IMAGE DENOISING USING SPARSE AND OVERCOMPLETE REPRESENTATIONS

A

Thesis Submitted

in Partial Fulfilment of the Requirements

for the Degree of

DOCTOR OF PHILOSOPHY

By

BHABESH DEKA

to the

DEPARTMENT OF ELECTRONICS AND ELECTRICAL ENGINEERING

INDIAN INSTITUTE OF TECHNOLOGY GUWAHATI

GUWAHATI - 781039, INDIA

FEBRUARY, 2011

IMAGE DENOISING USING SPARSE AND OVERCOMPLETE REPRESENTATIONS

Bhabesh Deka

Certificate

This is to certify that the thesis entitled "**IMAGE DENOISING USING SPARSE AND OVERCOMPLETE REPRESENTATIONS**", submitted by **Bhabesh Deka** (03610205), a research scholar in the *Department of Electronics and Electrical Engineering, Indian Institute of Technology Guwahati*, for the award of the degree of **Doctor of Philosophy**, is a record of an original research work carried out by him under my supervision and guidance. The thesis has fulfilled all requirements as per the regulations of the institute and in my opinion has reached the standard needed for submission. The results embodied in this thesis have not been submitted to any other University or Institute for the award of any degree or diploma.

Dated:
Guwahati.

Prof. Prabin Kumar Bora
Deptt. of Electronics and Electrical Engg.
Indian Institute of Technology Guwahati
Guwahati - 781039, India.

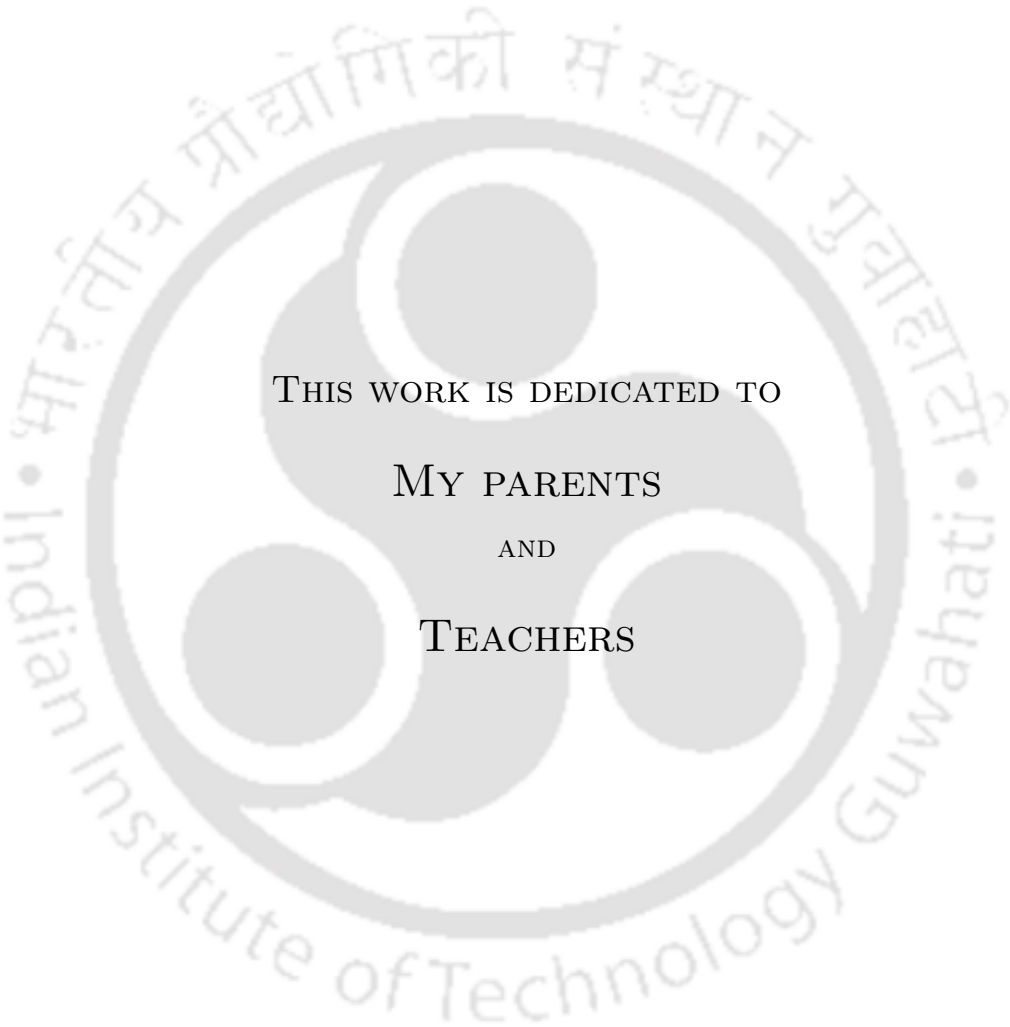

This work is dedicated to

My parents

and

Teachers

Acknowledgements

I owe my deepest sense of gratitude to my supervisor Prof. Prabin K. Bora for his excellent guidance. This thesis would not have been possible without his help, support and patience. I am very thankful for his stimulating suggestions and constant encouragement in all the time of this research and writing of this thesis.

I am also very thankful to other members of my doctoral committee, Prof. Samarendra Dandapat, Prof. Anil Mahanta and Prof. Ratnajit Bhattacharjee for sparing their precious time to evaluate the progress of my work. Their suggestions and assistance have been valuable.

I acknowledge my sincere gratitude to Dr. Debashis Ghosh and Dr. J. S. Sahambi who introduced me to research in the field of biomedical signal processing. I would also like to thank other faculty members of the Department for their support and constant encouragement during this course of study. Sincere thanks are also due to Prof. P. P. Sahu, Department of ECE, Tezpur University for his constant support in completing this research.

I am grateful to all the members of the research and technical staff of the Department. My special thanks to Mr. Sanjib Das, Mr. L. N. Sarma for maintaining an excellent computing facility and providing various resources useful for the research work.

Thanks go out to all my friends at the Image and Signal Processing Laboratory. Specially, I would like to thank to P. Vinod, Himanshu, Dakua, Kuntal, Rupaban Subedar, Ramesh Mishra, Mukesh Singh, Shyam, Padam Priyal, and Mridupawan for their help and support in many ways.

My deepest gratitude goes to my family for their continuous love and support throughout my studies. The opportunities that they have given me and their unlimited sacrifices are the reasons for where I am and what I have accomplished so far. I would also like to express special thanks to my wife for her sacrifice and incessant motivation towards the completion of this research work.

Finally, my tenure at IIT Guwahati will be the guiding spirit for the rest of my academic career.

Bhabesh Deka

Abstract

An image is corrupted by noise during its acquisition, transmission or storage. Noise degrades the image quality and interpretability. The aim of image denoising is to remove the distortion resulted by the noise while keeping the detail features in the image intact. The *sparse denoising* methods represent a class of denoising algorithms based on the principle that a natural signal like the image is *sparse* over some basis set but the noise is not. This has led to the widespread application of these methods in image denoising. Recent works in the literature focus on the use of *sparse and overcomplete representations* to develop state-of-the-art image denoising techniques. The thesis addresses the problem of image denoising by the sparse and overcomplete representations.

One of the recent additions to the greedy solution to the sparse representation problem is the *Bayesian Pursuit Algorithm* (BPA). The thesis critically examines the algorithm and proposes a modification by integrating a new initialization scheme and a stopping criterion to enhance its performance. The modified BPA converges to the true solution much faster than the standard BPA. It is also applied for the removal of additive white Gaussian noise from gray-scale images. Experimental results demonstrate that the modified BPA successfully removes the noise at low noise levels.

The thesis proposes two sparse denoising techniques based on the overcomplete dictionary for the removal of the *impulse noise* and the *speckle noise*. The novel *sparse reconstruction filter* is proposed for the removal of the impulse noise based on the principle of *signal recovery by compressed sensing*. The impulse-free pixels in the image are identified by an impulse detection algorithm and are used to reconstruct the noisy pixels using the *orthogonal matching pursuit* (OMP) algorithm with an overcomplete dictionary. The filter performs better than selected state-of-the-art impulse denoising filters.

The thesis explores removal of the speckle noise from medical ultrasound images using the sparse representation on an overcomplete dictionary. Many of the denoising algorithms including the ones based on the sparse representation of the signal require the noise to be additive, white and Gaussian. However, this assumption fails for speckle in the medical ultrasound images in the log-transform domain. The thesis adopts an existing technique for the decorrelation and the Gaussianization of the speckle in the log-transform domain and the resulting image is denoised by using sparse and overcomplete representations. Two denoising methods are applied on the preprocessed ultrasound images in the log-transform domain. They are: (1) the *undecimated wavelet transform* (UDWT) based soft thresholding and (2) the OMP-based sparse representation. Both the methods show improvements over the existing techniques for despeckling of medical ultrasound images.

Contents

List of Figures

List of Tables

List of Acronyms

ACWM	Adaptive center weighted median
AWGN	Additive white Gaussian noise
AWMF	Adaptive weighted median filter
BCS	Bayesian compressive sensing approach
BG	Bernoulli-Gaussian
BP	Basis pursuit
BPA	Bayesian pursuit algorithm
BPDN	Basis pursuit denoising
BSS	Blind source separation
CEF	Contrast enhancement filter
CLT	Central limit theorem
CS	Compressed sensing
CWT	Continuous wavelet transform
CWM	Center weighted median
DCT	Discrete cosine transform
DWM	Directional weighted median
DWT	Discrete wavelet transform
DWT-STH	DWT based soft thresholding
FOCUSS	Focal under-determined system solver
FTD	Fisher-Tippett distribution
GGD	Generalized Gaussian distribution
GGAD	Generalized gamma distribution
GND	Generalized Nakagami distribution
GP	Gradient pursuit
HWDS	Homomorphic wavelet based despeckling methods

HWF	Homomorphic Wiener filter
K-SVD	K singular value decompositions
LF	Lee filter
LLS	Linear least squares
MACWM	Modified adaptive weighted median
MAP	Maximum *a posteriori*
MLE	Maximum likelihood estimation
MM	Method of moments
MP	Matching pursuit
MSE	Mean square-error
NIG	Normal inverse Gaussian
NLM	Nonlocal Means
NP	Non-deterministic polynomial-time
OCT	Optical coherence tomography
OMP	Orthogonal matching pursuit
PCA	Principal component analysis
pdf	Probability density function
PSD	Power spectral density
PSF	Point spread function
PSM	Progressive switching median filter
PSNR	Peak signal-to-noise ratio
RCM	Rank conditioned median
RMSE	Root mean square error
SAR	Synthetic aperture radar
SBL	Sparse Bayesian learning
SBPA	Standard Bayesian pursuit algorithm
SD-ROM	Signal-dependent rank ordered mean
S/MSE	Signal-to-MSE
SNR	Signal-to-noise ratio
SONAR	Sound navigation and ranging
SRAD	Speckle reducing anisotropic diffusion
SRF	Sparse reconstruction filter

SSIM	Structural similarity index
SSNR	Speckle signal-to-noise ratio
StGP	Stage-wise weak gradient pursuit
StOMP	Stage-wise orthogonal matching pursuit
SURE	Stein's unbiased risk estimator
SVD	Singular value decomposition
UDWT	Undecimated wavelet transform
UDWT-STH	UDWT based soft thresholding
WM	Weighted median

List of Symbols

$\boldsymbol{\alpha}$	Sparse coefficient vector
$\mathbf{A}$	Sparse coefficient matrix
a	GGAD scale parameter
β	Edge preservation index
C	Noise gain
c	GGAD shape parameter
$\mathbf{c}$	Correlation vector
$\mathbf{D}$	Dictionary for CS recovery
$d(s,t)$	Impulse noise value at the location (s,t)
δ	Ultrasound resolution index
ε	RMSE of sparse representation
f	Probability density function
$\|.\|_F$	Frobenius norm
γ	Penalty parameter
$h(.)$	Point spread function
$\mathbf{I}$	Identity matrix
$\mathcal{I}$	Index set
K	Number of atoms in an overcomplete dictionary
κ	Coefficient of correlation
$K \times 1$	Dimension of a sparse coefficient vector
$\mathbf{L}_i$	Binary matrix that extracts the i^{th} patch from an image
$\|.\|_0$	ℓ^0 quasi-norm of a signal; Number of nonzero elements in a vector
$\|.\|_1$	ℓ^1-norm
$\|.\|_2$	ℓ^2-norm
λ	Sparsity inducing regularization parameter

M	Total number of training signals
μ	Mutual coherence
$\sqrt{m} \times \sqrt{m}$	Dimension of an image
$\sqrt{m}_p \times \sqrt{m}_p$	Dimension of an image patch
$m \times K$	Dimension of an overcomplete dictionary
$\mathbf{n}$	Noise in an image
N	Number of nonadaptive measurements in compressed sensing
$N \times K$	Dimension of $\mathbf{D}$ for sparse recovery
$N \times m$	Dimension of the sensing matrix
ν	Scaling parameter close to unity
$\mathbf{P}$	Square grid on an image
$P(\omega_1, \omega_2)$	PSD
p	Probability of inactive atoms
$\mathbf{\Phi}$	Overcomplete learned dictionary
$\mathbf{\Psi}$	Sensing matrix
$R_{xx}(.)$	Autocorrelation function
$\mathbb{R}^n$	Real vector space of dimension n
$\mathbb{R}^{n \times m}$	Real vector space of dimension $n \times m$
$\mathbf{r}_\mathrm{s}$	Residual error
$\mathbf{r}$	Amplitudes of sparse coefficient vector
r	Impulse noise ratio
ρ	Ultrasound decorrelation parameter
σ_n	Standard deviation of noise
σ_r	Standard deviation of the nonzero sparse coefficients
$\mathbf{s}$	Measured data
s	Iteration of a pursuit algorithm
(s, t)	Spatial location in an image
T	Transpose
t	Threshold parameter
v	GGAD shape parameter
$\mathbf{W}$	Square window for neighbourhood operation
$w(i, j)$	Weight representing similarity between the neighborhoods of each pair of pixels (i, j)

$\mathbf{x}$	Original image
$\hat{\mathbf{x}}$	Reconstructed image
x_{MAX}	Maximum gray level value in an image
$\mathbf{Y}$	Dataset to train a dictionary
$\mathbf{y}$	Noisy observed image
$\mathbf{z}$	Impulse detected image
ζ	Sparsity measure

Chapter 1

Introduction

An image is corrupted by noise at stages of acquisition, processing, transmission and storage. For example, when an analog image is converted to a digital image, the resulting digitized image contains noise due to quantization. Noise reduces the image quality and is especially significant when the objects being imaged are small and have relatively low contrast. It is necessary to apply an efficient denoising technique to compensate for such noisy data. The aim of image denoising is to remove the distortion resulted by the noise while keeping, as much as possible, the important features of the image intact. The performance of any image denoising algorithm relies on the understanding and exploiting the differences between the noise and the signal.

Noise modeling is greatly influenced by the capturing instruments, data transmission media, and image quantization. Most of the natural images get corrupted by additive white Gaussian noise. Other types of noise which are not modelled by a Gaussian distribution are the *impulse noise* and the *speckle noise*.

1.1 Noise Model

Let $y(s,t)$ denote an observed image. Considering an additive noise model, we can write

$$y(s,t) = x(s,t) + n(s,t) \tag{1.1}$$

where $x(s,t)$ is the desired noise-free image and $n(s,t)$ is the *additive noise* component and (s,t) represent a spatial location in the image. The Gaussian noise is generally considered to be an additive component. The additive model in Equation (1.1) also assumes that n is independent of x. The thermal noise, photographic film noise, and quantization noise obey the additive noise model.

The second most common noise model is the *multiplicative model*

$$y(s,t) = x(s,t)n(s,t) \tag{1.2}$$

The multiplicative model is most appropriate when the noise is not independent of x. One common application of this model is the speckle noise in coherent imagery such as the ultrasound image.

There are also some applications where neither the additive nor the multiplicative noise fits the noise well. The Poisson counting noise and the impulse noise fit neither model well.

1.2 Types of Noise

1.2.1 Gaussian Noise

The Gaussian distribution is widely used to model the thermal noise and it is the limiting distribution of other noises such as the photon counting noise and the film grain noise [1]. The density function of the Gaussian noise n with mean μ_n and variance σ_n^2 is

$$f_n(x) = \frac{1}{\sqrt{2\pi\sigma_n^2}} e^{\frac{-(x-\mu_n)^2}{2\sigma_n^2}}; \quad -\infty < x < \infty \tag{1.3}$$

The Gaussian distribution has many convenient mathematical properties. For example, the linear operations on Gaussian random variables yield Gaussian random variables. The *Central Limit Theorem* (CLT) states that the distribution of the sum of a large number of independent, small random variables tends to Gaussian distribution, thus giving a justification for the wide use of the Gaussian noise model.

1.2.2 Heavy-Tailed Noise

A heavy tail means that there is a larger probability of getting very large values. The heavy-tailed noise is not Gaussian because its density approaches 0 more slowly than the Gaussian. For example, a noise n with the double exponential density

$$f_n(x) = \frac{1}{2\sigma_n^2} e^{-\frac{|x|}{\sigma_n^2}}, \quad -\infty < x < \infty, \tag{1.4}$$

is a heavy-tailed noise. The impulse noise and the speckle noise are examples of heavy-tailed noise.

Impulse Noise

The impulse noise is a short-duration noise of fixed or variable amplitudes. It may be caused by a variety of sources, such as the saturation of the sensors or the adverse channel environment in a communication system. The data that are affected by the impulse noise change drastically and are perceptible compared to other data in the neighbourhood.

Impulses may have fixed values or their amplitudes may be all different. The first type of impulse noise appears as black and/or white spots in gray-scale images, because the noisy pixels have either very large or very small values. It mainly arises owing to the saturation of the imaging sensors. Extreme values are digitized as minimum and maximum allowed values. Such a fixed-valued impulse is called the *salt-and-pepper noise*. The second type of impulse noise that has varying amplitudes is more realistic and known as *random-valued impulse noise*. The typical source of such noise is the transmission channel that is usually affected by lightning or other atmospheric disturbance. The following noise models have been proposed in the literature to model the impulse noise [2].

1. *One-sided Impulse Noise Model*

This model assumes that impulse noise corrupting a signal sample is independent of the original signal value and the noise at other samples [2]. A sample corrupted by the impulse noise has the fixed value $d(s,t)$ at the location (s,t) while other samples remain unaltered. Let $x(s,t)$ denote the original image sample and $y(s,t)$ denote the noisy sample value. The model is expressed as follows:

$$y(s,t) = \begin{cases} d(s,t), & \text{with probability } r \\ x(s,t), & \text{with probability } 1-r. \end{cases} \tag{1.5}$$

2. *Two-sided Impulse Noise Model*

At every signal point an impulse occurs with probability r independent of both the noise at other signal points and the values of the original signal [2]. In this model, a corrupted point can have one of two extreme values, that is, either l (negative impulse) or h (positive impulse), where l is 0 and h is $2^b - 1$, and b is the number of bits per pixel. The model can be expressed in the following way:

$$y(s,t) = \begin{cases} l, & \text{with probability } r/2 \\ h, & \text{with probability } r/2 \\ x(s,t), & \text{with probability } 1-r. \end{cases} \tag{1.6}$$

3. *Bit Errors Impulse Noise Model*

A realistic impulse noise normally does not take a fixed value [2]. Its amplitude ranges from the

minimum to maximum allowable range in realistic case (between 0 and $2^b - 1$, where b is the number of bits per pixel). It may occur due to the change of bit values in the signal. Consider the image sample $x(s,t)$ at location (s,t).

$$x(s,t) = k_1 2^{b-1} + k_2 2^{b-2} + ... + k_{b-1}2 + k_b, \tag{1.7}$$

where $k_j \in \{0,1\}$ for $j = 1, 2, \ldots, b$. Assume that the bit errors occur with probability r independent both of the errors at other samples and the error in this sample. Then the corrupted signal values are of the form:

$$y(s,t) = k_1^* 2^{b-1} + k_2^* 2^{b-2} + ... + k_{b-1}^* 2 + k_b^*, \tag{1.8}$$

where

$$k_j^* = \begin{cases} k_j, & \text{with probability } 1-r \\ 1-k_j, & \text{with probability } r. \end{cases} \tag{1.9}$$

The following model is used for such random-valued impulse noise

$$y(s,t) = \begin{cases} x(s,t), & \text{with probability } 1-r \\ d(s,t), & \text{with probability } r. \end{cases} \tag{1.10}$$

Speckle Noise

Speckle is one of the more complex image noise models. It is signal dependent, non-Gaussian, and correlated. It is present in all coherent imaging systems (ultrasound, radar imaging, etc.). The details regarding the formation of speckle can be found in [1, 3]. In the following we discuss the speckle formation in ultrasound imaging, but the same principles apply to other coherent imaging systems as well.

When an acoustic pulse travels through tissues or any medium, backscattering from the scatterers within the resolution cell of the transducer contributes to the returned echo. Because of the random locations of the scatterers, the received echo is subjected to random variations in the phase and the amplitude. Some of these variations are in phase and add constructively, resulting in strong intensity, and others are out of phase and add destructively, resulting in low intensities. This gives rise to an interference pattern of bright and dark spots known as speckle.

Two important assumptions are made for the formation of speckle: 1) the scatterers are much smaller in size than the ultrasound wavelength. This means that each microscopic reflector in a homogeneous tissue cannot be resolved by the imaging system and is having random amplitude and

phase. 2) the variations at different points are independent from each other and independent from changes at any other point.

Speckle Noise Model

The amplitude of the reflected signal at any point (s,t) is the result of multiplication of the incident signal by a phasor with a random amplitude $a(s,t)$ and a random phase $\theta(s,t)$. Let $u(s,t)$ be the complex phasor of the incident wave at any point (s,t), $x(s,t)$ be the reflected signal, and $w(s,t)$ be the received phasor. Therefore, from the above assumption we can write

$$x(s,t) = u(s,t)a(s,t)e^{j\theta(s,t)}. \tag{1.11}$$

Let $h(s,t)$ be the *point-spread function* (PSF) of the ultrasound imaging system. $h(s,t)$ is assumed to be linear and space invariant [4] so that

$$w(s,t) = h(s,t) * x(s,t), \tag{1.12}$$

where $*$ is the convolution operation. Writing the phasors $x(s,t)$ and $w(s,t)$ in terms of rectangular coordinates

$$x(s,t) = x_R(s,t) + jx_I(s,t) \tag{1.13}$$

$$w(s,t) = w_R(s,t) + jw_I(s,t), \tag{1.14}$$

we can write from Equation (1.12)

$$w_R(s,t) = \int_{-\infty}^{\infty}\int_{-\infty}^{\infty} h(\alpha,\beta)x_R(s-\alpha,t-\beta)d\alpha d\beta, \tag{1.15}$$

and similarly

$$w_I(s,t) = \int_{-\infty}^{\infty}\int_{-\infty}^{\infty} h(\alpha,\beta)x_I(s-\alpha,t-\beta)d\alpha d\beta. \tag{1.16}$$

Considering Equations (1.15) and (1.16) as sums over infinitesimal increments of the values of s and t which are independent of each other, we can conclude that $w_R(s,t)$ and $w_I(s,t)$ are Gaussian with mean 0 and variance σ^2 by virtue of the CLT. These assumptions are valid as long as the size of the scatterers are small on the scale of a wavelength of the ultrasound and the imaging system cannot resolve the individual scatterers. Thus the real and imaginary components of the reflected waves are individually filtered by the PSF of the imaging system.

When the number of scatterers within one resolution cell is large and the phases of scattered waves are uniformly distributed between 0 and 2π, the received phasor with real and imaginary

components has a joint probability density function (pdf) given by [3, 5]

$$f_{w_R,w_I}(x,y) = \frac{1}{2\pi\sigma^2} e^{\left\{-\frac{x^2+y^2}{2\sigma^2}\right\}} \tag{1.17}$$

The pdf of the phasor magnitude $y(s,t) = \left(w_R(s,t)^2 + w_I(s,t)^2\right)^{1/2}$ is given by

$$f_y(r) = \begin{cases} \dfrac{r}{\sigma^2} e^{\left\{-\frac{r^2}{2\sigma^2}\right\}}, & r \geqslant 0 \\ 0, \text{ otherwise} \end{cases}, \tag{1.18}$$

which is the Rayleigh distribution. The pdf for the intensity $I = y^2$ is given by [3]

$$f_I(r) = \begin{cases} \dfrac{1}{2\sigma^2} e^{\left\{-\frac{r}{2\sigma^2}\right\}}, & r \geqslant 0 \\ 0, \text{ otherwise.} \end{cases} \tag{1.19}$$

In ultrasound imaging, y is the quantity of interest since the ultrasound B-scan detection senses the envelope of the echo of the transmitted ultrasound pulses. Therefore, the envelope of the echo over a homogeneous region can be modelled by the Rayleigh distribution.

The PSF of the ultrasound imaging system highly influences the properties of speckle. When the PSF support is larger compared to the numerous independent structures in a biological tissue but smaller compared to the features of interest in the image, then the noise is exponentially distributed and uncorrelated [1, 6]. In contrast to this, if the PSF support is larger compared to both the size of scatterers and the features of interest in the image, then the speckle is correlated and its distribution is dependent on the PSF, the frequency of ultrasound and the distance between the transducer and the objects being imaged [6].

1.3 Research Background on Image Denoising

An important and widely studied problem in image processing is the development of image denoising algorithms that remove noise artifacts while retaining the image structure. It is also important for postprocessing methods like segmentation, classification, object recognition, pattern analysis, registration, etc. In many applications like video analysis, image guided surgical interventions, etc. real-time denoising is also required.

The classical image denoising techniques are based on filtering, which can be classified into two categories of linear filtering and nonlinear filtering. *All these linear filtering methods assume that the noise is additive and Gaussian.* The most basic linear filter is the mean filter that replaces a pixel with the average value in a window. It is a low-pass filter with following limitations: 1) it tends to

blur sharp edges, destroy lines and other fine image details and 2) it performs poorly in the presence of non-Gaussian and signal-dependent noise. Linear filtering can be applied either in the spatial domain or in the frequency domain. The Wiener filter [7] is implemented in the frequency domain and is an optimal linear filter in terms of the mean square error if both the noise-free image and the noise are jointly Gaussian. The limitation of the Wiener filter is its low-pass characteristics, which gives rise to unacceptable blurring of lines and edges. This is due to the space invariant nature of the filter.

As stated above, the basic difficulty with the classical image filtering methods is that, they tend to blur the image, which is usually not expected from any good and stable filtering techniques. In particular, the sharp edges or lines that occur in the image should be preserved while filtering. With the discovery of *continuous wavelet transform* (CWT) by Grossmann and Morlet [8] and the application of *discrete wavelet transform* (DWT) in signal processing by Mallat [9], a new tool for the study of non-stationary signals was developed. In particular, in the early 1990s, Donoho *et al.* [10,11] demonstrated a simple denoising procedure by thresholding the detail wavelet coefficients. He showed that it had desirable statistical optimality properties. This method exploits the *sparsity* property of the discrete wavelet transform and uses the fact that this transform maps the white noise in the signal domain to the white noise in the transform domain. This is the unique property which enables the separation of the signal from the noise. The *wavelet shrinkage* is an image denoising technique based on the idea of thresholding the wavelet coefficients. Although the wavelet transform on an image is a linear operation, wavelet shrinkage is a nonlinear filtering method because of the presence of nonlinear thresholding operation. It may be adaptive or non-adaptive. *Visushrink* [12] is a non-adaptive thresholding method that depends only on the number of data points. The adaptive *SUREshrink* [10] technique uses a combination of the universal threshold and the SURE (Stein's Unbiased Risk Estimator) technique and performs better than the Visushrink. The *BayesShrink* [13] minimizes the Bayes' Risk Estimator function considering a generalized Gaussian prior for the signal and thus estimates a data-adaptive threshold.

The main limitation of the DWT is that it is not translation invariant because of the decimation operation. That is, the translation of the original signal leads to different wavelet coefficients. It gives rise to the pseudo-Gibbs phenomenon or the ringing effect [14, 15] in the denoised output. In order to overcome this and get more complete characteristic of the analyzed signal, the shift-invariant *undecimated wavelet transform* (UDWT) was proposed [14]. This transform produces more precise information for the frequency localization and the denoised images possess better perceptual qualities.

But the UDWT has larger storage space requirements and involves more computations.

In [16, 17], the authors showed that the traditional wavelet is not effective for describing a two dimensional image because the discontinuities present in it are spatially distributed and the wavelet coefficients for them are not *sparse*. Wavelets do very well for the representation of point singularities present in an one dimensional signal but fails in the case of lines and curves in images. To overcome these limitations, several new multiscale transforms were proposed. These include the *curvelets* [16], the *contourlets* [18], and the *ridgelets* [17]. Image denoising using these transforms are reported in [19–21].

Another promising class of nonlinear filtering methods for removing white Gaussian noise is the class of *nonlocal means algorithms*. An outline of the NLM algorithm is given below:

1.3.1 Nonlocal Means Algorithm

The nonlocal means (NLM) algorithm introduced by Buades *et al.* [48] is recently gaining an increasing popularity due to its excellent performance. It is a nonlinear filter based on the weighted average of pixels inside a search window which is relatively large compared to the traditional neighborhood techniques. Each pixel is weighted according to its similarity with its own neighborhood, and the neighborhoods of every other pixels in the image.

Let $x(i)$ be the original image, and $y(i)$ be the observed image indexed by an index variable $i \in \mathcal{I}$, where $\mathcal{I}$ is the index set. The restored value $\hat{x}_{NL}$ at location i is given as the Gaussian weighted average of all the pixels in $\mathcal{I}$. Thus,

$$\hat{x}_{NL}(i) = \sum_{j \in \mathcal{I}} w(i,j) y(j) \tag{1.20}$$

where $w(i,j)$ is the Gaussian weight. The weight $w(i,j)$ expresses the similarity between the Gaussian neighborhoods of pixels (i and j). It is given by,

$$w(i,j) = \frac{1}{Z(i)} e^{-\frac{\left\| y(\mathbf{N}_i) - y(\mathbf{N}_j) \right\|_{2,q}^2}{h^2}} \tag{1.21}$$

where $Z(i)$ is the normalizing factor $Z(i) = \sum_j e^{-\frac{\left\| y(\mathbf{N}_i) - y(\mathbf{N}_j) \right\|_{2,q}^2}{h^2}}$, and h is the decay parameter of the weights. In the above equation, $y(\mathbf{N}_i)$ is the vector of neighborhood pixel values, and $y(\mathbf{N}_i) := (y(j), j \in \mathbf{N}_i)$, where $\mathbf{N}_i$ defines the neighborhood of pixel i. The vector norm used in Equation (1.21) is simply the Euclidean difference, weighted by a Gaussian of zero mean and variance q [49].

The NLM algorithm works on the white Gaussian noise assumptions, and does not work for non-white and non-Gaussian noise. Another limitation of the NLM algorithm is the high computational

cost. For example, for an image with m pixels, m weights have to be computed for each pixel. Computation of the m^2 overall weights makes the algorithm inefficient and impractical. Many improvements of the original NLM algorithm was carried out later on, including the multiscale versions in [49], and the accelerated NLM by eliminating unrelated neighborhoods in [50].

1.3.2 Filtering of Heavy-tailed Noise

The filtering methods that we have discussed so far, are not adequate when the noise is not additive and/or modelled by non-Gaussian or heavy-tailed distributions. The impulse noise and the speckle are typical examples where linear filtering fails.

A robust nonlinear technique for recovering the signal when the noise-distribution is heavy-tailed or when the data are contaminated by outliers is the *median filter* [22]. The median filter is a nonlinear filter that takes the median of the data inside a moving window of pre-determined length as the filtered output. It works well for heavy-tailed noise distributions, whereas its performance is poor for short-tailed noise distributions [23]. Therefore, the median filter is effective at removing the impulse noise. The disadvantage of the median filter is that all the pixels are treated equally regardless of their locations within the window and as a result blurring of edges in the image occurs. One way to improve the performance of the median filter is to use the *weighted median* (WM) [24] which gives more weight to some samples within the window than the others. Because of the symmetric nature of the window, the sample that is most correlated with the desired estimate is, in general, the observation sample at the centre [1]. This leads to the *center weighted median* (CWM) filter [25] which is a special case of the WM filter. The CWM filter is highly effective in removing the salt-and-pepper noise while preserving the fine image details. The main limitation of the median filter and its variants is that they try to modify the pixels which are not affected by noise.

A better way to overcome this limitation is to incorporate some decision-making processes in the filter. At each pixel location, it is first determined whether the pixel is corrupted by noise. Filtering is applied on the pixel only if it is detected as noisy. The corrupted pixels are replaced by the median values or other suitable estimates, while keeping the noise-free pixels unaltered. Filters in this category include the *rank-conditioned median* (RCM) filter [26], the *signal-dependent rank-ordered mean* (SD-ROM) filter [27], and the *adaptive center weighted median* (ACWM) filter [28], etc.

The speckle noise in medical ultrasound images is a signal-dependent and multiplicative noise as discussed earlier and it depends on the structure of imaged tissue and various imaging parameters.

A spatially adaptive filter for smoothing speckle in ultrasound image was proposed in [29]. A spatial filter based on local statistics of the log-transformed ultrasound images using unsharp masking can be found in [30]. These filters fail to remove speckle near or on the edges. Filters based on the region growing technique have been proposed in [31, 32]. The disadvantage of these methods is due to the lack of a universal criterion to select a similarity property on which region growing can be carried out. Some other well known spatial filters are the *Lee filter* [33] and the *Kuan filter* [34]. These filters perform spatial averaging in the homogeneous regions and perform no filtering where edges and point features are present. This is achieved by introducing a coefficient of variation inside the moving window. In [35], an adaptive weighted median filter is used due to its robustness against impulsive type noise and edge preserving characteristics. Another nonlinear filter method using an edge sensitive diffusion called the speckle reducing anisotropic diffusion (SRAD) was proposed in [36] to suppress speckle in ultrasound image while preserving the edge information.

All the above filters are applied directly on the image having the multiplicative noise model. The *homomorphic* Wiener filter proposed in [7] first converts the multiplicative noise into an additive noise through the logarithmic transformation on the speckled image. Then the Wiener filter is used to reject the resultant additive noise followed by the exponential transformation on the filtered image.

Many multiscale methods based on the wavelet transform have also been proposed to *despeckle* ultrasound images. These methods in general consist of five key operations: (1) logarithmic transformation (2) wavelet transformation (3) modification of wavelet coefficients using some thresholding (shrinkage) function (4) inverse wavelet transform and finally (5) exponential transformation. In the image denoising literature these methods are collectively referred to as the *homomorphic wavelet based despeckling methods* (HWDS). The wavelet thresholding methods for the reduction of speckle can be found in [37, 38]. These methods adopted a soft thresholding procedure which was originally proposed by Donoho [10,11] to remove noise within the finer scales and in the non-linear processing of feature energy for contrast enhancement. However, thresholding methods have two main limitations: (1) the choice of the threshold, the most important design parameter, is done in an ad hoc manner; and (2) the specific distributions of the signal and noise are not at all considered.

To address the above issues, Simoncelli and Adelson [39] developed non-linear estimators in the wavelet domain, based on the formal Bayesian theory. They used a generalized Gaussian model for the subband statistics of the signal at different scales and thereby estimated the signal using a maximum *a posteriori* (MAP) estimator. Achim *et al.* [40] developed a MAP estimator for the removal of speckle by modeling the signal wavelet coefficients by the alpha-stable distribution [41]

and the noise wavelet coefficients by the Gaussian distribution for the wavelet decomposition at different scales. In [42], the authors proposed a versatile despeckling method by modeling the noise wavelet coefficients by the generalized Nakagami distribution. Thus, the success of the Bayesian methods depends on the proper use of the statistical distributions to model the signal and the noise.

The main limitation of the HWDS methods is that it assumes that the speckle noise in the log-transformed image is white and Gaussian. However, they are correlated [43] and also cannot be modelled well by the Gaussian distribution after the logarithmic transformation. A modified HWDS is proposed in [44] to overcome these limitations.

There is yet another class of algorithms for the reduction of speckle which do not apply the logarithm prior to the application of the wavelet transform. These *non-homomorphic methods* filter the wavelet coefficients of the original speckle corrupted image without log-transformation. Pižurica *et al.* [45] proposed a versatile denoising method in this category using the UDWT for medical ultrasound images. It considers the correlation of useful wavelet coefficients across scales. This method does not rely on the exact prior knowledge of the noise distribution and is more flexible and robust compared to other wavelet based methods. In [46,47], the authors proposed non-homomorphic approaches for filtering synthetic aperture radar (SAR) images.

A recent development in denoising is through the sparse representation of signals as continued below.

1.4 Image Denoising via Sparse and Overcomplete Representations

1.4.1 Sparse Representation

Natural images are highly redundant. They exhibit large correlations among neighbouring pixels because of the similar optical properties of the neighbouring points of the object and the PSF of the imaging device. Therefore, efficient coding techniques are required to remove these redundancies. A commonly adopted model in the image processing community is the transform coding in which an image is described by a linear combination of suitable basis functions. This is the principle of the coding strategy adopted in orthogonal transforms such as the *discrete cosine transform* (DCT) , the DWT of the image and the *principal component analysis* (PCA) of the image, etc. The PCA on a wide sense stationary signal results in an orthogonal transform (Karhunen-Loève transform) with transform coefficients completely decorrelated. All these transforms lead to the sparsification of the image to a certain degree. The assumption here is that the images have structures which can

be described well by second order correlations only. The DWT and its shift-invariant version, the UDWT, are very successful for the sparse representation of one-dimensional signals. The performance of the DWT and the UDWT in images deteriorates because the 2D separable bases cannot have compact representations for lines and edges.

The oriented lines and various edges in an image cause statistical dependencies that can be represented by higher-order correlations only [53]. The authors in [54] demonstrated that the localized structures such as step edge and the oriented structures like the lines and edges in the image cannot be described in terms of second order correlations alone. For such structures, the phases across different frequencies can be described only by higher-order correlations. The localized and compact distribution of energy in images leads to the *sparse structure* meaning that any given image can be represented with a few number of basis functions out of a much larger set [54].

In *sparse overcomplete representation*, a signal is expressed as a linear combination of a small number of elementary vectors called *atoms* chosen from an overcomplete basis set usually called the *overcomplete dictionary*. The number of atoms in the dictionary is much bigger than the dimension of the signal space. Decomposing a signal using an overcomplete dictionary gives rise to an ill-posed problem, because it does not have a unique representation.

Given an overcomplete system, the sparsest representation of a signal is the one that has the minimum ℓ^0-norm. In other words, the signal has the fewest number of nonzero coefficients with respect to the overcomplete basis set. Given the overcomplete dictionary $\mathbf{\Phi} \in \mathbb{R}^{m \times K}$, an ideal signal $\mathbf{x} \in \mathbb{R}^m$ can be represented as a linear combination of the atoms $\{\boldsymbol{\phi}_i\}_{i=1}^K$. The sparse solution is given by

$$\begin{aligned} \hat{\boldsymbol{\alpha}} &= \arg\min_{\boldsymbol{\alpha}} \|\boldsymbol{\alpha}\|_0 \\ \text{subject to } & \mathbf{x} = \mathbf{\Phi}\boldsymbol{\alpha}, \end{aligned} \tag{1.22}$$

where $\|.\|_0$ is the ℓ^0-norm counting the number of nonzero coefficients. Finding a solution to the above is an NP-hard [55, 56] problem and simpler formulations are made for tractable solutions.

Most algorithms for sparse representation can be classified into two categories, namely, the *greedy pursuit algorithms* and the algorithms based on the *ℓ^p-norm regularization*. The greedy pursuit algorithm obtains a sparse solution based on the correlation between the dictionary atoms and the observed data or the residual errors. The *matching pursuit* (MP) [57] and its modifications the *orthogonal matching pursuit* (OMP) [58] are the two pioneering greedy pursuit algorithms. In the ℓ^p-norm regularization based algorithms, a suitable ℓ^p-norm instead of the ℓ^0-norm is minimized

through regularization of a sparsity inducing norm. A representative of this category is the *basis pursuit* (BP) algorithm [55]. The BP solution to the sparse representation problem is given by

$$\begin{aligned} \hat{\boldsymbol{\alpha}} &= \arg\min_{\boldsymbol{\alpha}} \|\boldsymbol{\alpha}\|_1 \\ \text{subject to } & \mathbf{x} = \boldsymbol{\Phi}\boldsymbol{\alpha}, \end{aligned} \tag{1.23}$$

where $\|.\|_1$ is the ℓ^1-norm. The above problem is solved through the linear programming method and is known to give the ℓ^0-norm solution under certain conditions [59].

Though the BP gives a tractable solution to the sparse representation problem, linear programming involves high computational complexity. Therefore, locally optimal greedy algorithms are preferred.

1.4.2 Choice of the Overcomplete Dictionary

An important choice for the overcomplete dictionary is the basis set of an *overcomplete transform*. For such a transform the number of basis functions is more than the dimensionality of the input signal. An overcomplete transform is also translation invariant and possesses greater robustness against noise and other forms of image degradations. The overcomplete transforms like the UDWT, the curvelets, the contourlets, etc. have been found to be very effective [18,60–63] in various applications of image processing.

In some practical situations, the dictionary is built by taking a union of the basis sets of several transforms where each transform corresponds to an orthogonal basis or tight frame [64]. In [65], the authors use the combination of two dictionaries one for the representation of textures and the other for the natural scene parts assumed to be piecewise-smooth. When used with the BP [55] algorithm, it leads to the separation of different parts of the image. However, to represent the characteristics of an image completely, many transforms are required [66,67] and the size of the dictionary needed for sparse representation becomes very large.

An overcomplete dictionary of a reasonable size is needed for an efficient sparse representation and can be obtained by training on the image data. The trained overcomplete dictionary not only includes all kinds of characteristics in the image but also has a relatively smaller size. Aharon *et al.* [68] proposed a dictionary based on learning from the image patches as examples. The dictionary is updated in K steps considering one atom at a time. It is designed as a sequence of rank-one approximation problems solved by the *singular value decomposition* (SVD) method. They called this design of overcomplete dictionary as the *K-SVD*. The idea of learning a dictionary from the

image-patches can also be found in earlier works presented in [69–72].

The sparse representation of signals has recently seen many applications in signal processing such as time-frequency applications [55, 57], image denoising [55, 56], image deconvolution [73] and compressed sensing [74].

1.4.3 Sparse Denoising

The sparse representation of a signal through overcomplete transforms have been widely used in image denoising. In [61], the UDWT was used for denoising of 1D signals. Sendur and Selesnick [75] proposed a bivariate shrinkage estimator applied to the magnitude of the dual-tree complex wavelet transform coefficients for image denoising. Portilla *et al.* in [76] proposed an image denoising method based on a local Gaussian scale mixture model in an overcomplete wavelet transform. As pointed out earlier, to avoid the limitations posed by the wavelet transforms, new multiscale transforms using the curvelets, the ridgelets, the contourlets, etc. have been used for image denoising [19, 20].

The MP and BP algorithms have the ability to extract the signal from noisy data. The MP algorithm isolates the signal structures that are coherent with respect to a given dictionary. The signal energy is concentrated within a few atoms in the dictionary and MP can extract most of the signal energy in a few steps if the dictionary $\mathbf{\Phi}$ matches well with the signal $\mathbf{y}$. The additive white noise does not have any coherent structure with respect to any dictionary atom. An application of pattern extraction from noisy signals in a dictionary of Gabor functions has been shown [57]. The *basis pursuit denoising* (BPDN) [55] achieves the sparse representation for a signal corrupted with additive white noise through the regularization of the ℓ^1-norm. In [77], it is also shown that in the presence of the additive Gaussian noise, it is possible to recover the sparse representation of a signal with an error that grows at most proportional to the noise level. Applications of sparse representations in image denoising can be found in [56, 78, 79]

In [56], the authors have applied the K-SVD method for obtaining a learned dictionary which is then used for the sparse representation of the image corrupted by the additive white Gaussian noise. This technique is based on the principle of example-based image restoration. In this method, two training options are considered for obtaining the dictionary, namely, 1) training the dictionary using patches taken from the noisy image itself or 2) training on a corpus of patches taken from a set of high-quality images. The example based dictionary learning is limited by the handling of small image patches which may not ensure sparsity over the entire image. This limitation is avoided by adopting a global image prior which forces sparsity in every location of the patches in the image [80]. The

denoised image is then estimated by a MAP estimator along with a simple iterated patch-by-patch sparse coding and weighted averaging algorithm. The main steps of the K-SVD based denoising algorithm are:

- *Sparse Coding Step:* Perform sparse coding on image patches by using the OMP.
- *Dictionary Update:* Update the dictionary one atom at a time using the following steps:
  1. Compute the overall sparse representation error without considering the current atom.
  2. In order to ensure sparsity when computing the sparse coding vectors in the next step, restrict the error obtained above by considering only those training patches which use the current atom.
  3. Apply SVD on the restricted error as obtained above.
  4. Repeat Steps 1-3 for all the atoms.
- *Reconstruction:* Perform weighted averaging between the patches' approximations and the noisy image.

The authors in [79] extended the K-SVD based denoising method for the removal of white Gaussian noise from colour images. The modifications of the original K-SVD algorithm can be found in [79] to apply it for colour image inpainting and demosaicing with very good performance.

1.4.4 Compressed Sensing

Sparse representation has also led to the development of the theory of *compressed sensing* or *compressive sampling* (CS). It is a framework for signal acquisition and compression simultaneously and based on the work of Candès and Tao [81]. The CS principle allows the reconstruction of compressible signals from the sparse data sampled at a rate much lower than the Nyquist rate.

Consider a signal $\mathbf{x} \in \mathbb{R}^m$ that has a sparse representation $\mathbf{x} = \mathbf{\Phi}\boldsymbol{\alpha}$ with respect to a basis set $\mathbf{\Phi}^{m \times K}$ such that $\boldsymbol{\alpha}$ has at most k nonzero coefficients. Then $\mathbf{x}$ can be recovered by only $N \geqslant k.\log(m)$ projections on a second basis set $\mathbf{\Psi}$ incoherent with $\mathbf{\Phi}$ and obeying the *uniform uncertainty principle* (UUP). Mathematically, we can write $\mathbf{s} = \mathbf{\Psi}\mathbf{x}$, where $\mathbf{s}$ represents the measured data.

It basically solves the following optimization problem:

$$\begin{aligned} \hat{\boldsymbol{\alpha}} &= \arg\min_{\boldsymbol{\alpha}} \|\boldsymbol{\alpha}\|_p \\ \text{subject to } \mathbf{s} &= \mathbf{\Psi}\mathbf{\Phi}\boldsymbol{\alpha}, \end{aligned} \tag{1.24}$$

where $p = 0$ or 1 and $\mathbf{s}$ is the measured or available data. When $p = 0$, the solution involves the computationally exhaustive combinatorial optimization. The ℓ^1-norm optimization problem can be solved by the BP algorithm.

The authors in [82] have proposed a novel two stage algorithm for the removal of salt-and-pepper noise from gray scale images. In the first stage, the noisy pixels are detected using a simple impulse noise detection scheme. In the second stage, the image is reconstructed based on the partial noise-free pixels using the CS principles.

1.5 Motivation of the Present Work

The sparse representation of a signal over a redundant or an overcomplete dictionary is an important topic that has got many applications in signal processing. It has been successfully used for the removal of additive white Gaussian noise from images. However, only few works have investigated the use of sparse representation techniques for the removal of heavy-tailed noise, namely, the impulse noise and the speckle noise. The main objective of the thesis is to exploit sparse representations for removing such noises. The thesis explores the following issues:

1. Examine the sparse representation methods and suggest an improved technique for denoising applications.
2. Application of sparse representation techniques for the removal of impulse noise.
3. Adapt the sparse denoising methods for the removal of speckle noise.

1.6 Contributions of this Thesis

Main contributions of this thesis can be summarized into the following:

- Proposed a modified *Bayesian Pursuit Algorithm* (BPA) and applied it for the removal of additive white Gaussian noise from images.
- Proposed a unified detection based sparse reconstruction filter for the removal of impulse noise.
- Proposed an undecimated wavelet transform based method for the removal of speckle noise.
- Proposed a denoising method using a sparse representation on an overcomplete dictionary for the removal of speckle noise.

1.7 Thesis Organization

This thesis is divided into six chapters. The rest of the chapters are as outlined below.

Chapter 2: This chapter proposes a new initialization scheme and a stopping condition for the recently introduced Bayesian Pursuit Algorithm (BPA) for sparse representation in the noisy settings. This work also shows the application of the algorithm for the removal of additive white Gaussian noise from photographic images.

Chapter 3: This chapter presents a novel two-stage detection based sparse representation filter for the removal of fixed-valued and random-valued impulse noise. First, the noisy pixels are detected using an efficient impulse detection method. In the second stage, the noise candidates are reconstructed by using the sparse reconstruction based method in an iterative manner until convergence. The sparse reconstruction is based on the compressed sensing principle. Finally, the performance of the proposed technique is demonstrated on standard test images corrupted by impulse noise at different noise ratios.

Chapter 4: In this chapter first an existing undecimated wavelet transform based despeckling technique is modified by adopting an optimal parameter selection method. The rest of the chapter describes a method for despeckling of medical ultrasound images using the undecimated wavelet transform (UDWT). It is shown that the UDWT based despeckling algorithms can be used efficiently for the removal of multiplicative speckle noise by combining an existing preprocessing stage specifically designed for ultrasound images. The preprocessing stage reduces the autocorrelation of the speckle noise. Then using the standard homomorphic approach to despeckling, the log-transformed speckled images are subjected to a Gaussianization procedure to approximately model the speckle as white and Gaussian. The preprocessed speckled images are then denoised using the UDWT based soft-thresholding method. Results presented at the end of the chapter show that the proposed method suppresses the speckle noise very well while preserving the texture and other details present in the images.

Chapter 5: This chapter proposes a novel despeckling scheme for medical ultrasound images using the sparse and redundant representations over a learned overcomplete dictionary. It is observed that the image denoising methods via learned and overcomplete dictionary is optimal for the removal of additive white Gaussian noise only and cannot be applied for the removal of multiplicative speckle directly. We adopt the preprocessing stage applied in Chapter 4 before applying the sparse representation techniques for denoising. An adaptive dictionary is learned from the log-transformed speckled

images using the sparse representation principle to remove the speckle from the synthetic and medical ultrasound images. Extensive simulations are presented at the end of the chapter to show the effectiveness of the proposed filter for the removal of speckle noise both visually and quantitatively.

Chapter 6: A summary of the research work and the scope for future research are discussed in this chapter.

Chapter 2

Image Denoising Using the Modified Bayesian Pursuit Algorithm

2.1 Introduction

The sparse representation of a signal is based on the assumption that the natural signals can be expressed as a linear combination of a few bases from an overcomplete basis set. Such a representation results in a system of under-determined equations. Finding relevant sparse solutions of under-determined systems of linear equations in the presence of noise has been used popularly by the signal processing community. It has found applications in diverse areas. These include image denoising [56], image restoration [83], blind source separation (BSS) [84], compressed sensing (CS) [85], biometric authentication [86] and a host of other applications.

The sparse representation of an ideal noiseless signal $\mathbf{x}$ is modeled by

$$\mathbf{x} = \mathbf{\Phi}\boldsymbol{\alpha}, \tag{2.1}$$

where $\mathbf{x}$ is an $m \times 1$ signal vector, $\boldsymbol{\alpha}$ is a $K \times 1$ sparse coefficient vector, $\mathbf{\Phi}$ is an $m \times K$ matrix called the dictionary. It is assumed that $m \ll K$ which means that the dictionary is overcomplete. The columns of the dictionary are called the *atoms*. The above model assumes that $\mathbf{x}$ can be represented as a linear combination of atoms from the overcomplete dictionary $\mathbf{\Phi}$. Each atom is assumed to be of unity ℓ^2-norm throughout this work.

The representation of a signal with an overcomplete dictionary has the advantage over traditional orthogonal basis representations because they offer a wider range of generating elements (bases) and hence are more flexible in signal representation. A theoretical justification of the use of an overcomplete dictionary has been given in [69]. We assume here that the signal has a sparse representation on the overcomplete dictionary. Since the dictionary is overcomplete, the problem in Equation (2.1)

has infinitely many solutions.

Therefore, the solution of the above system of linear equations is posed as an optimization problem given by

$$\begin{aligned} &\min_{\boldsymbol{\alpha}} \|\boldsymbol{\alpha}\|_0 \\ &\text{subject to } \mathbf{x} = \boldsymbol{\Phi}\boldsymbol{\alpha}, \end{aligned} \tag{2.2}$$

where $\|.\|_0$ represents the ℓ^0-norm counting the number of nonzeros in a vector. Consider a signal $\mathbf{y}$ given by

$$\mathbf{y} = \mathbf{x} + \mathbf{n}, \tag{2.3}$$

where $\mathbf{n}$ is the additive white Gaussian noise (AWGN) with variance σ_n^2. The *noise-aware* variant of the sparse representation problem in Equation (2.2) can be modelled by

$$\begin{aligned} &\min_{\boldsymbol{\alpha}} \|\boldsymbol{\alpha}\|_0 \\ &\text{subject to } \|\mathbf{y} - \boldsymbol{\Phi}\boldsymbol{\alpha}\|_2 \leqslant \varepsilon, \end{aligned} \tag{2.4}$$

where ε is a constant depending on the mean-square-error of the representation and σ_n^2.

Finding the sparsest solution, over a redundant dictionary is an NP-hard combinatorial optimization problem [87]. This problem can be solved in a tractable way using two approaches: 1) optimization techniques and 2) greedy algorithms. The first category solves the problem by minimizing a cost function and the second one tries to find the nonzero elements directly through correlations between the dictionary atoms and the observed data or the residual. The optimization techniques are broadly divided into two categories, namely, the convex and non-convex optimization methods. The basis pursuit (BP) [55] as stated earlier , applies convex optimization that uses the ℓ^1-norm in place of ℓ^0-norm as the cost function. The resulting optimization problem is solved by the linear programming approach. The *Focal Under-determined System Solver* (FOCUSS) [88] is an important technique in the non-convex optimization category in the noise free case. Here it uses the ℓ^p-norm with $p < 1$ instead of the ℓ^0-norm [89]. The Bayesian methods such as the Sparse Bayesian Learning (SBL) [90], and Bayesian Compressive Sensing approach (BCS) [91] are also in the non-convex category.

The greedy category of sparse representation algorithms selects the atoms that best matches the signal structure at each iteration. It generally uses the correlation between the signal (or residual signal) and the atoms of the dictionary as a measure to find the atoms with nonzero coefficients. Mallat and Zhang [57] first introduced the concept of *Matching Pursuit* (MP) for the sparse representation

of signals over a redundant dictionary. There are a number of other pursuit algorithms like the *Orthogonal Matching Pursuit* (OMP) [58], *Stage-wise OMP* (StOMP) [92], *Gradient Pursuit* (GP) [93], *Stage-wise weak Gradient Pursuit* (StGP) [94], *Bayesian Pursuit Algorithm* (BPA) [95]. The greedy algorithms determine one active atom (eg., in MP) or several active atoms (eg., in StOMP) recursively at a time without solving a hard optimization problem in a multidimensional space. The MP determines it by exhaustively searching the atoms with highest correlations. In StOMP, it is done by comparing the correlations with a threshold [92]. The BPA algorithm which is a recent addition to the MP paradigm is based on a hypothesis testing as an activity measure to decide the nonzero components of the sparse vector in a Bayesian framework.

This chapter studies three of the MP algorithms, namely, the OMP, the StOMP, and the BPA. It proposes a modified BPA based on a new method of initialization and an improved stopping criterion. In the proposed algorithm, first a low-resolution sparse solution is obtained by hard thresholding. The BPA is initialized with this solution. To show the effectiveness of the proposed algorithm for denoising, we apply the modified BPA for the removal of additive white Gaussian noise in the sparse representation framework. In the following, we outline two of the popular greedy pursuit algorithms, namely, the Orthogonal Matching Pursuit (OMP), and the Stagewise OMP (StOMP) before discussing the Bayesian Pursuit Algorithm.

2.1.1 Orthogonal Matching Pursuit

The orthogonal matching pursuit (OMP) is a greedy step-wise regression algorithm [57, 58, 96]. At each iteration, the OMP selects an atom which has a maximum projection onto the residual. Then the sparse coefficients are obtained by orthogonal projection of the signal on the span of the selected atoms of current and previous iterations and the residual is recomputed. The process is repeated until convergence. Given a signal $\mathbf{y} \in \mathbb{R}^n$ and a dictionary $\mathbf{\Phi}$ with K ℓ^2-normalized atoms $\{\boldsymbol{\phi}\}_{k=1}^{K}$, the algorithm starts by setting $\mathbf{r}_0 = \mathbf{y}$, counter $\mathrm{s} = 1$, and perform the following steps:

1. Select the index of the next atom

$$\hat{i}_\mathrm{s} = \arg \max_{1 \leqslant i_\mathrm{s} \leqslant K} \left| \boldsymbol{\phi}_{i_\mathrm{s}}^T \mathbf{r}_\mathrm{s} \right| ;$$

2. Update the current approximation

$$\boldsymbol{\alpha}_\mathrm{s} = \min_{\boldsymbol{\alpha}_\mathrm{s}} \|\mathbf{y} - \mathbf{y}_\mathrm{s}\|_2 ,$$

such that $\mathbf{y}_\mathrm{s} \in \mathit{span}\left\{\boldsymbol{\phi}_{i_1}, \boldsymbol{\phi}_{i_2}, \ldots, \boldsymbol{\phi}_{i_\mathrm{s}}\right\}$; and

3. Update the residual $\mathbf{r}_s = \mathbf{y} - \mathbf{y}_s$.

The stopping rule of the algorithm can be based on either the solution reaching a fixed number of nonzero coefficients or the norm of the residual becoming less than a predefined threshold. The algorithm is widely used because of its computational simplicity.

Uniqueness of Sparse Solution

The OMP guarantees an optimal sparse solution if the signal $\mathbf{y}$ is sufficiently sparse. These algorithms produce a globally optimal solution under appropriate conditions on $\mathbf{\Phi}$ and $\mathbf{y}$. In order to develop an appropriate condition for such a solution, an important parameter is the *mutual coherence* μ of the dictionary $\mathbf{\Phi}$. It is defined by

$$\mu = \max_{1 \leqslant i,j \leqslant K, i \neq j} \left| \boldsymbol{\phi}_i^T \boldsymbol{\phi}_j \right|. \tag{2.5}$$

A dictionary is *incoherent* if μ is small. An optimal solution is guaranteed by the OMP if the sparsity ζ of $\mathbf{y}$ given by

$$\zeta = \|\boldsymbol{\alpha}\|_0,$$

satisfy the following condition [77]

$$\zeta < \frac{(1 + \mu^{-1})}{2}. \tag{2.6}$$

2.1.2 Stagewise Orthogonal Matching Pursuit

The stagewise orthogonal matching pursuit (StOMP) algorithm was proposed by Donoho *et al.* [92]. The algorithm converges in a fixed number of iterations (typically 10). The OMP is a special case of the StOMP. At each stage, the StOMP selects the atoms whose inner products with the current residual exceed a specific threshold. Since more than one atom is selected in each stage, the StOMP converges much faster than the OMP. The algorithm can be summarized as follows:

1. Initialize: solution $\boldsymbol{\alpha}_0 = \mathbf{0}$; residual $\mathbf{r}_0 = \mathbf{y}$; the support $\mathcal{I}_0$ of $\boldsymbol{\alpha}_0 = \emptyset$; counter s = 1.

2. Compute the correlations: $\mathbf{c}_s = \mathbf{\Phi}^T \mathbf{r}_{s-1}$

3. Apply hard thresholding to $\mathbf{c}_s$ to find the set of indices J_s such that

$$J_s = \{j : |c_s(j)| > t_s \sigma_n\} \tag{2.7}$$

where σ_n is the noise standard deviation and t_s is a threshold parameter.

4. Merge newly selected indices with the previous support $\mathcal{I}_{s-1}$ to update the support estimate

$$\mathcal{I}_s = \mathcal{I}_{s-1} \cup J_s \tag{2.8}$$

5. Project $\mathbf{y}$ on the atoms spanning the set $\mathcal{I}_s$ to find $\boldsymbol{\alpha}_s$ and compute the residual $\mathbf{r}_s$

$$\begin{aligned} \boldsymbol{\alpha}_s &= (\boldsymbol{\Phi}_{\mathcal{I}_s}^T \boldsymbol{\Phi}_{\mathcal{I}_s})^{-1} \boldsymbol{\Phi}_{\mathcal{I}_s}^T \mathbf{y} \\ \mathbf{r}_s &= \mathbf{y} - \boldsymbol{\Phi}\boldsymbol{\alpha}_s \end{aligned}$$

6. Repeat steps 2-5 until convergence.

7. Take $\hat{\boldsymbol{\alpha}} = \boldsymbol{\alpha}_s$ as the solution of StOMP.

The StOMP is developed for $\boldsymbol{\Phi}$ selected from independent and uniformly distributed random vectors on the unit sphere. For other dictionaries, like the trained overcomplete dictionaries, performance is not reported.

2.1.3 Bayesian Pursuit Algorithm (BPA)

The Bayesian hypothesis testing [97] is a powerful tool in estimation theory. In the BPA, the greedy method of selection of dictionary atoms is based on a hypothesis testing. In contrast to this, in the OMP or the StOMP once an atom is selected it is never dropped . Therefore, the BPA provides a very flexible and precise support of active atoms in the estimation of the sparse coefficients.

Modeling the sparse vector

In the BPA, the coefficient vector $\boldsymbol{\alpha} = [\alpha_1 \ \alpha_2 \ \ldots \ \alpha_K]^T$ is modelled by the Bernoulli-Gaussian (BG) model [95] where a coefficient is inactive with probability p. According to this model, each coefficient α_i can be written as

$$\alpha_i = q_i r_i, \tag{2.9}$$

where q_i represents the activity of the i^{th} coefficient and r_i represents the amplitudes of α_i. The activity q_i is a Bernoulli random variable with

$$q_i = \begin{cases} 0, \text{ with probability } p \\ 1, \text{ with probability } (1-p). \end{cases} \tag{2.10}$$

The amplitude of α_i is modelled as a zero-mean normal random variable $r_i \sim N(0, \sigma_r^2)$. The coefficient vector $\boldsymbol{\alpha}$ can be written as

$$\boldsymbol{\alpha} = \mathbf{Q}\mathbf{r}, \tag{2.11}$$

where $\mathbf{Q} = \text{diag}[q_1, q_2, \ldots, q_K]$ and $\mathbf{r} \triangleq [r_1\ r_2\ \ldots\ r_K]^T$ are activity matrix and the amplitude vector respectively. The BPA determines the activity measure of the atoms by means of a Bayesian hypothesis testing strategy on the correlation of the residual signal with the dictionary atoms. The method is briefly discussed below:

The Equation (2.3) can be rewritten as

$$\mathbf{y} = \sum_{i=1}^{K} \boldsymbol{\phi}_i \alpha_i + \mathbf{n}, \tag{2.12}$$

where $\boldsymbol{\phi}_i$ is the i^{th} atom in the dictionary scaled to have the unity norm.

The estimated correlation c_j between $\mathbf{y}$ and the j^{th} atom $\boldsymbol{\phi}_j$ is given by

$$c_j \triangleq \left\langle \mathbf{y}, \boldsymbol{\phi}_j \right\rangle = \alpha_j + \sum_{i \neq j} \alpha_i b_{ij} + v_j, \tag{2.13}$$

where $b_{ij} \triangleq \left\langle \boldsymbol{\phi}_i, \boldsymbol{\phi}_j \right\rangle$ and $v_j \triangleq \left\langle \mathbf{n}, \boldsymbol{\phi}_j \right\rangle$.

The BPA considers two hypotheses:

$$H_1 : \text{the } j^{\text{th}} \text{ atom is active}$$
$$H_2 : \text{the } j^{\text{th}} \text{ atom is inactive}$$

Assuming that the coefficients except the j^{th} one is known from the previous estimation, Equation (2.13) can be rewritten as

$$c_j - \sum_{i \neq j} \hat{\alpha}_i b_{ij} = \alpha_j + \sum_{i \neq j} (\alpha_i - \hat{\alpha}_i) b_{ij} + v_j, \tag{2.14}$$

where $\hat{\alpha}_i$ is the estimation of the i^{th} coefficient at the current iteration. Define

$$\begin{aligned} m_j &\triangleq \sum_{i \neq j} \hat{\alpha}_i b_{ij} \\ \gamma_j &\triangleq \sum_{i \neq j} (\alpha_i - \hat{\alpha}_i) b_{ij} + v_j. \end{aligned} \tag{2.15}$$

The two hypotheses H_1 and H_2 become

$$\begin{aligned} H_1 &: c_j - m_j = r_j + \gamma_j \\ H_2 &: c_j - m_j = \gamma_j, \end{aligned} \tag{2.16}$$

where m_j is known and γ_j depends on the noise. In [95], the authors consider the posterior proba-

bilities $P(H_1|c_j)$ and $P(H_2|c_j)$. The hypothesis H_1 is true if

$$P(H_1|c_j) > P(H_2|c_j) \tag{2.17}$$

Using the Bayes' rule, the above posteriors can be written as

$$P(H_1|c_j) = \frac{P(H_1)f(c_j|H_1)}{f(c_j)}, \tag{2.18}$$

and

$$P(H_2|c_j) = \frac{P(H_2)f(c_j|H_2)}{f(c_j)} \tag{2.19}$$

respectively, where $f(c_j|H_1)$ and $f(c_j|H_2)$ are likelihood functions. From the Bernoulli-Gaussian model in [95], we get

$$P(H_1) = 1 - p, \tag{2.20}$$

$$P(H_2) = p, \tag{2.21}$$

$$f(c_j|H_1) = \frac{1}{\sqrt{2\pi(\sigma^2_{\gamma_j} + \sigma^2_r)}} \exp\left(\frac{-(c_j - m_j)^2}{2(\sigma^2_{\gamma_j} + \sigma^2_r)}\right), \tag{2.22}$$

and

$$f(c_j|H_2) = \frac{1}{\sqrt{2\pi\sigma^2_{\gamma_j}}} \exp\left(\frac{-(c_j - m_j)^2}{2\sigma^2_{\gamma_j}}\right), \tag{2.23}$$

where σ^2_r is the variance of the amplitude vector $\mathbf{r}$ and $\sigma^2_{\gamma_j}$ is the variance of γ_j. Substitution of Equations (2.18) and (2.19) in Equation (2.17) leads to the following decision rule for the hypothesis testing

$$\hat{q}_j = \begin{cases} 1 & \text{if } |c_j - m_j| > \text{Th}_j \\ 0 & \text{otherwise,} \end{cases} \tag{2.24}$$

where Th_j is given by

$$\text{Th}_j \triangleq \frac{\sigma_{\gamma_j}}{\sigma_r} \sqrt{2(\sigma^2_r + \sigma^2_{\gamma_j}) \ln\left(\frac{p\sqrt{\sigma^2_r + \sigma^2_{\gamma_j}}}{(1-p)\sigma_{\gamma_j}}\right)}. \tag{2.25}$$

In the above, the parameters p and σ_r should be estimated. They are estimated by [95]

$$\begin{aligned} \hat{p} &= 1 - \frac{\|\hat{\mathbf{q}}\|_0}{K} \\ \hat{\sigma}_r &= \frac{\|\mathbf{r}\|_2}{\sqrt{K}} \end{aligned} \tag{2.26}$$

where $\hat{\mathbf{q}} = [q_1\ q_2\ \ldots\ q_K]^T$ is the activity vector corresponding to the observed signal $\mathbf{y}$ and $\|\mathbf{r}\|_2$ is

the norm of the corresponding amplitude vector. The parameter σ_{γ_j} is estimated as

$$\hat{\sigma}^2_{\gamma_j} = \hat{\sigma}^2_n + \sum_{i \neq j} b^2_{ij} \hat{\sigma}^2_{i,e_\alpha}, \tag{2.27}$$

where

$$\hat{\sigma}_n = \frac{\|\mathbf{y} - \mathbf{\Phi}\boldsymbol{\alpha}\|_2}{\sqrt{K}}, \tag{2.28}$$

is the estimation of the noise standard deviation and $\hat{\sigma}^2_{i,e_\alpha}$ is the variance of the coefficient error $e = \alpha_i - \hat{\alpha}_i$. For convergence, $\hat{\sigma}^2_{i,e_\alpha}$ is decreased linearly with a coefficient ν which is close to unity. Thus

$$\hat{\sigma}_{i,e_\alpha}(\text{new}) = \nu \hat{\sigma}_{i,e_\alpha}(\text{old}). \tag{2.29}$$

The convergence of the BPA is guaranteed if $\hat{\sigma}^2_{i,e_\alpha}$ approaches to zero.

After updating the activity vector $\mathbf{q}$ by Equation (2.24), the estimation of the amplitude vector $\mathbf{r}$ is carried out by the linear least-squares (LLS) method as

$$\hat{\mathbf{r}} = \sigma_r^2 \hat{\mathbf{Q}} \mathbf{\Phi}^T (\sigma_r^2 \mathbf{\Phi} \hat{\mathbf{Q}} \mathbf{\Phi}^T + \sigma_n^2 \mathbf{I})^{-1} \mathbf{y}, \tag{2.30}$$

where $\hat{\mathbf{Q}} = \text{diag}[\hat{q}_1, \hat{q}_2, \ldots, \hat{q}_K]$ and $\hat{\mathbf{q}} = [\hat{q}_1 \ \hat{q}_2 \ \ldots \ \hat{q}_K]^T$ is the updated activity vector. Finally, the $\hat{\boldsymbol{\alpha}}$ is obtained by Equation (2.11).

For implementation, the BPA is initialized with an ℓ^2-norm solution and the parameters $p^{(0)}$, $\sigma_r^{(0)}$, and $\sigma_n^{(0)}$ are initialized using the following:

$$\begin{aligned} \hat{p}^{(0)} &= 0.8 \\ \hat{\sigma}_r^{(0)} &= \frac{\|y\|_2}{\sqrt{m\,(1 - \hat{p}^{(0)})}} \\ \hat{\sigma}_n^{(0)} &= \frac{\hat{\sigma}_r^{(0)}}{5} \end{aligned} \tag{2.31}$$

It has been reported in [95] that the BPA outperforms the OMP, and the StOMP in terms of the estimation error at low noise levels. However, the computational complexity of the BPA is the highest compared to that of the OMP and the StOMP.

2.2 Proposed Modification of the BPA

2.2.1 Motivation

The BPA requires an approximate solution and an estimate for p to start the iteration. The BPA is initialized with the ℓ^2-norm solution and p is fixed by trial and error [98]. We refer hereafter the

original BPA algorithm as the *standard BPA* (SBPA). The following observations are made on the SBPA:

1. The ℓ^2-norm solution that SBPA uses as the initial solution, is not a sparse solution. The initialization of the SBPA with the ℓ^2-norm solution may not be the best initialization. Depending on $\mathbf{\Phi}$, it may be strongly biased towards a particular solution [88].

2. The SBPA is initialized with a constant p fixed by trial and error and on the assumption that there should be sufficient number of active atoms. It is worthwhile to investigate the role of the initial value of p in the quality of final solution at various noise levels.

3. After each iteration of the SBPA, the σ_{i,e_α} is assumed to decrease linearly with a proportionality constant ν whose value is taken to be close to unity. Finally the iteration stops when σ_{i,e_α} becomes zero and $\sigma_{\gamma_j} \approx \sigma_n$. Therefore, there is scope to design for a better stopping criterion for the convergence of the algorithm.

4. It is worthwhile to investigate the denoising performance of the standard BPA on real images. These points are investigated below:

2.2.2 Performance of the Standard BPA for Different Initial Solutions and Estimates of p

To address the issues in 1-3, the SBPA is initialized with different initial solutions and estimates of p and found the root mean square error (RMSE) in each of the representations. The following cases are considered:

1. Take the true solution as the initial solution and the true p as the initial estimate of p.

2. Take the ℓ^2-norm solution $\boldsymbol{\alpha}^* = \mathbf{\Phi}^\dagger \mathbf{y}$,

   where $\mathbf{\Phi}^\dagger$ is the pseudo inverse of $\mathbf{\Phi}$ given by $\mathbf{\Phi}^T(\mathbf{\Phi}\mathbf{\Phi}^T)^{-1}$. Assume the true value of p as the initial estimate of p.

3. Take an approximate sparse solution obtained by hard thresholding the ℓ^2-norm solution as the initial solution and the true value of p as the initial estimate of p.

4. Take an approximate sparse solution and estimate p from it according to Equation (2.26).

The SBPA is allowed to run for 20 iterations for each of the cases. The details of the experiment is given in the section on Experimental Results. The following observations are made on a case-by-case basis:

1. *BPA with true initial solution and true p as the initial estimate of p:*

   The RMSE by the BPA with this initial solution (detailed in the results section) is lower than that for the SBPA at different noise levels.

2. *BPA with the ℓ^2-norm initialization and true value of p as the initial estimate of p:*

   The RMSE of this representation is found to be higher than the SBPA.

3. *BPA with an approximately sparse initial solution and the true value of p as the initial estimate of p:*

   A better quality of solution is obtained with the sparse initialization compared to that by the SBPA in terms of the RMSE at different noise levels.

4. *BPA with an approximately sparse initial solution and the estimated value of p:*

   Finally, the sparse initialization and an estimate of p from the sparse initial solution yield a better solution than that by the SBPA. The RMSE of the final solution is lower compared to the SBPA.

The details of these experiments are presented in the results section. From the above observations we conclude that the quality of solution of the SBPA depends on the initial sparse solution and the initial estimate for p.

2.2.3 Stopping Criterion

The stopping criterion of the OMP [56,99] can be adopted for the BPA. Let $\boldsymbol{\alpha}$ be the sparse solution so that the residual $\mathbf{r}_{\mathrm{s}} = \mathbf{y} - \boldsymbol{\Phi}\boldsymbol{\alpha}$. Then a threshold on the RMSE can be used as a stopping criterion, where

$$\mathrm{RMSE} = \frac{\|\mathbf{r}_{\mathrm{s}}\|_2}{\sqrt{m}}. \tag{2.32}$$

We may threshold the RMSE by

$$\frac{\|\mathbf{r}_{\mathrm{s}}\|_2}{\sqrt{m}} \leqslant C\sigma_n, \tag{2.33}$$

where C is a constant and σ_n is the standard deviation of the noise. The equivalent condition is

$$\frac{\|\mathbf{r}_s\|_2^2}{\sigma_n^2} \leqslant mC^2. \tag{2.34}$$

In [99], the authors suggest a simple procedure to estimate C. Assuming $\mathbf{r}_s$ to be Gaussian, the random variable $V = \frac{\|\mathbf{r}_s\|_2^2}{\sigma_n^2}$ will be χ_m^2 distributed, with the probability density function:

$$f_V(v) = \begin{cases} \dfrac{v^{m/2-1}}{2^{m/2}\Gamma(m/2)} e^{-m/2}, & v \geqslant 0 \\ 0, & v < 0. \end{cases} \tag{2.35}$$

Therefore, C can be found by thresholding the probability:

$$\mathrm{P}\left(\frac{\|\mathbf{r}_s\|_2^2}{\sigma_n^2} \leqslant mC^2\right) = \int_0^{mC^2} \frac{v^{m/2-1}}{2^{m/2}\Gamma(m/2)} e^{-m/2} dv. \tag{2.36}$$

A good choice for the threshold on this probability is 0.9. With this probability and $m = 64$, one gets $C = 1.15$.

2.2.4 The Modified BPA

On the basis of the above discussion, we propose the modified BPA that includes: (1) a sparse initialization obtained by hard thresholding the ℓ^2-norm solution (2) the estimation of p from the initial sparse solution using Equation (2.26) and (3) a stopping criterion as stated above.

To find the sparse initial solution from $\boldsymbol{\alpha}^0$, a method similar to the one applied in the StOMP algorithm [92] is adopted. The correlation c_k of each atom $\boldsymbol{\phi}_k$ in $\boldsymbol{\Phi}$ with the observed data $\mathbf{y}$ is measured by the relation:

$$c_k = \boldsymbol{\phi}_k^T \mathbf{y}. \tag{2.37}$$

Considering all the atoms in $\boldsymbol{\Phi}$, we get the correlation vector

$$\mathbf{c} = \boldsymbol{\Phi}^T \mathbf{y}. \tag{2.38}$$

The correlation values may be thresholded to get the significant atoms. A reasonable way to threshold the correlation values is given by the relation:

$$c_k \text{ is significant if } |c_k| \geqslant t\sigma_c, \tag{2.39}$$

where σ_c is the estimated standard deviation of $\mathbf{c}$ and t is a suitable constant. The atom $\boldsymbol{\phi}_k$ is retained if c_k is significant. Suppose $J = \{j : c(j) > t\sigma_c\}$ is the set of indices of significant atoms.

Then the initial sparse solution $\boldsymbol{\alpha}_j^0$ is obtained by:

$$\boldsymbol{\alpha}_j^0 = \begin{cases} \boldsymbol{\alpha}_j^*, & \text{for } j \in J \\ 0, & \text{otherwise.} \end{cases}, \tag{2.40}$$

where $\boldsymbol{\alpha}_j^*$ is the ℓ^2-norm solution. The modified BPA is shown by a block diagram in Fig. 2.1. The

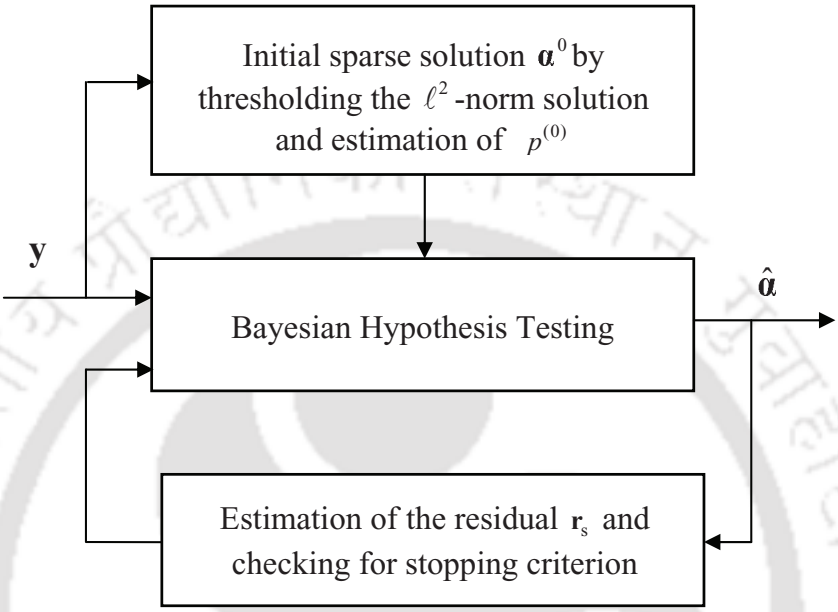

Fig. 2.1: Modified BPA

algorithm can be summarized as follows:

Algorithm 1 Modified BPA

1: Obtain the ℓ^2-norm solution $\boldsymbol{\alpha}^* = \boldsymbol{\Phi}^\dagger \mathbf{y}$.
2: Find an initial sparse solution $\boldsymbol{\alpha}^0$ as follows

   i. Compute the correlation vector $\mathbf{c} = \boldsymbol{\Phi}^{\boldsymbol{T}} \mathbf{y}$.

   ii. Obtain $\boldsymbol{\alpha}^0$ using Equation (2.40).

3: Estimate $\hat{p}^{(0)} = 1 - \frac{\|\boldsymbol{\alpha}^0\|_0}{K}$.
4: Estimate $\hat{\sigma}_r^{(0)}$, and $\hat{\sigma}_n^{(0)}$ using Equation (2.31).
5: Find the set of active atoms and the sparse solution using the Bayesian hypothesis testing.
6: Update $\hat{p}$, $\hat{\sigma}_r$, and $\hat{\sigma}_n$ using Equations (2.26) and (2.28) respectively.
7: Compute the residual as discussed in Section 2.2.3.
8: Check the stopping condition, if it is true then stop and take the current solution as the final solution otherwise go to step 5 and repeat the steps 5-8.

In the following section, we propose an image denoising algorithm using the modified BPA.

2.3 Image Denoising by the Modified BPA Algorithm

Consider an ideal noise free image $\mathbf{x}$ of size $\sqrt{m} \times \sqrt{m}$ and $\mathbf{y}$ be the noisy version of it. The problem of estimation of $\mathbf{x}$ from $\mathbf{y}$ under the assumption that $\mathbf{x}$ is sparse over a dictionary has two essential issues: (1) to find a dictionary $\mathbf{\Phi}$ which permits a sparse representation of the signal and (2) to find the coefficients of this sparse representation. The second issue can be addressed by the modified BPA discussed above. As pointed out in Chapter 1, there are two ways to address the issue of finding the dictionary. The dictionary can be chosen either from a set of prespecified basis functions or can be learned from the given data. In [68], Aharon *et al.* show that the K-SVD is a very efficient strategy for dictionary learning. The K-SVD based dictionary learning is outlined below.

2.3.1 K-SVD Based Dictionary Learning

Consider $\mathbf{Y} = [\mathbf{y}_1\ \mathbf{y}_2\ ....\ \mathbf{y}_M]$, be the dataset to learn the dictionary $\mathbf{\Phi}$, where M is the total number of training signals in the dataset. Each example $\mathbf{y}_i$ gives a sparse representation $\boldsymbol{\alpha}_i$ with respect to the dictionary $\mathbf{\Phi}$. Therefore, we can write

$$\mathbf{y}_i = \mathbf{\Phi}\boldsymbol{\alpha}_i + \mathbf{n}, \quad \text{for } i = 1, 2, \ldots, M. \tag{2.41}$$

The K-SVD algorithm aims at finding the best possible dictionary for the sparse representation of the example set $\mathbf{Y}$. It solves the following optimization problem:

$$\begin{aligned} &\min_{\mathbf{\Phi},\mathbf{A}} \left\{ \|\mathbf{Y} - \mathbf{\Phi}\mathbf{A}\|_F^2 \right\} \\ &\text{subject to } \forall i, \quad \|\boldsymbol{\alpha}_i\|_0 \leqslant T_0, \end{aligned} \tag{2.42}$$

where $\|.\|_F$ represents the Frobenius norm, $\mathbf{A} = [\boldsymbol{\alpha}_1\ \boldsymbol{\alpha}_2\ \ldots\ \boldsymbol{\alpha}_M]$, and T_0 is a fixed number.

Alternatively, a similar objective can be met by solving

$$\begin{aligned} &\min_{\mathbf{\Phi},\boldsymbol{\alpha}} \sum_{i=1}^{M} \|\boldsymbol{\alpha}_i\|_0 \\ &\text{subject to } \|\mathbf{Y} - \mathbf{\Phi}\mathbf{A}\|_F^2 \leqslant \varepsilon^2, \end{aligned} \tag{2.43}$$

where ε is a constant depending on the mean-square representation error and variance of the noise. The K-SVD algorithm solves the minimization problem in Equation (2.42) iteratively in two stages:

Sparse coding stage

Assuming the dictionary $\mathbf{\Phi}$ as fixed and has ℓ^2 normalized columns, the cost function in Equation (2.42) can be rewritten as

$$\|\mathbf{Y} - \mathbf{\Phi A}\|_F^2 = \sum_{i=1}^{M} \|\mathbf{y}_i - \mathbf{\Phi}\boldsymbol{\alpha}_i\|_2^2. \tag{2.44}$$

Therefore, the problem in Equation (2.42) can be decoupled to M distinct problems of the form

$$\begin{aligned} &\min_{\boldsymbol{\alpha}_i} \|\mathbf{y}_i - \mathbf{\Phi}\boldsymbol{\alpha}_i\|_2^2 \\ &\text{subject to } \|\boldsymbol{\alpha}_i\|_0 \leqslant T_0 \\ &\text{for } i = 1, 2, \ldots, M. \end{aligned} \tag{2.45}$$

This problem can be solved by one of the pursuit algorithms discussed in Section 2.1.

Dictionary update using SVD

The dictionary $\mathbf{\Phi}$ is updated one column at a time using the *singular value decomposition* (SVD). From Equation (2.42), the term $\mathbf{\Phi A}$ can be written as a sum of K rank-1 matrices. That is

$$\begin{aligned} \|\mathbf{Y} - \mathbf{\Phi A}\|_F^2 &= \left\| \mathbf{Y} - \sum_{j=1}^{K} \boldsymbol{\phi}_j \boldsymbol{\alpha}_R^j \right\|_F^2 \\ &= \left\| \mathbf{E}_k - \boldsymbol{\phi}_k \boldsymbol{\alpha}_R^k \right\|_F^2, \end{aligned} \tag{2.46}$$

where

$$\mathbf{E}_k = \mathbf{Y} - \sum_{j \neq k} \boldsymbol{\phi}_j \boldsymbol{\alpha}_R^j, \tag{2.47}$$

and $\boldsymbol{\alpha}_R^k$ is the k^{th} row of the matrix $\boldsymbol{\alpha}$ which uses the atom $\boldsymbol{\phi}_k$.

In order to introduce the sparsity while updating each atom, the authors in [68] consider only those examples (signals) which use the k^{th} atom in the dictionary to be updated. Suppose $\mathcal{I}_k$ is a set of indices pointing to the examples from $\{\mathbf{y}_1, \mathbf{y}_2, \ldots, \mathbf{y}_M\}$ that use the atom $\boldsymbol{\phi}_k$. Thus,

$$\mathcal{I}_k = \left\{ i |\ 1 \leqslant i \leqslant K,\ \alpha_R^k(i) \neq 0 \right\}. \tag{2.48}$$

Define a matrix $\mathbf{\Omega}_k$ of size $M \times |\mathcal{I}_k|$ such that

$$\mathbf{\Omega}_k(i,j) = \begin{cases} 1, \text{ if } i = \mathcal{I}_k(j) \\ 0, \text{ otherwise.} \end{cases} \tag{2.49}$$

The matrix $\mathbf{E}_k^R$ of size $m \times |\mathcal{I}_k|$ is then given by

$$\mathbf{E}_k^R = \mathbf{E}_k \mathbf{\Omega}_k. \tag{2.50}$$

$\mathbf{E}_k^R$ in the above equation is substituted for $\mathbf{E}_k$ in the minimization problem in Equation (2.47). The optimal solution for $\boldsymbol{\phi}_k$ is now obtained by the singular value decomposition of the $\mathbf{E}_k^R$ matrix [100] given by:

$$\mathbf{E}_k^R = \mathbf{U}\mathbf{\Delta}\mathbf{V}^T, \tag{2.51}$$

where

$$\mathbf{U} = [\mathbf{u}_1\ \mathbf{u}_2\ \ldots\ \mathbf{u}_m] = \text{Eigenvectors of } \mathbf{E}_k^R \left(\mathbf{E}_k^R\right)^T \tag{2.52}$$

$$\mathbf{V} = [\mathbf{v}_1\ \mathbf{v}_2\ \ldots\ \mathbf{v}_{|\mathcal{I}_k|}] = \text{Eigenvectors of } \left(\mathbf{E}_k^R\right)^T \mathbf{E}_k^R \tag{2.53}$$

$$\mathbf{\Delta} = \text{square roots of the nonzero eigenvalues of } \mathbf{E}_k^R \left(\mathbf{E}_k^R\right)^T \text{ or } \left(\mathbf{E}_k^R\right)^T \mathbf{E}_k^R. \tag{2.54}$$

The dictionary updation stage can be summarized as follows:

Algorithm 2 Dictionary update using the K-SVD [68]

1: $k = 0$.
2: **repeat**
3: $k = k + 1$.
4: For an atom $\boldsymbol{\phi}_k$ and $\boldsymbol{\alpha}$
5: Obtain $\mathbf{E}_k$ in Equation (2.47) and then find $\mathbf{E}_k^R$ in Equation (2.50).
6: Consider the minimization of $\left\|\mathbf{E}_k^R - \boldsymbol{\phi}_k \boldsymbol{\alpha}_R^k\right\|_F^2$
7: Perform SVD on $\mathbf{E}_k^R$ using Equation (2.51).
8: Update $\boldsymbol{\phi}_k$ by $\mathbf{u}_1$ in Equation (2.52).
9: Update $\boldsymbol{\alpha}_R^k$ by
$\boldsymbol{\alpha}_R^k = \Delta(1,1)\mathbf{v}_1$,
where $\mathbf{v}_1$ and $\Delta(1,1)$ are obtained by Equation (2.53) and Equation (2.54) respectively.
10: **until** $k = K$

2.4 K-SVD Based Image Denoising

In [56], Elad and Aharon present an image denoising method using the sparse representation over a learned overcomplete dictionary obtained by applying the K-SVD, on overlapping patches of the image. It is assumed that the image $\mathbf{x}$ has a sparse representation in each patch of dimension $\sqrt{m}_p \times \sqrt{m}_p$. Addressing image denoising as a sparse decomposition problem in each patch leads to

the following energy minimization problem:

$$\left\{\hat{\boldsymbol{\alpha}}_i, \hat{\boldsymbol{\Phi}}, \hat{\mathbf{x}}\right\}_{i=1,2,\ldots,M} = \arg \min_{\boldsymbol{\Phi},\boldsymbol{\alpha}_i,\mathbf{x}} \left\{\gamma \left\|\mathbf{x}-\mathbf{y}\right\|_2^2 + \sum_i \lambda_i \left\|\boldsymbol{\alpha}_i\right\|_0 + \sum_i \left\|\boldsymbol{\Phi}\boldsymbol{\alpha}_i - \mathbf{L}_i\mathbf{x}\right\|_2^2\right\}, \tag{2.55}$$

where i marks the location of the patch in the image and γ is a penalty parameter related to the noise variance and λ is the sparsity inducing regularization term. $\hat{\boldsymbol{\alpha}}_i$ are the sparse representation for the i^{th} patch using $\hat{\boldsymbol{\Phi}}$. The operator $\mathbf{L}_i$ is a binary matrix $m_p \times m$ which extracts the $\sqrt{m}_p \times \sqrt{m}_p$ patch from the i^{th} location in the image. The above problem is solved in two stages:

1. *Sparse coding stage*

   It is assumed that $\boldsymbol{\Phi}$ is known and the minimization problem in Equation (2.55) consists of only two unknowns, namely, $\boldsymbol{\alpha}$ and $\mathbf{x}$. Then with the initialization $\mathbf{x} = \mathbf{y}$, the problem can be decoupled into smaller problems of the form:

   $$\hat{\boldsymbol{\alpha}}_i = \arg \min_{\boldsymbol{\alpha}_i} \left\{\lambda_i \left\|\boldsymbol{\alpha}_i\right\|_0 + \left\|\boldsymbol{\Phi}\boldsymbol{\alpha}_i - \mathbf{L}_i\mathbf{x}\right\|_2^2\right\}. \tag{2.56}$$

   The above optimization problem is solved by a pursuit algorithm like the OMP and the modified BPA in the present case.

2. *Dictionary update stage*

   After finding all $\hat{\boldsymbol{\alpha}}_i$ as above, the dictionary is updated one column at a time using the algorithm discussed in 2.3.1.

The above two stages are carried out iteratively till the convergence of the results. After getting all $\hat{\boldsymbol{\alpha}}_i$ (corresponding to all the patches in the image) and the $\hat{\boldsymbol{\Phi}}$ as above, the problem in Equation (2.55) becomes

$$\hat{\mathbf{x}} = \arg \min_{\mathbf{x}} \gamma \left\|\mathbf{x}-\mathbf{y}\right\|_2^2 + \sum_i \left\|\mathbf{L}_i\mathbf{x} - \hat{\boldsymbol{\Phi}}\hat{\boldsymbol{\alpha}}_i\right\|_2^2. \tag{2.57}$$

The above is a quadratic optimization problem has the closed-form solution given by

$$\hat{\mathbf{x}} = \left[\gamma\mathbf{I} + \sum_i \mathbf{L}_i^T\mathbf{L}_i\right]^{-1}\left[\gamma\mathbf{y} + \sum_i \mathbf{L}_i^T\hat{\boldsymbol{\Phi}}\hat{\alpha}_i\right], \tag{2.58}$$

where $\mathbf{I}$ is the identity matrix.

The K-SVD based image denoising is shown to have the state-of-the-art performance for the removal of additive white Gaussian noise [56].

Based on the above discussion we propose to apply the modified BPA for the removal of additive white Gaussian noise using a dictionary obtained by applying the K-SVD algorithm on the noisy

image. The sparse coding stage of the standard K-SVD is performed using the modified BPA. The algorithm can be summarized as follows:

Algorithm 3 Denoising algorithm using the modified BPA

1: Goal: denoise a given image $\mathbf{y}$ corrupted by AWGN.
2: Initialize the dictionary with overcomplete DCT and normalize its columns to have unit ℓ^2 norm.
3: **repeat**
4: *Sparse coding stage:* Apply the modified BPA in subsection 2.2.4 to obtain the sparse coefficients $\hat{\boldsymbol{\alpha}}_i$ for each patch by solving the minimization problem in Equation (2.56) .
5: *Dictionary update stage:* Apply the algorithm discussed in subsection 2.3.1 to update the dictionary one column at a time and obtain $\hat{\boldsymbol{\Phi}}$.
6: **until** convergence
7: Estimate the denoised image by using Equation (2.58).

2.5 Experimental Results

The first set of experiments are performed to evaluate the performance of the modified BPA. It is reported in the following subsection.

2.5.1 Performance Evaluation of the Modified BPA

We use a random dictionary matrix with normalized columns. The test data are generated by the model in Equation (2.1). An overcomplete dictionary of size 256×512 is considered. The components of each atom in $\boldsymbol{\Phi}$ are generated using a pseudo-random number generator that generates uniform random numbers in the range [-1, 1]. The coefficient vector $\boldsymbol{\alpha}$ is generated using a Gaussian random number generator and assuming zero values to 90% of the randomly selected coefficients ($p = 0.9$). The noisy data is generated by the model in Equation (2.3). We consider AWGN with standard deviations in the range 0.02-0.2 to get different sets of noisy data. The representation performance of the algorithm is measured by the following measures.

1. The RMSE of the sparse coefficient vector given by

$$\|\hat{\boldsymbol{\alpha}}_{\mathbf{0},\boldsymbol{\varepsilon}} - \boldsymbol{\alpha}_{\mathbf{0}}\|_2 , \tag{2.59}$$

where $\hat{\boldsymbol{\alpha}}_{\mathbf{0},\boldsymbol{\varepsilon}}$ is the representation of $\mathbf{y}$, and $\boldsymbol{\alpha}_{\mathbf{0}}$ is the representation of the corresponding noise free signal $\mathbf{x}$. The subscript $\mathbf{0}$ here represents the case when the noise vector is zero.

2. The RMSE of reconstruction given by

$$\|\mathbf{\Phi}\hat{\boldsymbol{\alpha}}_{\mathbf{0},\boldsymbol{\varepsilon}} - \mathbf{y_0}\|_2 , \tag{2.60}$$

where $\mathbf{y_0} = \mathbf{x} = \mathbf{\Phi}\boldsymbol{\alpha_0}$.

The average performance is obtained by considering 100 sparse representation problems. For each problem, the sparsity is kept constant and the dictionary, the sparse vector, and the noise vector are randomly chosen. The initial values of the parameters p are estimated by Equation (2.26). σ_r and σ_n are initialized according to Equation (2.31). For the BPA, we have chosen the initialization given by Equation (2.31). The BPA is run for 20 iterations and for convergence the parameter ν in Equation (2.29) is selected as 0.95.

A. Performance of the BPA with different initial solutions and values of p

In this experiment, we study the performance of the BPA for different initial solutions and initial estimates of p as enumerated in subsection 2.2.2. We compare the RMSE of the representation error for the BPA at different noise levels (σ_n) with different initial solutions and initial values of p with that of the SBPA. Fig. 2.2a shows the plots of the RMSE vs. σ_n. It clearly shows that the performance of the BPA depends on the initialization. It is interesting to note that the RMSE for the BPA initialized with the ℓ^2-norm solution and true value of p is the highest at different noise levels. This shows that the ℓ^2-norm solution is not an optimal solution for initialization of the BPA. The RMSE of the modified BPA is lower compared to the SBPA at different noise levels.

Fig. 2.2b shows the corresponding RMSE of the reconstruction for various initialization methods as discussed above for the BPA at different noise levels. The results show that the BPA initialized with the ℓ^2-norm initialization and the true value of p gives the highest reconstruction error at different noise levels. The modified BPA has a comparatively lower RMSE than the SBPA at different noise levels. Finally, the BPA with sparse initial solution and true value of p has the lowest RMSE of reconstruction among all the methods at different noise levels.

These results suggest the need for sparse initial solution for the better performance of the BPA.

B. Convergence of the modified BPA

In this experiment, we observed the rate of convergence of the modified BPA and the SBPA to the true parameters. Table 2.1 shows the iterative estimation of the parameters, namely, $\hat{p}$, $\hat{\sigma}_r$ and $\hat{\sigma}_n$ to their actual values. Fig. 2.3 shows the corresponding plots. It is observed that the modified BPA

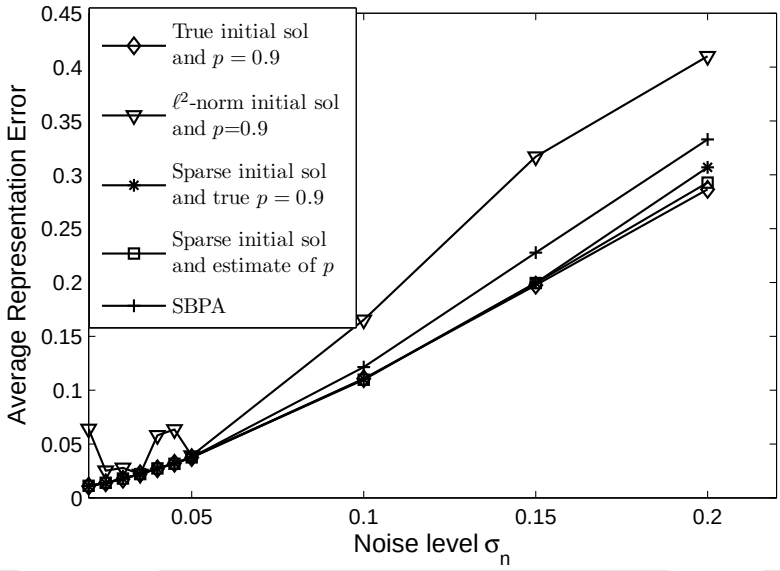

(a)

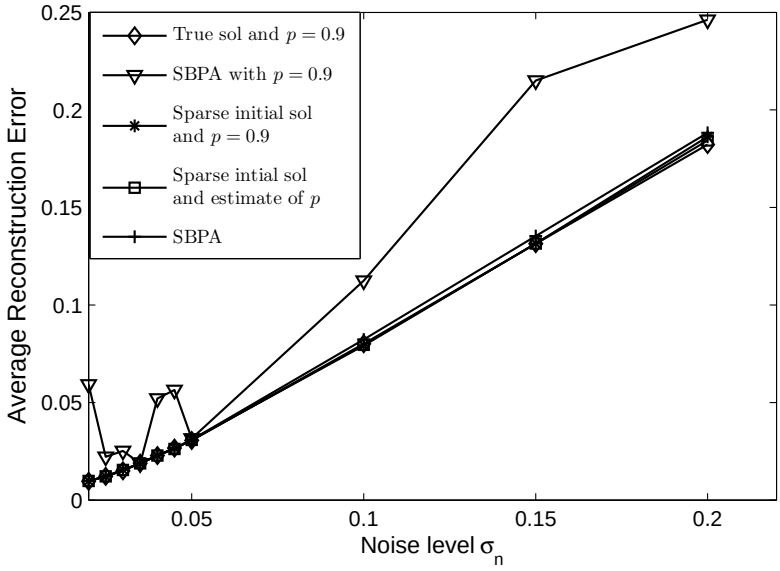

(b)

Fig. 2.2: (a) RMSE of representation for BPA with different initializations and the SBPA and (b) RMSE of reconstruction for BPA with different initializations and the SBPA.

algorithm converges faster to the true values than the SBPA.

Table. 2.1: Convergence of (a) the SBPA and (b) the modified BPA to the actual parameters: $K = 512$, $m = 256$, $p = 0.9$, $\sigma_r = 0.3098$ and $\sigma_n = 0.01$.

(a)

Iteration number	$\hat{p}$	$\hat{\sigma}_r$	$\hat{\sigma}_n$
1	0.8000	0.7189	0.1438
2	0.8887	0.2715	0.0846
3	0.8301	0.2738	0.0324
4	0.8457	0.3052	0.0087
5	0.8789	0.3144	0.0061
6	0.9004	0.3153	0.0062
7	0.9004	0.3153	0.0062

(b)

Iteration number	$\hat{p}$	$\hat{\sigma}_r$	$\hat{\sigma}_n$
1	0.8516	0.7582	0.1516
2	0.9004	0.2994	0.0152
3	0.8965	0.3146	0.0059
4	0.9004	0.3158	0.0058
5	0.9004	0.3159	0.0059
6	0.9004	0.3159	0.0059
7	0.9004	0.3159	0.0059

C. Comparison of the modified BPA with different pursuit algorithms

This experiment is carried out to compare the performance of the modified BPA with selected greedy pursuit algorithms. Fig. 2.4a shows the performance of the OMP, the StOMP, the SBPA and the proposed algorithm in terms of representation errors at different noise levels. For OMP and StOMP algorithms, (implemented by SparseLab[1]) we use 50 and 20 iterations respectively. The number of iterations for the OMP is chosen more than the StOMP because it takes more number of iterations to converge. In order to make a fair comparison of the performances of the various pursuit algorithms with that of the BPA, we consider the number of iterations of the OMP and the StOMP to be exactly the same as reported in [95]. The sensitivity parameter in StOMP for threshold selection is chosen as 0.5. It is clearly observed that the modified BPA outperforms the SBPA in terms of the RMSE of the representation error at different noise levels. Fig. 2.4b shows the reconstruction error for the various pursuit algorithms at different noise levels. The proposed algorithm clearly outperforms the SBPA at different noise levels. It is also observed that the modified BPA provides low representation and reconstruction errors at low noise levels compared to that of the OMP and

[1]The codes SolveOMP, SolveStOMP are publicly available at http://sparselab.stanford.edu

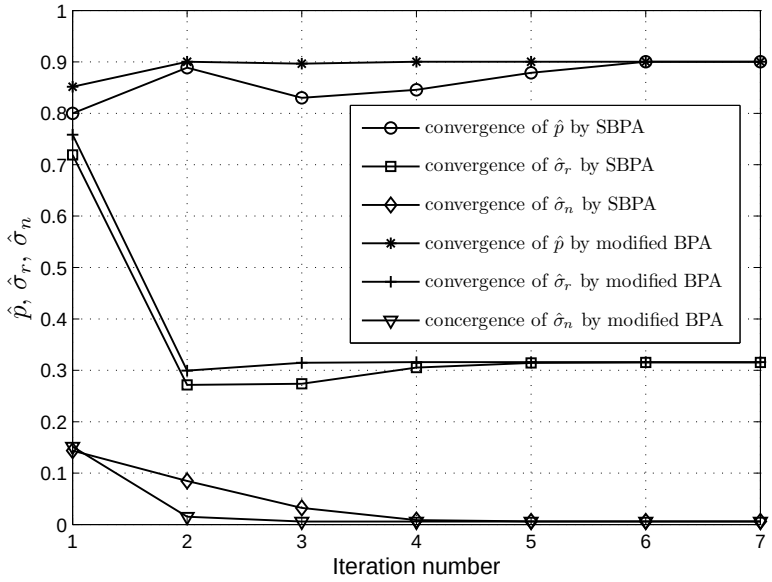

Fig. 2.3: Convergence of the SBPA and the modified BPA to the true parameters.

the StOMP. However, at high noise levels the performance of the OMP and the StOMP found to be better than the modified BPA. The performance of the OMP in terms of the RMSEs is consistently superior at high noise levels. It is interesting to note that the performance of the StOMP also deteriorates with the increased noise levels. The poor performance of the SBPA and the modified BPA at high noise levels calls for further investigation.

In the following subsection, denoising of photographic test images corrupted by AWGN at different values of σ_n using the modified BPA is reported.

2.5.2 Image denoising through the Modified BPA

In this set of experiments, we apply the modified BPA for the removal of additive white Gaussian noise from a number of images. The performance of the algorithm is verified with the test images of "Lena", "cameraman" and "Peppers" at different noise levels. The first image is of size 512×512 and the rest are of size 256×256. All these images are corrupted with additive white Gaussian noise at different values of σ_n for experimentation. The dictionary is initialized with the overcomplete DCT. We have selected overlapping patches of size 8×8 for learning a dictionary of size 64×256 using the K-SVD method discussed in subsection 2.3.1. The learning converges usually in 5-10 iterations. We select $\gamma = \frac{30}{\sigma_n}$ in Equation (2.58) for all the experiments. We have considered the following performance indices for quantitative analysis of the denoised outputs:

1. *Peak signal-to-noise ratio* (PSNR)

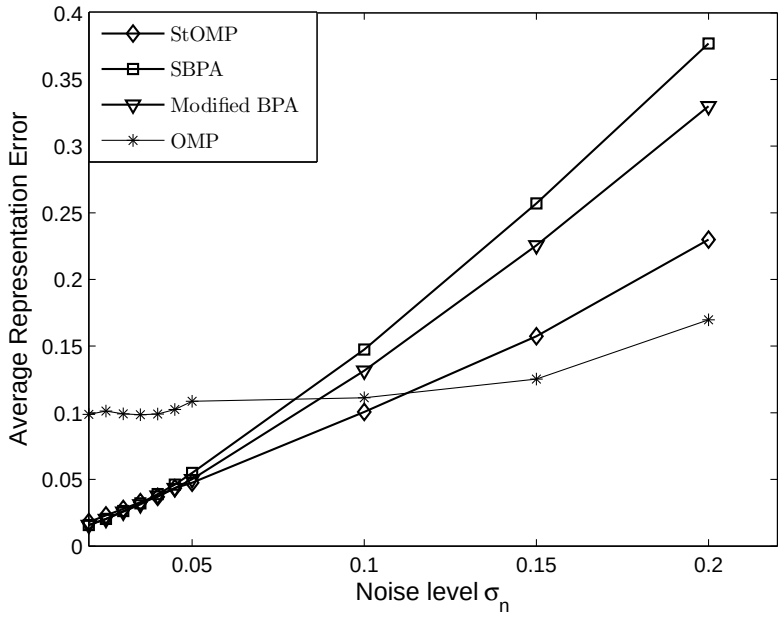

(a)

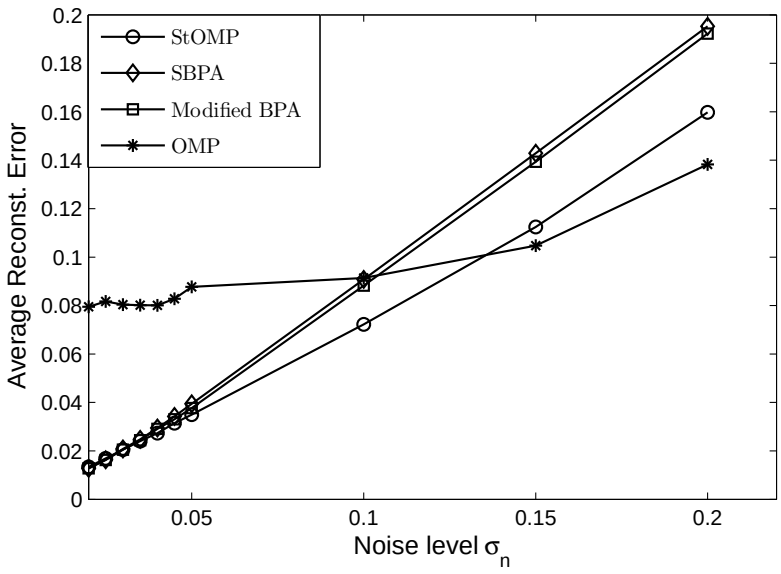

(b)

Fig. 2.4: (a) RMSE of representation for different pursuit algorithms and the modified BPA and (b) RMSE of reconstruction for different pursuit algorithms and the modified BPA.

The PSNR is given by

$$\text{PSNR} = 10\log_{10}\left(\frac{x_{\text{MAX}}^2}{\text{MSE}}\right), \tag{2.61}$$

where x_{MAX} is the maximum gray level (for an 8-bit gray-scale image, $x_{\text{MAX}} = 255$) in the original image and MSE represents the mean-square error between the original image and the filtered image. The larger PSNR values correspond to good image quality.

2. *Structural similarity index* (SSIM)

The SSIM between two images [101] is computed as

$$\text{SSIM} = \frac{(2\overline{x}\overline{\hat{x}} + C_1)(2\sigma_{x\hat{x}} + C_2)}{(\overline{x}^2 + \overline{\hat{x}}^2 + C_1)(\sigma_x^2 + \sigma_{\hat{x}}^2 + C_2)}, \tag{2.62}$$

where

$$\begin{aligned} C_1 &= (0.01 \times x_{\text{MAX}})^2 \\ C_2 &= (0.03 \times x_{\text{MAX}})^2 \\ \sigma_x^2 &= \frac{1}{m}\sum_{i=1}^{m}(x_i - \overline{x})^2 \\ \sigma_{\overline{x}}^2 &= \frac{1}{m}\sum_{i=1}^{m}(\overline{x}_i - \overline{\hat{x}})^2 \\ \sigma_{x\hat{x}} &= \sqrt{\frac{1}{m}\sum_{i=1}^{m}(x_i - \overline{x})(\hat{x}_i - \overline{\hat{x}})} \end{aligned} \tag{2.63}$$

and $\overline{x}$ and $\overline{\hat{x}}$ are the mean of the original image $\mathbf{x} = [x_1\ x_2\ \ldots\ x_m]^T$ and the denoised image $\hat{\mathbf{x}} = [\hat{x}_1\ \hat{x}_2\ \ldots\ \hat{x}_m]^T$, respectively. The SSIM values lie between -1 and 1. For good quality of denoised output, the value of SSIM should be close to unity.

The SSIM is a well-known quality metric used to measure the similarity between two images. It is considered to be correlated with the quality perception of the human visual system (HVS). The SSIM performs better than the PSNR in discriminating structural content in images. Table 2.2 summarizes the denoising results in terms of PSNR and SSIM for the test images mentioned above. The results show that the proposed method outperforms the OMP based K-SVD method for different noise levels $\sigma_n = 2$ to 10. Over a wide class of images, the proposed method outperforms K-SVD+OMP up to a noise level with standard deviation 12 in terms of both PSNR and SSIM. For $\sigma_n > 12$, the performance of the OMP based K-SVD method is better than the proposed method. Every result reported is an average over 5 experiments, having different realizations of the noise. Figs. 2.5-2.7 show the denoising results at different values of σ_n for the "Lena" image. From the figures, it can be seen that the proposed method produce visually better outputs than the OMP based method

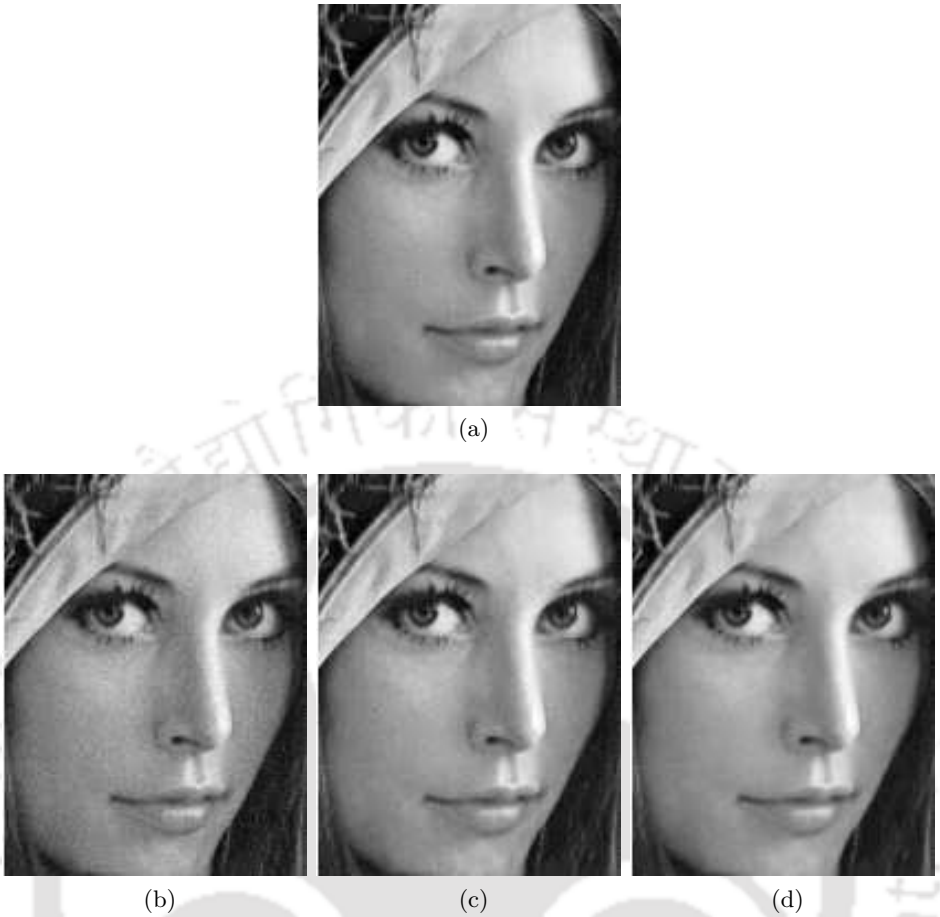

(a)

(b) (c) (d)

Fig. 2.5: (a) Original image. (b) Noisy image with $\sigma_n = 5$ and results for K-SVD based denoising (c) by OMP and (d) by proposed method.

(a) (b) (c)

Fig. 2.6: (a) Noisy image with $\sigma_n = 10$ and results for K-SVD based denoising (b) by OMP and (c) by proposed method.

at low noise levels. This is further verified for other test images corrupted by different values of σ_n. The results are shown in Figs. 2.8-2.13. These results confirm that the K-SVD based denoising using the modified BPA can remove the additive white Gaussian noise successfully only at low noise levels. But for higher noise levels ($\sigma_n > 10$) the performance of the OMP based method is better as observed on the "Lena" image.

(a) (b) (c)

Fig. 2.7: (a) Noisy image with $\sigma_n = 20$ and results for K-SVD based denoising (b) by OMP and (c) by proposed method.

(a)

(b) (c) (d)

Fig. 2.8: (a) Original image. (b) Noisy image with $\sigma_n = 5$ and results for K-SVD based denoising (c) by OMP and (d) by proposed method.

Table. 2.2: Comparison of PSNR (dB) and SSIM for the filtered test images

Image	σ_n	PSNR		SSIM	
		K-SVD+OMP	Proposed Method	K-SVD+OMP	Proposed Method
Lena	2	43.51	44.61	0.9777	0.9798
Cameraman		43.78	44.03	0.9750	0.9858
Peppers		35.68	37.32	0.9525	0.9732
Lena	5	38.58	38.91	0.9341	0.9439
Cameraman		37.63	38.10	0.9450	0.9518
Peppers		33.18	36.28	0.9202	0.9529
Lena	7	36.29	36.84	0.9246	0.9305
Cameraman		43.78	44.03	0.9750	0.9858
Peppers		32.82	35.40	0.9177	0.9346
Lena	10	35.22	35.90	0.8444	0.8824
Cameraman		32.91	32.96	0.9050	0.9150
Peppers		31.34	33.52	0.8962	0.9110
Lena	15	33.32	32.20	0.8010	0.7988
Cameraman		31.20	30.32	0.8858	0.8750
Peppers		30.72	29.72	0.8693	0.8583
Lena	20	32.38	30.20	0.7556	0.6588
Cameraman		28.47	27.92	0.7780	0.6858
Peppers		28.72	25.32	0.8315	0.7253

(a) (b) (c)

Fig. 2.9: (a) Noisy image with $\sigma_n = 10$ and results for K-SVD based denoising (b) by OMP and (c) by proposed method.

(a) (b) (c)

Fig. 2.10: (a) Noisy image with $\sigma_n = 20$ and results for K-SVD based denoising (b) by OMP and (c) by proposed method.

(a)

(b)

(c)

(d)

Fig. 2.11: (a) Original image. (b) Noisy image with $\sigma_n = 5$ and results for K-SVD based denoising (c) by OMP and (d) by proposed method.

(a)

(b)

(c)

Fig. 2.12: (a) Noisy image with $\sigma_n = 10$ and results for K-SVD based denoising (b) by OMP and (c) by proposed method.

(a)

(b)

(c)

Fig. 2.13: (a) Noisy image with $\sigma_n = 15$ and results for K-SVD based denoising (b) by OMP and (c) by proposed method.

2.6 Conclusion

In this chapter, we examined three greedy algorithms- the OMP, the StOMP, and the BPA for image denoising and proposed a modified version of the BPA. The main idea behind this algorithm is that we can improve the performance of the BPA by a sparse initialization and redefining the stopping condition of the SBPA. The simulation study shows the advantage of the proposed modification in terms of representation error and reconstruction error over other selected greedy pursuit algorithms especially at lower levels of noise. We have applied the proposed algorithm for the removal of additive white Gaussian noise from gray scale images by integrating the proposed algorithm and the K-SVD dictionary learning algorithm in a sparse representation framework. The denoising results demonstrate that the proposed framework outperforms the K-SVD based denoising algorithm using the OMP at low noise levels, but at higher noise levels, the OMP based sparse denoising performs better.

Chapter 3

Removal of Impulse Noise Using Sparse Representation

3.1 Introduction

A photographic image is often corrupted by impulse noise during image acquisition or transmission [102]. Impulse noise may also be caused by variety of sources, such as switching, industrial machines in the vicinity of the receiver, power-line interference, lightning in the atmosphere, man-made noise, etc. Therefore, filtering is essential to minimize the effect of image degradation due to this noise.

Linear filtering techniques are extensively used in the field of image restoration. They are very popular because of the mathematical simplicity, backed by the linear system theory and computational efficiency. In spite of these, not all denoising problems can be satisfactorily addressed through the use of linear filters. Particularly, linear filters perform poorly in the case of impulse noise. They tend to blur edges and destroy lines, and other fine image details. These reasons have led to the use of nonlinear filtering techniques. A class of nonlinear filters that has been proven very useful is the class of median based filters. The median filter [103] takes the median of the data inside a moving window of pre-determined length as the filter output. The median filter is suitable for long-tailed noise distributions (e.g. Laplacian distribution) and performs poorly for short-tailed noise distributions (e.g. uniform distribution) [23]. It effectively reduces the impulse noise, which takes very high and very low values. The drawback of the median filter is the blurring caused to the image. One way to improve this situation is the weighted median (WM) filter [24,35,104], which gives more weight to some values within the window than others. A special case of the WM filter is the center-weighted median (CWM) filter [25] which gives more weight only to the central value of the window. The main limitation of these filters is that they try to change the pixels that are not corrupted by the

noise as they are typically applied uniformly across the entire image. As a result, their effectiveness in noise suppression is often at the expense of blurred and distorted image features. A solution to this situation is to include a decision making process to these filters to locate the pixels corrupted by the noise. At each pixel location, it is first determined whether the current pixel is contaminated. Filtering is applied on the pixel if it is corrupted by noise. The corrupted pixels are replaced by the median values, while the noise-free pixels are left unaltered. Since not every pixel is filtered, undue distortion can be avoided. However, the performance of this type of filters depends mainly on its ability to detect the noisy pixels.

A simple but effective impulse detection filter is the rank-conditioned median (RCM) filter [26] in which the pixels in the filtering window are ranked according to their magnitudes and the center pixel is considered to be noisy if it lies outside the trimming rank. In the signal-dependent rank order mean (SD-ROM) filter [27] all but the central pixel within the filtering window are considered for rank-ordering. The SD-ROM filter works well for both the fixed-valued and the random-valued impulse noise. In [105], the authors proposed a progressive switching median (PSM) filter where both the impulse detector and the noise filter are applied progressively in iterative manners. Chen and Wu [28] proposed an adaptive scheme for impulse noise detection by thresholding the absolute differences for different center weights. There are many decision based median filers which have been developed recently including the directional weighted median (DWM) filter [106] and the contrast enhancement-based filter (CEF) [107]. The main drawback of these filters is that the replacement of the noisy pixels by the rank-ordered mean or the median results in the blurring of details and edges, especially when the noise ratio is high. To avoid the median operation for filtering, the authors in [108] proposed an iterative two-stage filter for the removal of random-valued impulse noise. First, it uses a modified ACWM (MACWM) filter to detect the noisy pixels and in the second stage a detail preserving regularization procedure is applied to preserve the edges and other details at high-noise ratio.

Sparse representation has been successfully exploited for the removal of the additive white Gaussian noise with very good performance [56]. The assumption here is that the natural signals are sparse or compressible in the sense that they have a concise representations when expressed with a proper basis set [69]. Recently sparse representation has also been used for the restoration of colour images [79]. The work in [79] also used sparse representation to handle non-homogeneous noise and showed applications to colour image *inpainting* and *demosaicing* problems.

In this chapter, a novel two-stage *Sparse Reconstruction Filter* (SRF) is proposed for the removal

of impulse noise from an image using an iterative procedure. In the first stage, we consider a simple impulse noise detection scheme to detect the noisy pixels. In the second stage, the noisy pixels are reconstructed iteratively by using a sparse reconstruction technique until convergence.

In parallel to this work, the authors in [109] also proposed a sparse representation based impulse noise removal algorithm. The algorithm consists of two stages. In the first stage, the impulses are detected by the boundary discriminative noise detection (BDND) [110]. In the second stage, the noisy pixels are reconstructed iteratively by solving a sparse representation based optimization problem.

3.2 Impulse Noise Detection

Consider a square grid $\mathbf{P}$ of dimension $\sqrt{m} \times \sqrt{m}$ over which an 8-bit gray scale image $\mathbf{x}$ is defined. Let $y(s,t)$ be the gray value of the noisy image $\mathbf{y}$ at pixel $(s,t) \in \mathbf{P}$ and $W(s,t)$ be a window centered at (s,t). We assume here the following impulse noise model

$$y(s,t) = \begin{cases} x(s,t), & \text{with probability } 1-r \\ d(s,t), & \text{with probability } r \end{cases}, \tag{3.1}$$

where $x(s,t)$ and $d(s,t)$ denote the pixel values at location (s,t) in the original image and the noisy image respectively and r is the noise ratio. In an 8-bit image, the fixed-valued (salt and pepper) impulse noise values $d(s,t)$ can take either 0 or 255 whereas for the random-valued impulse noise, $d(s,t)$ is uniformly distributed in [0, 255].

In the proposed algorithm, we consider a unified approach for the detection of impulse noise meaning that our algorithm can be combined with any of the existing impulse noise detection schemes and yet we show that the performance of the proposed scheme remains superior compared to the traditional median based filters. The performance of the proposed algorithm can be analyzed by the recently developed theory of *compressed sensing* or *compressive sampling* [74, 85]. According to the compressed sensing theory, it is possible to reconstruct a signal sampled at a rate much lower than the Nyquist rate accurately, provided it has a sparse representation with respect to a certain basis set.

3.3 Sparse Denoising

Consider the image $\mathbf{x}$ be arranged into a column vector of size m and its noisy version $\mathbf{y}$ being corrupted by the additive white Gaussian noise (AWGN). In the sparse representation framework, the signal $\mathbf{x} \in \mathbb{R}^m$ can be represented as a linear combination of a few columns (called the *atoms*) from an overcomplete dictionary $\mathbf{\Phi} \in \mathbb{R}^{m \times K}$ where $m \ll K$. Therefore, using the model in Equation (2.3),

$$\mathbf{y} = \mathbf{\Phi}\boldsymbol{\alpha} + \mathbf{n}, \tag{3.2}$$

where $\boldsymbol{\alpha} \in \mathbb{R}^K$ is the sparse coefficient vector and $\mathbf{n}$ is the additive white noise with variance σ_n^2. The above problem does not have a unique solution for $\boldsymbol{\alpha}$. As discussed earlier, the *noise-aware* variant of the sparsest representation problem is given by

$$\begin{aligned} &\min_{\alpha} \ \|\alpha\|_0 \\ &\text{subject to } \|\mathbf{y} - \mathbf{\Phi}\alpha\|_2 \leqslant \varepsilon, \end{aligned} \tag{3.3}$$

where $\|.\|_0$ is the ℓ^0-norm, counting the number of nonzeros in a vector and ε is a threshold depending on the RMSE of representation and the noise standard deviation σ_n. The sparse denoising problem involves solving the optimization problem in Equation (3.3).

3.4 K-SVD Based Image Denoising

Chapter 2 discussed the image denoising method using the sparse representation over a learned overcomplete dictionary obtained by applying the K-SVD on overlapping patches of the image. It is assumed that the image $\mathbf{x}$ has sparse representation in each patch of dimension $\sqrt{m_p} \times \sqrt{m_p}$. Addressing the denoising problem as a sparse decomposition problem in each patch leads to the energy minimization problem which is reproduced here for conveneience:

$$\begin{aligned} \left\{\hat{\boldsymbol{\alpha}}_i, \hat{\mathbf{\Phi}}, \hat{\mathbf{x}}\right\}_{i=1,2,\ldots,M} = \arg \min_{\mathbf{\Phi}, \boldsymbol{\alpha}_i, \mathbf{x}} \Big\{ \gamma \|\mathbf{x} - \mathbf{y}\|_2^2 \\ + \sum_{i \in \mathbf{P}} \lambda_i \|\boldsymbol{\alpha}_i\|_0 + \sum_{i \in \mathbf{P}} \|\mathbf{\Phi}\boldsymbol{\alpha}_i - \mathbf{L}_i\mathbf{x}\|_2^2 \Big\}, \end{aligned} \tag{3.4}$$

where i marks the location of the patch in the image and γ is a penalty parameter related to the noise variance and λ is the sparsity inducing regularization term. $\hat{\boldsymbol{\alpha}}_i$ are the sparse representation for the i^{th} patch using $\hat{\mathbf{\Phi}}$. The operator $\mathbf{L}_i$ is a binary matrix $m_p \times m$ which extracts the $\sqrt{m_p} \times \sqrt{m_p}$ patch from the i^{th} location in the image. The above problem is solved in two stages:

1. *Sparse coding stage*

   It is assumed that $\mathbf{\Phi}$ is known and the minimization problem in Equation (3.4) consists of only two unknowns, namely, $\boldsymbol{\alpha}$ and $\mathbf{x}$. Then with the initialization $\mathbf{x} = \mathbf{y}$, the problem can be decoupled into many smaller problems of the form

$$\hat{\boldsymbol{\alpha}}_i = \arg\min_{\boldsymbol{\alpha}_i} \left\{ \lambda_i \|\boldsymbol{\alpha}_i\|_0 + \|\mathbf{\Phi}\boldsymbol{\alpha}_i - \mathbf{L}_i\mathbf{x}\|_2^2 \right\}. \tag{3.5}$$

   The above optimization problem is solved by the greedy orthogonal matching pursuit algorithm.

2. *Dictionary update stage*

   After finding all $\hat{\boldsymbol{\alpha}}_i$ as above, the dictionary is updated one column at a time using the algorithm discussed in Chapter 2.

The above two stages are carried out iteratively till the convergence of the results. After getting all $\hat{\boldsymbol{\alpha}}_i$ (corresponding to all the patches in the image) and the $\hat{\mathbf{\Phi}}$ as above, the problem in Equation (3.4) becomes

$$\hat{\mathbf{x}} = \arg\min_{\mathbf{x}} \gamma \|\mathbf{x} - \mathbf{y}\|_2^2 + \sum_i \left\| \mathbf{L}_i\mathbf{x} - \hat{\mathbf{\Phi}}\hat{\boldsymbol{\alpha}}_i \right\|_2^2. \tag{3.6}$$

The above is a quadratic optimization problem has the closed-form solution given by

$$\hat{\mathbf{x}} = \left[\gamma\mathbf{I} + \sum_i \mathbf{L}_i^T\mathbf{L}_i \right]^{-1} \left[\gamma\mathbf{y} + \sum_i \mathbf{L}_i^T\hat{\mathbf{\Phi}}\hat{\alpha}_i \right], \tag{3.7}$$

where $\mathbf{I}$ is the identity matrix.

The K-SVD based image denoising is shown to have the state-of-the-art performance for the removal of additive white Gaussian noise [56].

3.5 Sparse Recovery by Compressed Sensing

Compressed sensing (CS) theory [74] states that a signal which is sparse over an appropriate basis such as the DCT, the wavelets, or the overcomplete dictionary can be exactly recovered from a small number of linear measurements. The minimum number of such measurements is considerably lower than the number of samples required by the Shannon-Nyquist sampling theorem. The accurate reconstruction of missing data can be directly linked to the theory of data reconstruction via compressed sensing. Although the CS theory was originally developed for classes of signals that have a very sparse representation in an orthonormal basis, the authors in [111] have shown its extension for signals having sparse representations in overcomplete dictionaries.

Consider a signal $\mathbf{x}$ which is sparse with respect to an overcomplete basis $\mathbf{\Phi}$ so that $\mathbf{x} = \mathbf{\Phi}\boldsymbol{\alpha}$. Let $\mathbf{\Psi} = [\boldsymbol{\psi}_1\ \boldsymbol{\psi}_2\ \ldots\ \boldsymbol{\psi}_N]^T$ be an $N \times m$ sampling matrix, with $N \ll m$. Let $\mathbf{s}$ be the vector of N linear measurements of the sparse signal $\mathbf{x}$ obtained by using the matrix $\mathbf{\Psi}$ such that $\mathbf{s} = \mathbf{\Psi}\mathbf{x}$. For recovery of $\mathbf{x}$ from $\mathbf{s}$, CS requires that $\mathbf{\Psi}$ and $\mathbf{\Phi}$ to be as incoherent (orthogonal) as possible [74,85]. The recovery of $\mathbf{x}$ from $\mathbf{s}$ can be done by the following ℓ^0-norm minimization problem:

$$\begin{aligned} \hat{\boldsymbol{\alpha}} &= \min_{\boldsymbol{\alpha}} \|\boldsymbol{\alpha}\|_0 \\ &\text{subject to } \mathbf{s} = \mathbf{\Psi}\mathbf{\Phi}\boldsymbol{\alpha},\ \ \mathbf{x} = \mathbf{\Phi}\boldsymbol{\alpha}. \end{aligned} \tag{3.8}$$

In general, signals of interest may not be exactly sparse and some measurement noise may also be added due to the finite precision of the measuring devices. Therefore, a *noise-aware* variant of problem in Equation (3.8) is given by

$$\begin{aligned} \hat{\boldsymbol{\alpha}} &= \min_{\boldsymbol{\alpha}} \|\boldsymbol{\alpha}\|_0 \\ &\text{subject to } \|\mathbf{s} - \mathbf{\Psi}\mathbf{\Phi}\boldsymbol{\alpha}\|_2 \leqslant \varepsilon, \end{aligned} \tag{3.9}$$

where $\varepsilon > 0$ accounts for the noise in the linear measurements and of non-exact sparsity.

Assuming that $\mathbf{\Phi}$ is learned from a set of overlapping patches of an image using the K-SVD algorithm, the problem in the above equation is first decoupled into many smaller problems given by

$$\begin{aligned} \hat{\boldsymbol{\alpha}}_i &= \min_{\boldsymbol{\alpha}_i} \|\boldsymbol{\alpha}_i\|_0 \\ &\text{subject to } \|\mathbf{L}_i\mathbf{s} - \mathbf{\Psi}\mathbf{\Phi}\boldsymbol{\alpha}_i\|_2 \leqslant \varepsilon, \end{aligned} \tag{3.10}$$

where ε accounts for the noise and the RMSE of representation in the i^{th} patch. Following [56], we consider these to be the sparse representation problems over the image patches which can be solved using the OMP and the given $\mathbf{\Phi}$. After getting $\hat{\boldsymbol{\alpha}}_i$ corresponding to all the patches, the image $\mathbf{x}$ can be obtained by the weighted averaging operation given by

$$\hat{\mathbf{x}} = \left(\sum_i \mathbf{L}_i^T\mathbf{L}_i\right)^{-1}\left(\sum_i \mathbf{L}_i^T\mathbf{\Phi}\hat{\boldsymbol{\alpha}}_i\right), \tag{3.11}$$

where the matrix to be inverted is a diagonal one, representing the number of times each pixel is overlapped.

3.5.1 Mutual Coherence of the Combined Dictionary

For accurate reconstruction of the data via CS requires $\mathbf{\Phi}$ and $\mathbf{\Psi}$ to be mutually incoherent [74]. The mutual coherence between $\mathbf{\Phi}$ and $\mathbf{\Psi}$ is related to the correlation between the atoms of $\mathbf{\Phi}$ and $\mathbf{\Psi}$. However, Elad [112] proposed an optimal reconstruction condition on the basis of the mutual incoherence between the atoms of the equivalent dictionary.

Consider the equivalent dictionary $\mathbf{D} = \mathbf{\Psi\Phi}$, where $\mathbf{D} = [\mathbf{d}_1\ \mathbf{d}_2\ \ldots\ \mathbf{d}_K]$. The incoherence between $\mathbf{\Psi}$ and $\mathbf{\Phi}$ is measured by the *mutual coherence* $\mu(\mathbf{D})$ of the equivalent dictionary $\mathbf{D}$. As introduced in Chapter 2, it is given by

$$\mu(\mathbf{D}) = \max_{i\neq j, i\geqslant 1, j\leqslant K} \frac{\left|\mathbf{d}_i^T \mathbf{d}_j\right|}{\|\mathbf{d}_i\|_{\ell_2} \|\mathbf{d}_j\|_{\ell_2}}. \tag{3.12}$$

If the sensing matrix $\mathbf{\Psi}$ is obtained in such a way that $\mu(\mathbf{D})$ is very small considering $\mathbf{\Phi}$ being fixed, the successful recovery of the original signal $\mathbf{x}$ is possible from the linear measurements $\mathbf{s}$. The details of the theory behind signal recovery through CS may be found in [74, 85, 111].

3.6 Impulse Noise Filtering Using Compressed Sensing Principle

In the detection based filtering algorithms, the detected noisy pixels are reconstructed from the noise-free pixels in the image. These noise-free pixels can be considered as the measured data in the CS paradigm.

Suppose the impulse-detected image $\mathbf{z}$ is given by $\mathbf{z} = [z_1\ z_2\ \ldots\ z_m]^T$ where

$$z_i = \begin{cases} x_i, & \text{if } x_i \text{ is noise-free} \\ 0, & \text{otherwise} \end{cases}, \tag{3.13}$$

and N indicates the number of noise-free pixels. These noise-free pixels can be arranged into a vector $\mathbf{s}$ such that

$$\mathbf{s} = \mathbf{\Psi z}, \tag{3.14}$$

where $\mathbf{\Psi}$ is a $N \times m$ binary matrix with

$$\Psi_{ij} = \begin{cases} 1, & \text{if } z_j \text{ is the } i^{\text{th}} \text{ nonzero component of } \mathbf{z} \\ 0, & \text{otherwise.} \end{cases} \tag{3.15}$$

Thus, each row of $\mathbf{\Psi}$ consists of all zeros except one element which is equal to one. As the elements of a row other than the unity element are all zeros, $\mathbf{D} = \mathbf{\Psi\Phi}$ consists of the partial rows of the matrix $\mathbf{\Phi}$.

To measure the incoherence of $\mathbf{\Psi}$ and $\mathbf{\Phi}$, a number of overcomplete dictionaries of dfferent sizes are learned by applying the K-SVD algorithm on the "Lena" image. For each $\mathbf{\Phi}$, a number of rows are randomly dropped to get the dictionary $\mathbf{D}$ of size $N \times K$. For different values of N, the entries of $\mathbf{D}$ are considered to determine $\mu(\mathbf{D})$ according to Equation (3.12). Fig. 3.1 shows the plot of $\mu(\mathbf{D})$ for different N on three overcomplete dictionaries of size 64×256, 100×256 and

144×256, respectively. From the figure it is clearly observed that mutual coherence values decreases

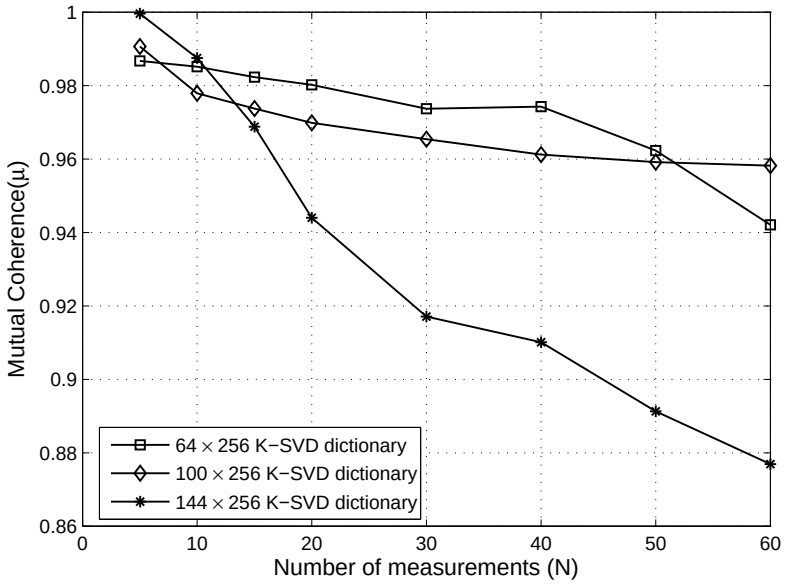

Fig. 3.1: Comparison of mutual coherence values at different values of available measurements using different learned overcomplete dictionaries

as the number of measurements increases for any given dictionary. Therefore, the reconstruction performance will expectedly depend on the number of noise-free data. The following conclusions are drawn from the above study:

1. The selection of $\mathbf{\Psi}$ by the present method is a simple method. But it cannot guarantee incoherence of $\mathbf{\Psi}$ with $\mathbf{\Phi}$.

2. As a general case, decreasing N results in increased coherence.

3. Unlike what reported in [82], the coherence does not increase sharply to 1 as N is reduced beyond a limit.

4. With the increasing dictionary redundancy, defined as the ratio of the number of columns to its rows, the coherence between $\mathbf{\Psi}$ and $\mathbf{\Phi}$ increases.

   As reported in [56], decreasing the redudancy of the dictionary $\mathbf{\Phi}$ results in decreased denoising performance in addition to increased computational overhead in learning the dictionary and OMP iterations. Therefore, as recommended in [56], we adopt a 64×256 dictionary.

3.7 Proposed Sparse Reconstruction Filter

A novel two-stage *sparse reconstruction filter* (SRF) is proposed for the removal of impulse noise based on the above study. Fig. 3.2 shows the block diagram of the proposed filter. In the first stage, an impulse noise detection algorithm is used to identify the pixels which are likely to be corrupted by the noise. The impulse noise detected image $\mathbf{z}$ is obtained by replacing the noisy pixels by zeros. The noise-free pixels in $\mathbf{z}$ are arranged into a column vector $\mathbf{s}$ and are considered as the samples from which the image is to be reconstructed. The matrix $\mathbf{\Psi}$ is constructed using Equation (3.15). In the second stage, we obtain a global dictionary $\hat{\mathbf{\Phi}}$ learned over a large data set of clean images

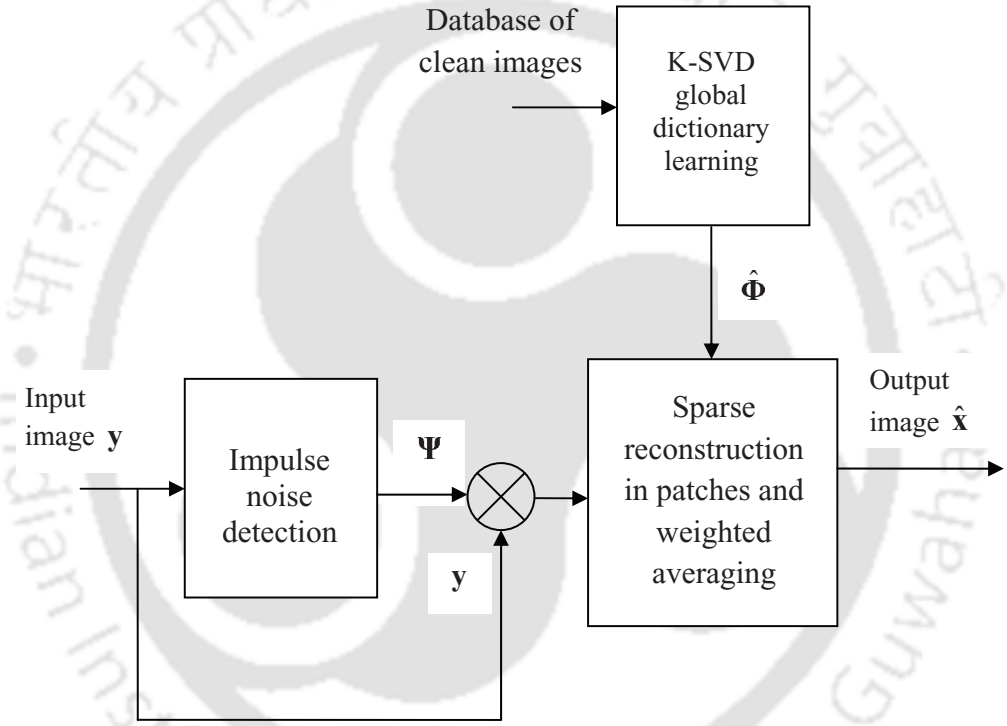

Fig. 3.2: Block diagram of the sparse reconstruction filter

which are not related to the test images. The overlapping patches of the image are considered and the image in each patch is reconstructed from the samples of $\mathbf{s}$ in the patch. The direct application of the OMP requires a large number of iterations for a small ε value in Equation (3.10). This is evidenced by our experimental results reported in Section 3.8. For faster convergence, the following strategy is applied:

3.7.1 Changing Constraint for OMP Iterations

Set ε at a large value ε^0 depending on the percentage of noise. In practice ε^0 can be set depending on the % of pixels detected as impulse. We apply the OMP to estimate $\hat{\boldsymbol{\alpha}}_i$ by solving the minimization problem in Equation (3.10) on the overlapping patches of the image $\mathbf{s}$. Then $\hat{\mathbf{x}}_i$ are obtained by using $\hat{\mathbf{x}}_i = \hat{\boldsymbol{\Phi}}\hat{\boldsymbol{\alpha}}_i$ for the image patches at locations $i = 1, 2, \ldots, M$ in the image plane $\mathbf{P}$. We call this stage as the sparse reconstruction stage in our algorithm. The $\hat{\mathbf{x}}_i$ obtained above are then substituted in Equation (3.5) and solve for the new estimates of $\hat{\boldsymbol{\alpha}}_i$ using the OMP with a reduced ε. Since the reconstructed samples replace the original samples after each iteration, the constraint ε on the ℓ^2-norm of reconstruction error is changed after each iteration. The strategy is described by

$$\varepsilon_{j+1} = \nu\varepsilon_j, \tag{3.16}$$

where j denotes an OMP iteration and ν is a parameter close to unity. The above step is carried out recursively. The algorithm stops when ε_{j+1} reaches a minimum value ε^* determined by experimentally. The overall algorithm can be summarized as follows:

Algorithm 4 Sparse Reconstruction Filter

1: Input $\mathbf{y}$.
2: Detect the noisy pixels using an impulse noise detection algorithm and obtain $\mathbf{z}$ using Equation (3.13).
3: Obtain $\boldsymbol{\Psi}$ and $\mathbf{s}$.
4: Learn a global dictionary $\hat{\boldsymbol{\Phi}}$ by applying the K-SVD algorithm on a clean image data set.
5: Reconstruct $\mathbf{x}_i$ for the overlapping image patches at $i = 1, 2, \ldots, M$, by the following steps:
   a. Set $\varepsilon = \varepsilon^0$.
   b. Obtain $\mathbf{s}_i = \mathbf{L}_i\mathbf{s}$.
   c. Substitute $\mathbf{s}_i$ corresponding to the i^{th} patch in Equation (3.10) to estimate $\boldsymbol{\alpha}_i^0$ for $\mathbf{L}_i\mathbf{s}$ by using the OMP.
   d. Obtain $\mathbf{x}_i = \hat{\boldsymbol{\Phi}}\boldsymbol{\alpha}_i^0$.
   e. **repeat**
   f. Obtain $\varepsilon = \nu\varepsilon$ where ν is less than unity.
   g. Substitute $\mathbf{x}_i$ for $\mathbf{L}_i\mathbf{x}$ to estimate $\boldsymbol{\alpha}_i$ in Equation (3.5) by using the OMP.
   h. Obtain $\mathbf{x}_i = \hat{\boldsymbol{\Phi}}\boldsymbol{\alpha}_i$.
   i. **until** $\varepsilon = \varepsilon^*$.
6: Obtain $\hat{\mathbf{x}}$ by weighted averaging using Equation (3.11).

3.8 Experimental Results

A number of experiments are carried out to evaluate the performance of the proposed algorithm on standard test images of "Lena", "Barbara", "Boat", and "Peppers". The first three images are of size 512×512 and the last one is of size 256×256. All these images are artificially corrupted with the random-valued and the fixed-valued impulse noises at noise ratios varying from 20% to 90%. The denoising performance is measured in terms of the PSNR values defined in the previous chapter. The structural similarity index (SSIM) is not used here as the PSNR is the most commonly used parameter for comparison of the performances of impulse denoising methods.

The detection stages of three state-of-the-art impulse noise filtering algorithms are considered for the detection of the impulse noise. They are: (1) the SD-ROM filter (2) the ACWM filter and (3) the contrast enhancement filter. The details of these filters are given in Appendix A.

We obtain a global dictionary by applying the K-SVD algorithm as discussed in [56] on a large data set (100000 patches, each of size 8×8) of clean and standard test images. A few sample images of this data set are "couple", "house", "cameraman", "goldhill", "clock", "aerial", and "bridge". All these images are taken from the University of Southern California image database at [1]. The 8×8 patch is a good choice for a learned dictionary with $K = 256$ in terms of the denoising performance and the computational overhead as discussed in Section 3.6. The experimental results are reported below:

A. Effect of the impulse noise detection method

The impulse detection methods are applied on test images corrupted by fixed-valued and random-valued impulses. The denoising method is applied on these impulse detected images. Tables 3.1-3.4 show the performance of the proposed sparse reconstruction filter in terms of the PSNR values. The following observations are made:

1. For the same level of corruption by the fixed-valued impulse noise, the SD-ROM detection gives best PSNR performances compared to the other two methods. However, for random valued impulse noise, the ACWM detection leads to the best PSNR performances. The PSNR performance for the images corrupted by random-valued impulse noise is better than that for the corruption by fixed-valued impulse noise.

2. The experiments are also repeated assuming the ideal detection of the impulse noise. The

[1] http://sipi.usc.edu/database/

denoising performance of the proposed method is very good for ideal detection of the impulse noise. The PSNR performance for the corruptions by the fixed-valued and the random-valued impulse noise are similar for ideal detection.

Figs. 3.3-3.4 show the denoised outputs of the proposed filter on "Boat" image corrupted by 50% fixed-valued and random-valued impulse noise for different impulse noise detection methods. Thus the denoising performance of the proposed filter depends on the accuracy of impulse detection. But the variability of the filtering performance for different detection methods under study is not much.

Table. 3.1: Comparison of PSNR (dB) for the filtered "Barbara" image using the prposed filter

Impulse detection method	Random-valued impulse			Fixed-valued impulse		
	30%	40%	50%	30%	40%	50%
SD-ROM [27]	24.91	24.19	23.32	25.06	24.13	22.95
ACWM [28]	25.35	24.23	23.34	24.71	23.55	21.44
CEF [107]	24.81	23.53	22.00	24.80	23.48	19.40
Ideal detection	35.67	33.58	31.80	35.65	33.66	31.62

Table. 3.2: Comparison of PSNR (dB) for the filtered "Peppers" image using the proposed filter

Impulse detection method	Random-valued impulse			Fixed-valued impulse		
	30%	40%	50%	30%	40%	50%
SD-ROM [27]	27.50	26.13	25.03	26.98	25.32	22.68
ACWM [28]	28.50	27.06	25.66	27.30	24.79	22.17
CEF [107]	28.06	26.21	24.99	26.38	23.90	21.88
Ideal detection	35.30	32.98	30.88	35.12	33.37	31.24

Table. 3.3: Comparison of PSNR (dB) for the filtered "Boat" image using the proposed filter

Impulse detection method	Random-valued impulse			Fixed-valued impulse		
	30%	40%	50%	30%	40%	50%
SD-ROM [27]	29.13	27.67	26.07	29.07	27.38	25.34
ACWM [28]	29.61	27.88	26.37	29.06	26.99	23.13
CEF [107]	28.87	27.13	24.84	28.94	26.16	21.27
Ideal detection	35.04	33.09	31.30	35.07	33.07	31.31

B. Performance of the proposed filter at different noise ratios

In this experiment, we study the performance of the proposed sparse reconstruction filter for both the random-valued and the fixed-valued impulse noise for noise ratios varying from 20% to 95%. The SD-ROM filter is used for the detection of the impulse noise for this experiment. Table 3.5

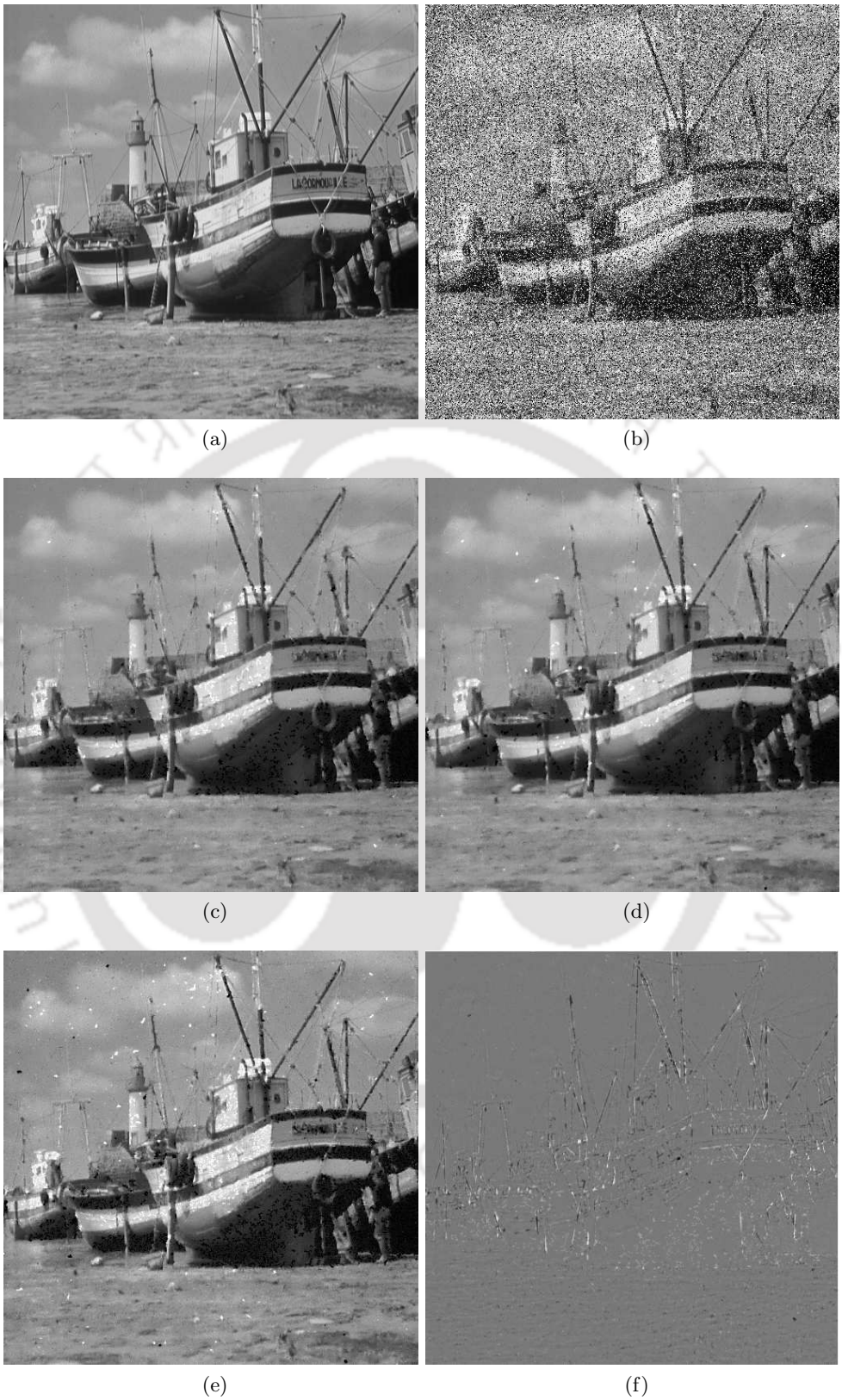

Fig. 3.3: (a) Original "Boat" image. (b) Noisy image with 50% random-valued impulse noise. Results for (c) Proposed filter with SDROM detection (d) Proposed filter with ACWM detection (e) Proposed filter with CEF detection (f) Difference between (a) and (c).

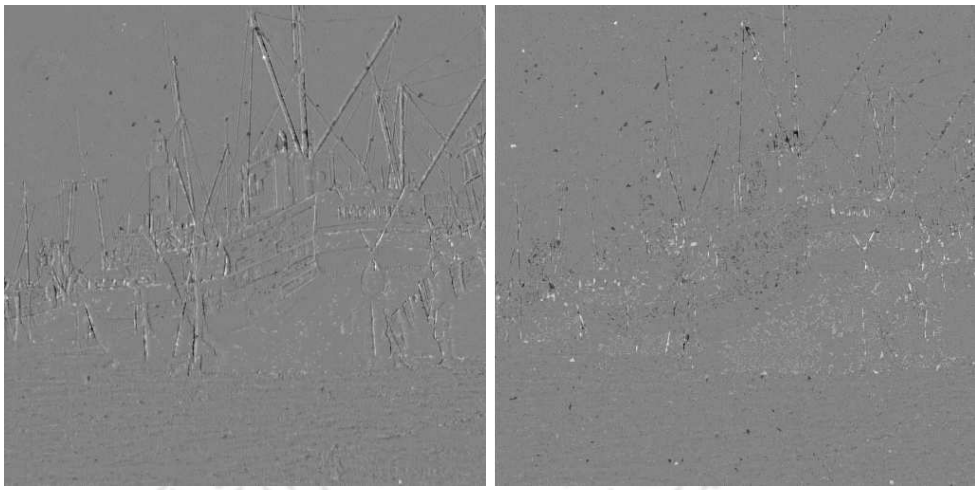

(g) (h)

Fig. 3.3: (g) Difference between (a) and (d), and (h) Difference between (a) and (e).

Table. 3.4: Comparison of PSNR (dB) for the filtered "Lena" image using proposed filter

Impulse detection method	Random-valued impulse			Fixed-valued impulse		
	30%	40%	50%	30%	40%	50%
SD-ROM [27]	33.44	31.43	29.02	33.68	31.39	28.23
ACWM [28]	33.50	31.57	29.35	32.85	30.58	25.29
CEF [107]	31.84	29.28	26.31	33.54	29.80	23.82
Ideal detection	37.69	35.89	34.23	37.70	35.79	34.18

shows the results of the proposed method on all the test images in terms of the output PSNR for different impulse noise ratio. From these results, it is observed that the proposed method works successfully for a wide range of noise ratios. However, the proposed filter is comparatively better at removing the random-valued impulse noise than the fixed-valued impulse noise particularly at noise ratios of 40% or higher. This variation is observed for other methods of impulse detection as well. It is also observed that the output PSNR values for the proposed sparse reconstruction filter decreases drastically at noise ratios of 90% or more for the random-valued impulse noise whereas for the fixed-valued impulse noise the output PSNR starts decreasing rapidly for noise ratios of 80% or more. Fig. 3.5a and Fig. 3.5b show the plots of PSNR values of the denoised outputs at different noise ratios obtained by the proposed method with the SD-ROM detection applied on two images corrupted by both the random-valued and the fixed-valued impulse noises. Figs. 3.6b-3.6f demonstrate the visual quality of the outputs obtained by the proposed denoising method using the SD-ROM detection for the "Lena" image corrupted by the random-valued impulse noise at noise ratios in the range 50%- 90%. Figs. 3.7b-3.7f show the corresponding outputs for the fixed-valued impulse noise. From these results, it is observed that the proposed filter fails to give any meaningful

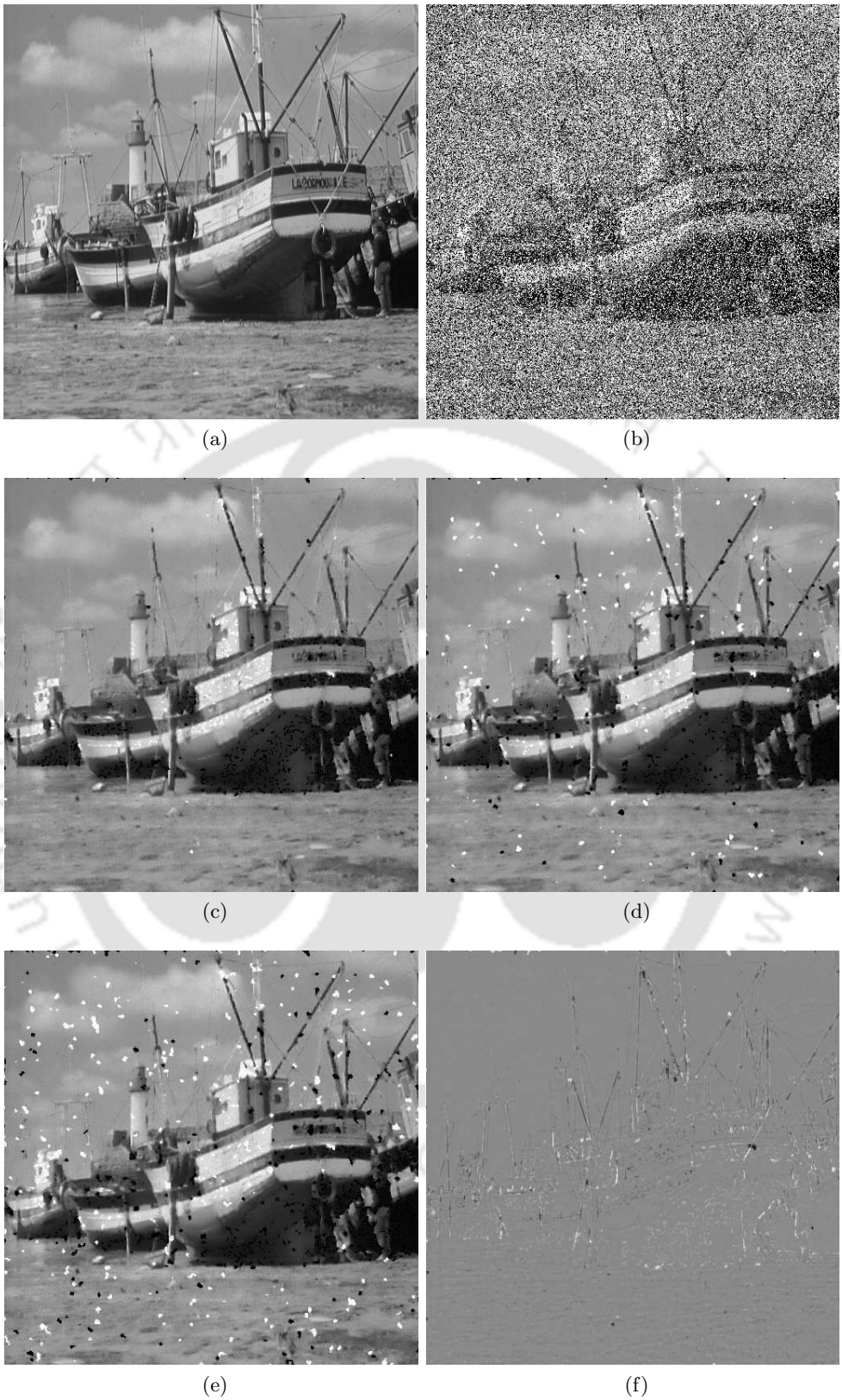

(a) (b) (c) (d) (e) (f)

Fig. 3.4: (a) Original "Boat" image. (b) Noisy image with 50% fixed-valued impulse noise. Results for (c) Proposed filter with SDROM detection (d) Proposed filter with ACWM detection (e) Proposed filter with CEF detection (f) Difference between (a) and (c).

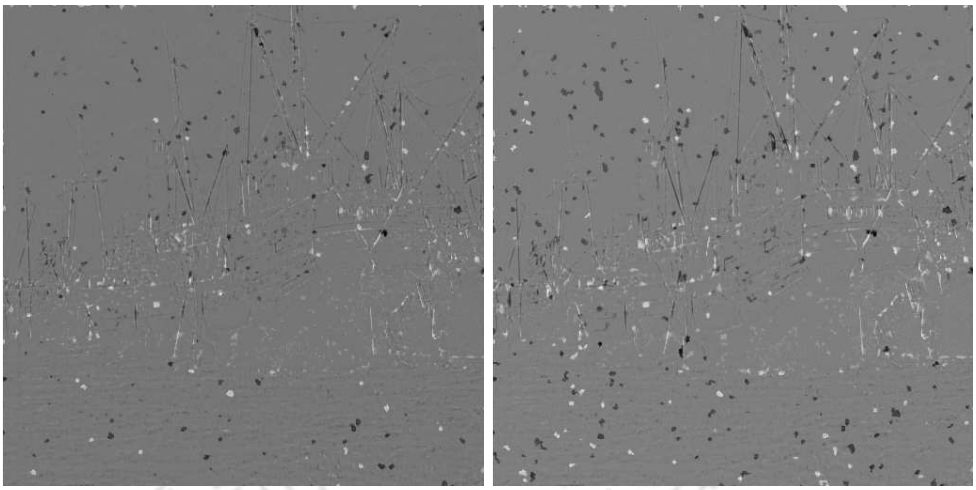

(g) (h)

Fig. 3.4: (g) Difference between (a) and (d), and (h) Difference between (a) and (e).

reconstruction for impulse noise ratios higher than 90% for the random-valued impulse noise. But it fails to reconstruct at noise ratios of 80% or higher in the case of the fixed-valued impulse noise. We have experimentally seen that the percentage of impulse detected is higher in the case of random-valued noise than the fixed-valued impulse noise at high ratios (i.e. 70% or higher). Because of this, the reconstruction performance is worse in the later case.

If noise detection is perfect, the performance of the proposed filter does not deteriorate much at high noise ratios as evident from our experiments with ideal detection up to 90% of impulse noise corruption.

C. Effect of changing constraints on the number of OMP iterations

As discussed in Section 3.7, for faster convergence we apply the OMP iteratively for decreasing values of ε. The OMP is run with different sets of ε depending upon the impulse noise ratio to refine the estimates of $\hat{\boldsymbol{\alpha}}$. Table 3.6 shows the average number of OMP iterations per patch for different test images at different noise ratios using decreasing values of ε.

The results show that the OMP takes only a few number of iterations to converge for the proposed method of changing the constraint. The results also show that there is only a slight change in the number of OMP iterations even if the noise ratio is doubled for all the test images. This is in contrast to the OMP with a fixed ε. For example, with ε fixed at the same ε^*, the OMP on the "Lena" and "Peppers" images takes much larger number of iterations as shown in Table 3.7.

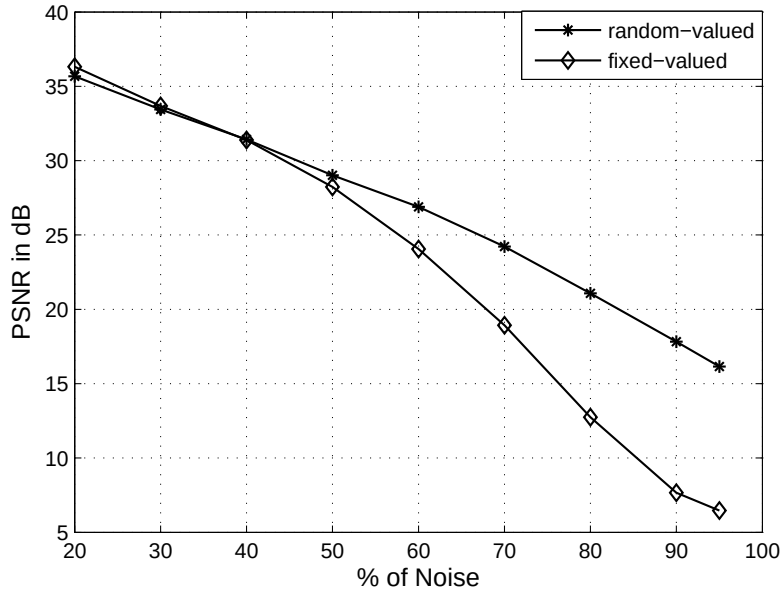

(a)

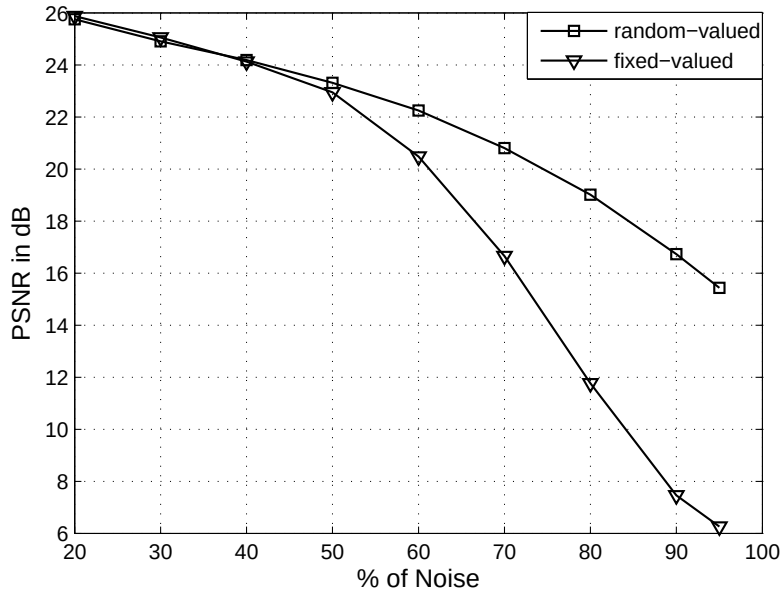

(b)

Fig. 3.5: PSNR (in dB) of the filterd outputs with the SD-ROM detection for the (a) Lena image (b) Barbara image

Table. 3.5: Comparison of PSNR (dB) for different test images using the SD-ROM detection

(a) Random-valued impulse noise

% of noise	Input PSNR	Output PSNR			
		Barbara	Peppers	Boat	Lena
20	14.84	25.76	29.60	30.53	35.67
30	13.06	24.91	27.50	29.13	33.44
40	11.80	24.19	26.13	27.67	31.43
50	10.83	23.32	25.03	26.07	29.02
60	10.01	22.25	23.20	24.70	26.89
70	9.37	20.81	21.32	22.75	24.22
80	8.78	19.02	18.92	20.49	21.07
90	8.26	16.73	16.42	17.52	17.82
95	8.00	15.44	15.10	15.83	16.15

(b) Fixed-valued impulse noise

% of noise	Input PSNR	Output PSNR			
		Barbara	Peppers	Boat	Lena
20	12.30	25.88	29.40	29.40	36.31
30	10.49	25.06	26.98	29.07	33.68
40	9.24	24.13	25.32	27.38	31.39
50	8.29	22.95	22.68	25.34	28.23
60	7.48	20.48	20.05	22.18	24.05
70	6.80	16.66	16.38	17.70	18.93
80	6.23	11.77	11.27	12.10	12.74
90	5.74	7.46	6.95	7.61	7.66
95	5.49	6.26	6.07	6.43	6.46

Table. 3.6: Comparison of the average number of OMP iterations per denoising patch for different test images. For the detection of the impulse noise the detection stage of the SD-ROM filter is used.

(a) Random-valued impulse noise

% of noise	Average number of iterations/patch			
	Barbara (512×512)	Peppers (256×256)	Boat (512×512)	Lena (512×512)
20	23	6	16	11
40	20	5	14	10

(b) Fixed-valued impulse noise

% of noise	Average number of iterations/patch			
	Barbara (512×512)	Peppers (256×256)	Boat (512×512)	Lena (512×512)
20	20	5	15	11
40	15	4	12	9

Table. 3.7: Comparison of the average number of OMP iterations per denoising patch for different test images using fixed ε. The images are corrupted by 40% random-valued impulse noise and the detection stage of the SD-ROM filter is used for impulse detection.

Image	Average number of iterations/patch
Lena (512×512)	80
Peppers(256×256)	20

(a) (b) (c) (d) (e) (f)

Fig. 3.6: (a) Original image. The output of the proposed reconstruction filter for the "Lena" image corrupted with (b) 50% (c) 60% (d) 70% (e) 80% and (f) 90% random-valued impulse noise, respectively. The detection stage of the SD-ROM filter is applied for the detection of the impulse locations.

Fig. 3.7: (a) Original image. The results of the proposed method for the "Lena" image corrupted with (b) 50% (c) 60% (d) 70% (e) 80% and (f) 90% fixed-valued impulse noise, respectively. The detection stage of the SD-ROM filter is applied for the detection of the impulse locations.

D. Comparison with the state-of-the-art impulse noise filtering methods

To evaluate the relative performance of the proposed filter, we have compared its performance with the following state-of-the-art methods: (1) the PSM filter [105] (2) the SD-ROM filter [27] (3) the modified ACWM (MACWM) filter [108] and (4) the contrast enhancement filter (CEF). For the proposed method, we consider impulse noise detection by all the three methods mentioned in subsection 3.8.

A comparison in terms of PSNR values across different denoising methods applied on the test images are shown in Tables 3.8-3.19 for both the random-valued impulse noise and the fixed-valued noises. The tables consider the performance of the proposed filter relative to the median filter and other filters under consideration. The noise levels up to 50% are considered because the median filter does not work beyond 50% of noise corruption.

The PSNR performance of the proposed filter is nearly equal to or better than that of other filters under consideration at different noise levels. The variations in performance may be due to the difference in the number of impulses detected by a particular method.

Figs. 3.8a-3.8e show the outputs of the standard median, the PSM, the SD-ROM, the MACWM, and the contrast enhancement filters on the "Boat" image corrupted by 50% fixed-valued impulse noise ratio, respectively. Figs. 3.3c-3.3e show the outputs of the proposed method with the SD-ROM filter detection, the ACWM detection and the CEF detection, respectively on the "Boat" image corrupted by 50% random-valued impulse noise. The figures clearly show that the denoised output obtained by the proposed method with the SD-ROM detection is visually the best out of all the denoised outputs.

The results also indicate that the reconstructed images obtained by the proposed method using the SD-ROM detection and the ACWM detection are almost similar. However, the reconstructed image obtained by the CEF detection shows that some noisy pixels are left undetected by this method and hence not reconstructed by the proposed method. The results are presented in Figs. 3.3f-3.3h.

Fig. 3.9 shows the results of the state-of-the-art median based filtering methods on the "Boat" image corrupted by the 50 % fixed-valued impulse noise. The results for the proposed method with the SD-ROM filter detection, the ACWM detection and the CEF detection, respectively on the "Boat" image corrupted by 50% fixed-valued impulse noise are shown in Figs. 3.4c-3.4e. It is observed that the proposed method with the SD-ROM detection performs the best in terms of visual quality. It not only removes the fixed-valued impulse noise but also preserves the detail features in the image. Fig. 3.4f shows the difference between the original image and the output obtained by

the proposed method using the SD-ROM detection. It shows that the difference contains very less features indicating the similarities between the original and the filtered images.

Fig. 3.10 shows the plots of PSNR values of the denoised image for various filtering methods and the proposed method with the SD-ROM detection on the "Lena" image corrupted by the impulse noise at different noise ratios. The results show that the proposed method outperforms the state-of-the-art detection based median filters at all noise ratios.

3.9 Conclusion

This chapter proposed a two-stage detection based novel sparse reconstruction filter for the removal of both the random-valued and the fixed-valued impulse noise from gray scale images. In the first stage, the noisy pixels are detected by an impulse noise detection method. In the second stage, the noise-free pixels are used to reconstruct the noisy pixels using the principle of sparse recovery by compressed sensing. It is shown that the performance of the proposed reconstruction depends mainly on the minimum noise-free data available for reconstruction. We have also compared the performance of the proposed method with the state-of-the-art detection based filtering schemes like the PSM, the SD-ROM, the MACWM, and the CEF. The experimental results show that with an efficient impulse detection method, the proposed reconstruction outperforms the state-of-the-art detection-based filtering methods both quantitatively and qualitatively. The study in this chapter indicates that the filtering stage of the detection-based impulse denoising methods can be replaced by a sparse reconstruction stage employing the compressed sensing principle.

Table. 3.8: Comparison of PSNR (dB) for the filtered "Barbara" image

Method	Random-valued			Fixed-valued		
	30%	40%	50%	30%	40%	50%
Median Filter [103]	23.26	21.87	20.02	20.83	17.67	14.58
PSM Filter [105]	23.85	22.51	20.75	23.44	21.50	18.92
SD-ROM Filter [27]	24.48	23.73	22.85	24.41	23.48	22.24
MACWM Filter [108]	24.76	23.61	22.01	24.21	22.85	20.76
CEF [107]	24.14	22.95	21.39	23.70	22.38	19.36
Proposed Filter with SD-ROM detection	**24.91**	**24.19**	**23.32**	**25.06**	**24.13**	**22.95**

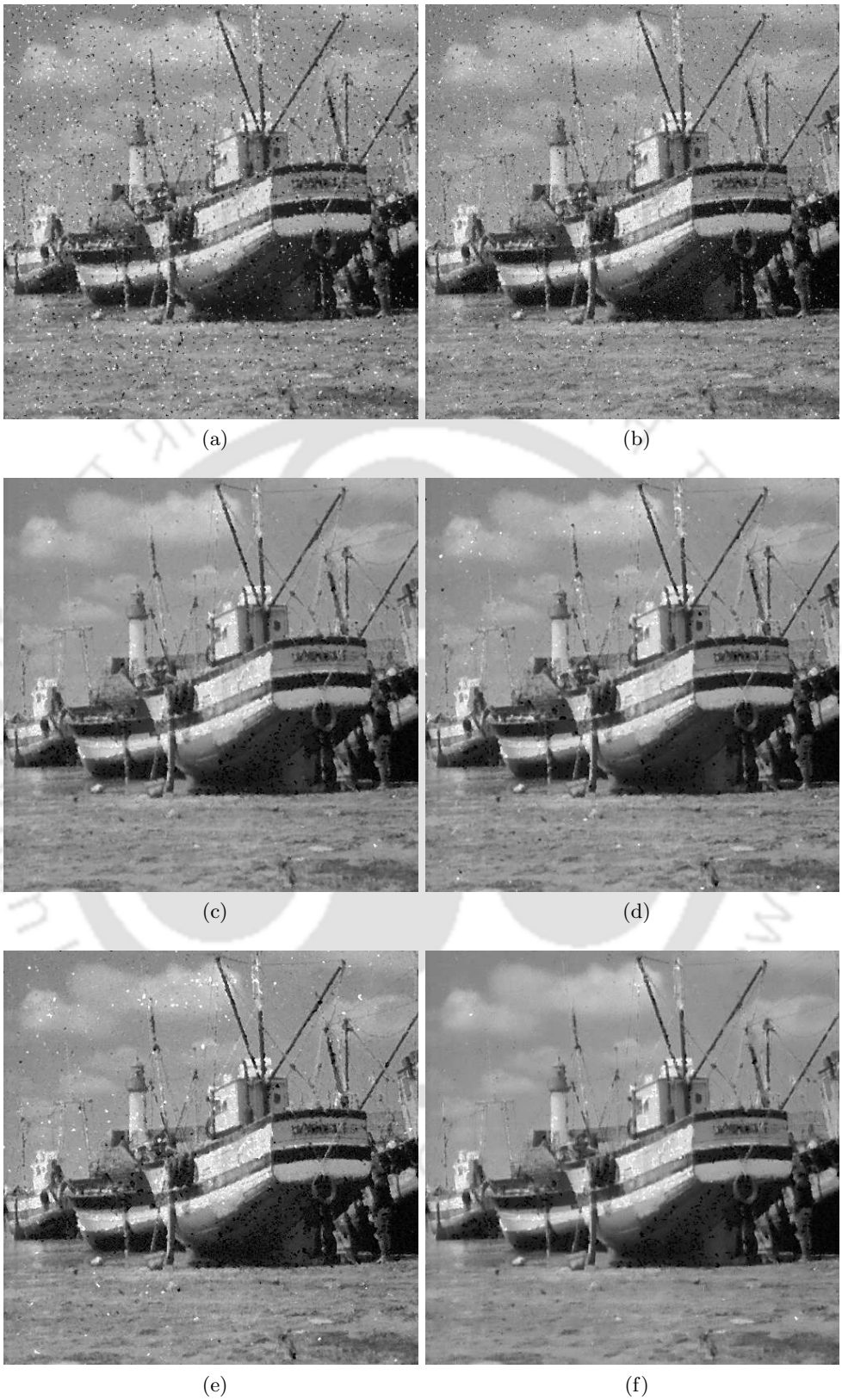

Fig. 3.8: Results of different filters for "Boat" image with 50% random-valued impulse noise. (a) Median filter. (b) PSM filter. (c) SD-ROM filter. (d) MACWM filter. (e) CEF. (f) Proposed Method.

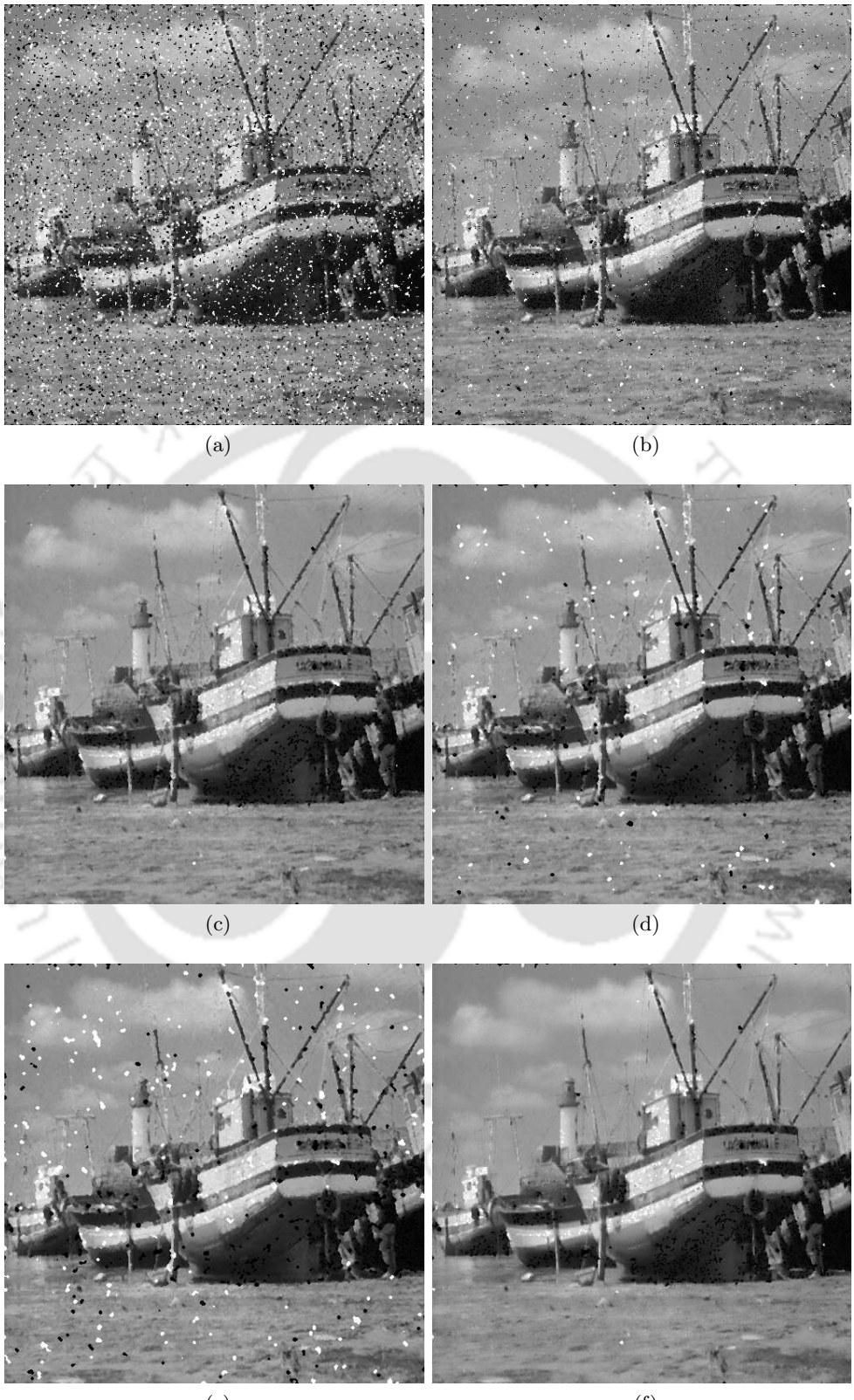

(a) (b) (c) (d) (e) (f)

Fig. 3.9: Results of different filters for "Boat" image with 50% salt and pepper noise. (a) Median filter. (b) PSM filter. (c) SD-ROM filter. (d) MACWM filter. (e) CEF. (f) Proposed Method.

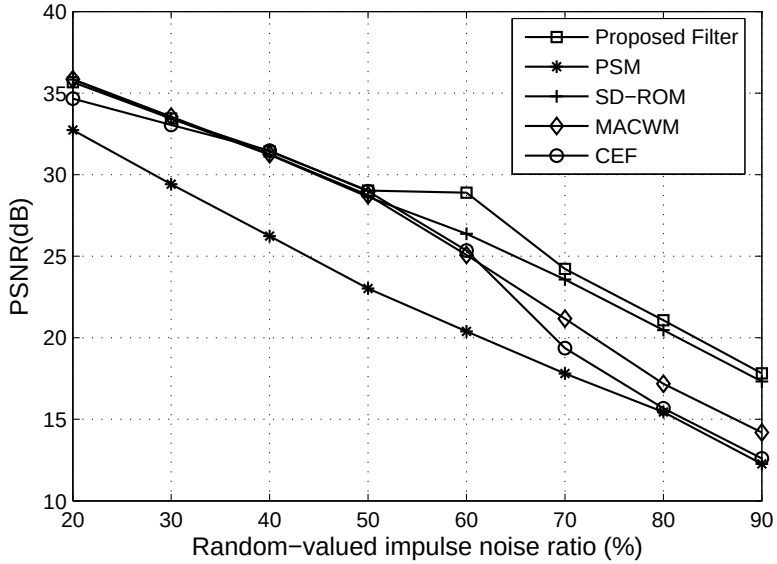

(a)

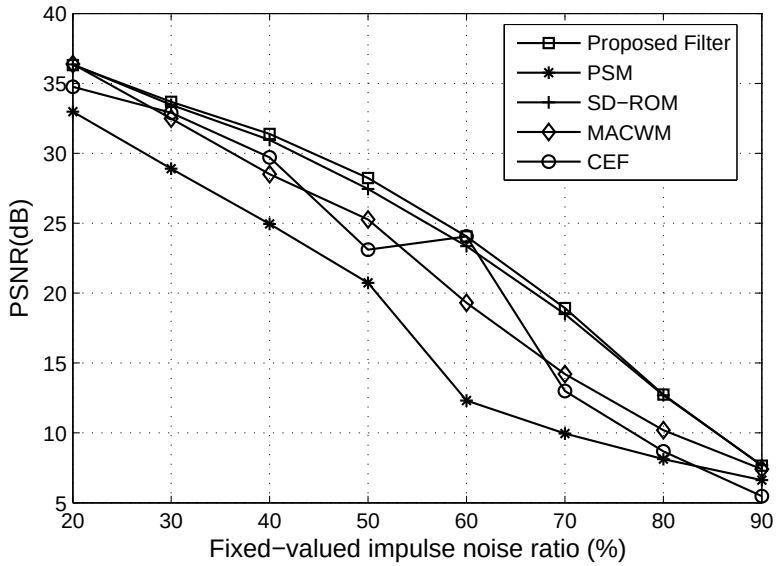

(b)

Fig. 3.10: Performance comparison of different filters for the "Lena" image corrupted by varying percentages of (a) random-valued and (b) fixed-valued impulses, respectively.

Table. 3.9: Comparison of PSNR (dB) for the filtered "Peppers" image

Method	Random-valued			Fixed-valued		
	30%	40%	50%	30%	40%	50%
Median Filter [103]	25.86	23.69	20.86	22.03	18.13	14.88
PSM Filter [105]	26.31	24.26	21.76	25.52	22.48	19.51
SD-ROM Filter [27]	26.53	25.32	23.99	25.47	24.02	21.80
MACWM Filter [108]	27.31	**26.17**	24.77	26.39	24.38	21.86
CEF [107]	26.76	25.44	21.94	25.89	23.68	20.43
Proposed Filter with SD-ROM detection	**27.50**	26.13	**25.03**	**26.98**	**25.32**	**22.68**

Table. 3.10: Comparison of PSNR (dB) for the filtered "Boat" image

Method	Random-valued			Fixed-valued		
	30%	40%	50%	30%	40%	50%
Median Filter [103]	26.28	23.98	21.33	22.61	18.52	15.06
PSM Filter [105]	27.11	24.90	22.28	26.68	23.74	20.21
SD-ROM Filter [27]	29.12	27.62	25.93	28.85	27.11	24.90
MACWM Filter [108]	**29.36**	**28.09**	25.87	28.94	26.93	22.76
CEF [107]	28.35	26.62	24.14	28.52	26.05	20.97
Proposed Filter with SD-ROM detection	29.13	27.67	**26.07**	**29.07**	**27.38**	**25.34**

Table. 3.11: Comparison of PSNR (dB) for the filtered "Lena" image

Method	Random-valued			Fixed-valued		
	30%	40%	50%	30%	40%	50%
Median Filter [103]	28.84	25.28	21.93	23.48	18.93	15.30
PSM Filter [105]	29.41	26.23	23.02	28.90	24.95	20.73
SD-ROM Filter [27]	33.44	31.22	28.63	33.47	30.96	27.45
MACWM Filter [108]	**33.56**	31.25	28.74	32.48	28.51	25.26
CEF [107]	33.05	**31.47**	28.98	32.90	29.71	23.11
Proposed Filter with SD-ROM detection	33.44	**31.47**	**29.02**	**33.68**	**31.39**	**28.23**

Table. 3.12: Comparison of PSNR (dB) for the filtered "Barbara" image

Method	Random-valued			Fixed-valued		
	30%	40%	50%	30%	40%	50%
Median Filter [103]	23.26	21.82	20.02	20.86	17.67	14.55
PSM Filter [105]	23.85	22.43	20.75	23.41	21.50	18.89
SD-ROM Filter [27]	24.48	23.70	22.85	24.39	23.48	**22.17**
MACWM Filter [108]	24.76	23.75	22.69	23.93	22.85	20.76
CEF [107]	24.14	22.91	21.39	23.74	22.04	18.70
Proposed Filter with ACWM detection	**25.35**	**24.23**	**23.34**	**24.71**	**23.55**	21.44

Table. 3.13: Comparison of PSNR (dB) for the filtered "Peppers" image

Method	Random-valued			Fixed-valued		
	30%	40%	50%	30%	40%	50%
Median Filter [103]	26.04	23.67	21.43	22.67	18.19	14.72
PSM Filter [105]	26.51	24.24	22.25	25.98	22.28	19.16
SD-ROM Filter [27]	27.06	25.55	24.14	25.75	23.40	21.88
MACWM Filter [108]	27.73	26.36	24.88	26.06	23.79	21.30
CEF [107]	27.40	25.59	24.09	25.79	23.32	20.39
Proposed Filter with ACWM detection	**28.50**	**27.06**	**25.66**	**27.30**	**24.79**	**22.17**

Table. 3.14: Comparison of PSNR (dB) for the filtered "Boat" image

Method	Random-valued			Fixed-valued		
	30%	40%	50%	30%	40%	50%
Median Filter [103]	26.55	24.04	21.28	22.61	18.52	15.06
PSM Filter [105]	27.35	24.94	22.40	26.68	23.74	20.21
SD-ROM Filter [27]	29.22	27.68	26.18	28.85	**27.11**	**24.90**
MACWM Filter [108]	**29.62**	**28.10**	26.17	28.94	26.93	22.76
CEF [107]	28.51	26.65	24.29	28.33	25.62	20.68
Proposed Filter with ACWM detection	29.61	27.88	**26.37**	**29.07**	26.99	23.13

Table. 3.15: Comparison of PSNR (dB) for the filtered "Lena" image

Method	Random-valued			Fixed-valued		
	30%	40%	50%	30%	40%	50%
Median Filter [103]	28.74	25.03	22.02	23.48	18.93	15.25
PSM Filter [105]	29.44	25.94	23.06	28.90	24.95	20.51
SD-ROM Filter [27]	33.40	31.05	28.84	**33.47**	**30.96**	**27.15**
MACWM Filter [108]	**33.64**	31.39	28.81	32.48	30.35	24.77
CEF [107]	31.28	28.63	25.68	33.23	28.77	22.84
Proposed Filter with ACWM detection	33.50	**31.57**	**29.35**	32.85	30.85	25.29

Table. 3.16: Comparison of PSNR (dB) for the filtered "Barbara" image

Method	Random-valued			Fixed-valued		
	30%	40%	50%	30%	40%	50%
Median Filter [103]	23.26	21.82	20.02	20.86	17.67	14.55
PSM Filter [105]	23.85	22.43	20.75	23.41	21.50	18.89
SD-ROM Filter [27]	24.48	23.70	22.00	24.39	22.94	**22.17**
MACWM Filter [108]	24.72	**23.75**	22.69	24.07	22.77	20.76
CEF [107]	24.14	22.91	21.39	23.74	22.04	18.70
Proposed Filter with CEF detection	**24.81**	23.53	**22.00**	**24.80**	**23.48**	19.40

Table. 3.17: Comparison of PSNR (dB) for the filtered "Peppers" image

Method	Random-valued			Fixed-valued		
	30%	40%	50%	30%	40%	50%
Median Filter [103]	26.04	23.67	21.43	21.93	18.22	14.72
PSM Filter [105]	26.51	24.24	22.25	25.24	22.83	19.16
SD-ROM Filter [27]	27.06	25.55	24.14	25.25	23.75	21.02
MACWM Filter [108]	27.67	25.89	24.88	25.50	**24.47**	21.30
CEF [107]	27.40	25.59	24.09	25.43	23.22	21.24
Proposed Filter with CEF detection	**28.06**	**26.21**	**24.99**	**26.38**	23.90	**21.88**

Table. 3.18: Comparison of PSNR (dB) for the filtered "Boat" image

Method	Random-valued			Fixed-valued		
	30%	40%	50%	30%	40%	50%
Median Filter [103]	26.55	24.04	21.28	22.61	18.52	15.06
PSM Filter [105]	27.35	24.94	22.40	26.68	23.74	20.21
SD-ROM Filter [27]	29.22	27.68	**26.18**	28.85	**27.11**	**24.90**
MACWM Filter [108]	**29.62**	**28.12**	26.17	**29.04**	26.93	22.76
CEF [107]	28.51	26.65	24.29	28.33	25.62	20.68
Proposed Filter with CEF detection	28.87	27.13	24.84	28.94	26.16	21.27

Table. 3.19: Comparison of PSNR (dB) for the filtered "Lena" image

Method	Random-valued			Fixed-valued		
	30%	40%	50%	30%	40%	50%
Median Filter [103]	28.84	25.29	22.00	23.48	18.93	15.30
PSM Filter [105]	29.41	26.13	23.12	28.90	24.95	20.73
SD-ROM Filter [27]	33.44	31.05	**28.96**	33.47	**30.96**	**27.45**
MACWM Filter [108]	**33.56**	**31.57**	28.70	32.48	30.35	25.26
CEF [107]	31.45	28.78	25.64	33.23	28.77	23.11
Proposed Filter with CEF detection	31.84	29.28	26.31	**33.54**	29.80	23.82

Chapter 4

Sparse Despeckling of Medical Ultrasound Images Using the Undecimated Wavelet Transform

4.1 Introduction

The previous chapter addressed the problem of denoising images corrupted by the impulse noise which is non-Gaussian and non-additive. This chapter considers another non-Gaussian and non-additive noise, namely, the speckle noise with the particular reference to the medical ultrasound images.

Speckle noise is an interference present in all coherent imaging systems. It arises when waves random both in amplitude and phase due to the microscopic variations of the surface roughness in a resolution cell are accumulated. It appears as a fine granular structure in the image and reduces the image quality and thereby the ability of a human observer to resolve the fine details.

In an ultrasound imaging system, high frequency ultrasound waves are projected on the areas of interest in the body. These waves pass through the skin of the patient and get reflected at the tissue interfaces. The reflected waves are envelope detected and displayed as a two-dimensional image.

Most of the biological tissues consist of scatterers much smaller in size than the acoustic wavelength; the signal acquired within a resolution cell comprises reflections from many such independent scatterers. These result in de-phased echoes causing interference (either constructive or destructive) and producing intricate interference patterns termed as speckle [44]. Speckle is a type of noise which generally masks the fine details of the ultrasound image, thereby making the interpretation of an ultrasound image difficult for medical diagnosis. As a result, despeckling methods are necessary for

enhancing the image quality and increasing the diagnostic value of medical ultrasound images. Other examples of systems affected by the speckle noise include the *synthetic aperture radar* (SAR), *optical coherence tomography* (OCT) and *sound navigation and ranging* (SONAR) images.

Goodman [3] discussed the statistical nature of the speckle for the first time in connection with laser imaging. Later on, Wagner and Smith [5] studied the statistical properties of the ultrasound speckle. The earliest despeckling method consists of a spatial compounding technique [113]. Linear filtering techniques that are widely used for the reduction of speckle include the *Lee filter* [33], the *Frost filter* [114] and the *Kuan filter* [34]. The Lee and Kuan filters produce the output image by finding a linear combination of the center pixel intensity with the average intensity within a filter window based on the local image statistics. These filters achieve a balance between a direct averaging (within the homogeneous regions) and the identity filtering (where edges and other features exist). The Frost filter also obtains a balance between averaging and all-pass filtering. In this filter an exponentially shaped filter kernel that carries out pointwise filtering operation, is used. In [29], the authors proposed a speckle reduction filter that changes the amount of smoothing according to the ratio of local mean to the local variance. The main limitation of the linear filters is that they tend to suppress the noise at the expense of over-smoothing the details. To perform filtering by preserving the anatomical content of the image, an adaptive median filter is proposed in [35]. Although this nonlinear filter is capable of suppressing speckle effectively, its low-pass characteristics seem to blur the finer image details. In [36], the authors proposed an edge sensitive diffusion based method called *speckle reducing anisotropic diffusion* (SRAD) to suppress speckle while preserving the edge information based on nonlinear partial differential equations.

Lee [33] first demonstrated that the speckle is signal dependent in the sense that the mean is proportional to the standard deviation of the speckled image. The multiplicative nature of the speckle was proposed in [7] where the noise is converted into an additive one through log transformation and the problem of despeckling is thus reduced to the estimation of signal in the presence of an additive noise. Subsequently, Wiener filtering is applied in order to reject this additive noise, followed by an exponential transformation. The structure of this algorithm is general, because it allows further modifications by replacing the linear Wiener filter by other filtering schemes.

After the pioneering work of Donoho and Johnstone [12], denoising based on wavelet decomposition has become popular for removing the additive white Gaussian noise (AWGN) from noisy signals. The underlying principle is that the wavelet transform is good at energy compaction, the small coefficients are more likely due to the noise and the large coefficients are due to the important

signal features. In other words, the signal component is sparse with respect to the wavelet bases. These small coefficients can be thresholded without affecting the significant features of the image. Thresholding is a nonlinear technique which operates on one wavelet coefficient at a time. In its most basic form, each coefficient is compared against a threshold, if the coefficient is smaller than the threshold then it is set to zero; otherwise it is either kept unaltered or modified through a non-linear transform. In [12], these two thresholding strategies are described as the *hard thresholding* and the *soft thresholding* respectively.

The application of the wavelet transform for despeckling of medical ultrasound images were reported in [37, 38, 40]. These methods use the logarithmic transformation of the speckled image before wavelet denoising and are generally referred to as the *homomorphic wavelet based despeckling* (HWDS) methods.

Zong [37] adopted a soft-thresholding method to remove the noise within the finer scales (such as levels 1 and/or 2) and hard thresholding within middle scales (such as levels 3 and/or 4) to enhance features. However, this thresholding method has two main limitations: 1) the choice of the threshold, the most important design parameter, is done in an ad hoc manner; and 2) the specific distributions of the signal and the noise are not at all considered. To address these issues, Simoncelli and Adelson [39] developed non-linear estimators in the wavelet domain, based on the formal Bayesian theory. They used a generalized Laplacian model for the highpass outputs corresponding to the ultrasound signal at different scales and subsequently estimated the signal using a MAP estimator. Achim *et al.* [40] developed a MAP estimator for ultrasound images by assuming an *alpha stable* prior for the signal. It assumes that after the log transformation, the speckle can be approximated by the zero-mean additive white Gaussian noise, and estimators/filters are designed accordingly. Solbø and Eltoft [115] proposed a homomorphic filter by modelling the wavelet coefficients of both the speckle and the signal using the *normal inverse Gaussian* distribution. In [116], Gupta *et al.* developed a MAP estimator by assuming a Rayleigh distribution to model the magnitude of speckle noise and a Gaussian distribution to model the signal respectively in the log domain.

Michailovich and Tannenbaum [44] proposed a modified HWDS algorithm by introducing a pre-processing procedure intended to change the noise statistics without changing the anatomical content of the image. They proposed the *Fisher-Tippet distribution* (FTD) to characterize the speckle in the log domain. Recently, Gupta *et al.* [42] proposed the two-sided *generalized Nakagami distribution* (GND) for modelling speckle and *generalized Gaussian distribution* (GGD) for modelling the image and used a Bayesian MAP estimator in the wavelet domain to estimate the desired signal. The

authors in [42] proposed two techniques for speckle suppression, namely, the *GNDShrink* and the *GNDThresh*.

The HWDS methods assume that after the log transformation speckle becomes additive and white Gaussian. However, speckle in ultrasound images is locally correlated [43]. Michailovich and Tannenbaum [44] carried out experiments on several ultrasound images both *in vivo* and *in vitro* and demonstrated that the autocorrelation function of the ultrasound image samples over any homogeneous region has a non-negligible support. Moreover, the speckle in the log-transformed ultrasound image is often spiky in nature with occasional outliers and cannot be modelled by the Gaussian distribution. These characteristics of speckle lead to poor performance of any traditional despeckling method including the HWDS methods. To overcome this, the authors in [44, 117] have proposed a preprocessing procedure on the envelope detected ultrasound images before applying the HWDS method. The preprocessing procedure includes the decorrelation and the Gaussianization of the speckle noise.

Redundant representations based on the multiscale transforms have been proved to be effective in removing speckle from different coherent imaging techniques including the medical ultrasound and the SAR imageries [45, 46, 118–123]. The UDWT is the most widely used redundant transform and has been applied for despeckling of ultrasound images [42, 45, 116, 124]. The redundant transforms produce a sparse representation of the signal in terms of the overcomplete basis. The overcomplete transform is important for denoising because of its robustness to noise and other forms of image degradations [69]. Another advantage of the redundant transform is its shift invariance which allows for small translation or scaling of local image features to result in smooth and graceful change in values of the sparse coefficients [62]. This distinctive feature is not present in the transforms with a fixed basis set such as wavelets.

The above study shows that the performance of the HWDS schemes can be improved by using the UDWT in place of the DWT and accurate analysis of the statistical properties of the log-transformed speckle noise. Further a denoising method based on the sparse representation of the signal requires the noise to be additive, uncorrelated and Gaussian for optimal performance [12]. The Gaussianization and decorrelation procedures in [44, 117] may be used as important preprocessing steps prior to the application of any sparsity-based denoising method.

In this chapter, the *generalized gamma distribution* (GGAD) is used to model the speckle in the positive detailed wavelet coefficients of the log-transformed medical ultrasound images for despeckling in a Bayesian framework. We then proposed a method for despeckling of medical ultrasound images

by incorporating the above preprocessing steps to the overcomplete UDWT-based soft thresholding method.

4.2 Theoretical Background

4.2.1 Speckled Image Model

As pointed out in Chapter 1, it is well established that the fully-developed speckle is a multiplicative noise [7] and can be modelled as

$$y = xn, \tag{4.1}$$

where n is modelled as a stationary and unity mean random variable independent of x.

The homomorphic despeckling methods take the advantage of the logarithmic transformation that, when applied to both sides of Equation (4.1), converts the multiplicative noise into an additive one. Taking logarithm on both sides of Equation 4.1, we get

$$f_l = g_l + \eta_l, \tag{4.2}$$

where f_l, g_l and η_l denote the logarithms of y, x and n, respectively. Thus in the log-transform domain, the speckle reduction problem of Equation (4.2) becomes a conventional problem of additive noise removal.

4.2.2 Speckle Statistics

The mechanism of the speckle formation in ultrasound imaging is similar to that of laser imaging [3], and the statistical description of the speckle noise generally depends upon the composition and the type of the tissues. For the case in which the resolution cell consists of a relatively large number of independent scatterers (more than 10, normally), the speckle amplitude is widely recognized to follow a Rayleigh distribution [5]. However, when the number of scatterers is low or their spatial locations are not independent, the distributions are likely to deviate from the Rayleigh model. In order to account for the non-Rayleigh scattering, a number of distributions have been proposed with varying success in despeckling. These include the Rician distribution, the K-distribution, the Nakagami distribution, and the Weibull distribution [125, 126].

The present research scenario demands a generalized model that can possibly describe the statistics of the speckle in a more general scattering environment.

4.3 Despeckling Based on Modelling of the UDWT Coeffcients

4.3.1 Filtering in the Discrete Wavelet Transform Domain

It is recognized that standard noise-filtering methods often result in blurred image features. Indeed, a single-scale representation of signals, either in time or in frequency, is often inadequate when attempting to separate signals from the noisy data.

During the last decade, the *discrete wavelet transform* (DWT) has become a popular and useful tool in signal and image processing. One of its main features is its ability to perform *multiresolution decomposition*. The DWT does this by projecting a signal $\mathbf{x}$ on to nested subspaces V_j of $L^2(\mathbb{R})$ that represent approximations $\mathbf{x}_j$ of the signal at different resolutions. As a result, the wavelet decomposition gives a simultaneous spatial and frequency domain representation of the signal.

The DWT of an image is implemented by filtering with a pair of quadrature mirror filters along the rows and columns alternatively, followed by downsampling by a factor of two in each direction [127], [9]. This filtering operation decomposes the image into four subbands LL, HL, LH, and HH at each level of decomposition. The LL subband contains the low frequency components in both directions, whereas HL, LH, and HH subbands contain the detail components in horizontal, vertical, and diagonal directions, respectively. The above filtering process is iterated on the LL subband, splitting it into four smaller subbands in the same way. The result is a multiresolution pyramid structure containing the information about the image at each scale.

The filtering method using the DWT is called the *wavelet shrinkage denoising* and was developed by Donoho and Johnstone [10, 12]. The main principle of wavelet shrinkage is that the wavelet representation can separate the signal and the noise. The DWT shows the energy compaction by distributing the energy of the signal into a small number of coefficients having large amplitudes and the noise on the other hand is spread over a large number of coefficients having small amplitudes. Hence a thresholding operation can be carried out to attenuate the noise energy by removing those small coefficients while maintaining the signal energy by keeping the large coefficients unchanged. There are two basic thresholding rules, namely, the hard thresholding and the soft thresholding. The hard thresholding is defined as:

$$\hat{X} = \begin{cases} Y, \text{ if } |Y| \geqslant t \\ 0, \text{ otherwise} \end{cases}, \tag{4.3}$$

and the soft thresholding is defined as:

$$\hat{X} = \begin{cases} Y - t, \text{ if } |Y| \geqslant t \\ Y + t, \text{ if } |Y| \leqslant -t \\ 0, \text{ otherwise} \end{cases}, \tag{4.4}$$

where Y represents a detail wavelet coefficient, $\hat{X}$ is the thresholded coefficient and t is a predefined threshold.

In DWT based denoising, the wavelet coefficients in the detail subbands obtained by the DWT are first thresholded. The thresholded coefficients along with the lowpass coefficients are then used to reconstruct the denoised image.

4.3.2 Removal of Speckle in the Undecimated Wavelet Transform Domain

As a consequence of the downsampling operations in the pyramidal algorithm, the DWT does not preserve translation invariance. The *undecimated wavelet transform* (UDWT) [128] is a special version of the DWT that preserves translation invariance. Instead of the downsampling operation, the UDWT utilizes recursively dilated filters in order to halve the bandwidth from one level to another.

Given a signal $\mathbf{x}$ of length m, the first step of the UDWT produces two sets of coefficients: (1) the approximation coefficients c_j and the detail coefficients d_j by convolving the signal $\mathbf{x}(= c_0)$ with the low-pass and high-pass filters h_0 and g_0 respectively. The next step splits the approximation coefficients c_1 in two parts using the same scheme, but with the modified filters obtained by upsampling the filters used for the previous step and replacing $\mathbf{x}$ by c_1. Then, the UDWT produces c_2 and d_2. In general, the one-dimensional UDWT decomposition can be described by

$$\begin{aligned} c_{j+1}[k] &= c_j[k] * h_j[k] \\ d_{j+1}[k] &= c_j[k] * g_j[k], \end{aligned} \tag{4.5}$$

where $*$ denotes the convolution operation and h_j and g_j respectively denote the low-pass and high-pass filters. The corresponding low-pass filters at scale $j+1$ is defined recursively as

$$h_{j+1}[k] = h_j[k] \uparrow 2 = \begin{cases} h_j\left[\frac{k}{2}\right], & k \text{ even} \\ 0, & \text{otherwise} \end{cases}, \tag{4.6}$$

where $\uparrow$ represents the upsampling operation. The high-pass filters $g_j[k]$ are defined similarly. The one-dimensional UDWT decomposition can be shown by a block diagram in Fig. 4.1. In order to

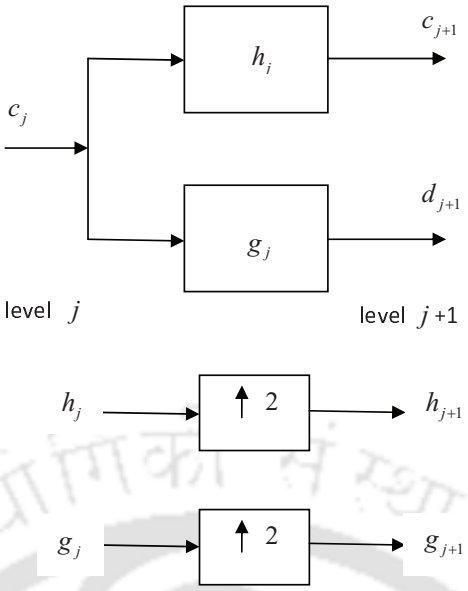

Fig. 4.1: One dimensional UDWT

reconstruct $\mathbf{x}$ in the original signal domain, one recursively performs the synthesis operation given by

$$c_j[k] = \frac{1}{2}\left(\tilde{h}_j[k] * c_{j+1}[k] + \tilde{g}_j[k] * d_{j+1}[k]\right) \tag{4.7}$$

where $\tilde{h}_j$ and $\tilde{g}_j$ are the reconstruction filters. The filters h_j, $\tilde{h}_j$, g_j, and $\tilde{g}_j$ obey the principle of perfect reconstruction [129]. The wavelet transform now becomes a shift-invariant operation.

The application of the UDWT to the log-transformed noisy image, f_l in Equation (4.2) gives

$$W(f_l) = W(g_l + \eta_l) = W(g_l) + W(\eta_l). \tag{4.8}$$

For notational simplicity Equation (4.8) is rewritten as

$$Y_l = X_l + N_l, \tag{4.9}$$

where $Y_l = W(f_l)$, $X_l = W(g_l)$, $N_l = W(\eta_l)$ are the random variables representing the UDWT coefficients of the noisy signal, the true signal and the noise after the log transformation, respectively. At each level of decomposition, four subbands (one approximation and three detail bands) are created. The approximation (lowpass) band in the first level is again decomposed into four subbands to get the second level of decomposition and so on. The highpass bands at all levels are considered for soft-thresholding based denoising.

The UDWT performs better than the DWT in denoising because: (1) By using all coefficients at each level, the high frequency information can be well preserved and (2) The number of pixels

involved in computing a given coefficient decreases so that the relation between the frequency and spatial information is more precise [15].

4.3.3 Modelling the UDWT Coefficients of Log-transformed Ultrasound Images

Modelling the signal component (X_l) in the wavelet domain

It has been observed that in the subband representation of medical images, the histograms of detailed wavelet coefficients have heavier tails and are more sharply peaked at zero. Such histograms cannot be modelled by the Gaussian distribution and the authors in [40] described an *alpha-stable distribution* for modelling these histograms. However a closed-form solution can not be obtained for this model. A well accepted model for modelling the histograms of detailed wavelet coefficients in the image processing community is the zero-mean generalized Gaussian distribution (GGD) [13].

In this work, we use the zero-mean GGD density for modelling the noise-free wavelet coefficients. The probability density function (pdf) of the GGD random variable X_l is given by:

$$\begin{aligned} f_{X_l}(x_l) &= C_{GGD}(\sigma_X, \tau) \exp\{-[K(\sigma_X, \tau)\,|x_l|]^\tau\}, \\ -\infty &< x_l < \infty, \;\; \sigma_X > 0, \tau > 0, \end{aligned} \tag{4.10}$$

where $K(\sigma_X, \tau) = \sigma_X^{-1}\left[\frac{\Gamma(\frac{3}{\tau})}{\Gamma(\frac{1}{\tau})}\right]^{\frac{1}{2}}$ and $C_{GGD}(\sigma_X, \tau) = \frac{\tau\, K(\sigma_X, \tau)}{2\Gamma(\frac{1}{\tau})}$. This distribution is described by two parameters- the standard deviation σ_X determining the spread of the pdf, and the parameter τ determining the shape of the pdf. Two special cases of the GGD are the Laplacian pdf (for $\tau = 1$)

$$f_{X_l}(x_l) = \frac{1}{\sigma_X \sqrt{2}} \exp\left(-\frac{\sqrt{2}\,|x_l|}{\sigma_X}\right), \tag{4.11}$$

and the Gaussian pdf (for $\tau = 2$)

$$f_{X_l}(x_l) = \frac{1}{\sigma_X \sqrt{2\pi}} \exp\left(-\frac{x_l^2}{2\sigma_X^2}\right). \tag{4.12}$$

These two special cases are particularly interesting because they are analytically tractable and hence will be used in this work.

Modelling the speckle component (N_l) in the wavelet domain

In [40], the authors used the Gaussian pdf for modelling the speckle wavelet coefficients after log transformation. Solbø and Eltoft [130] use the normal inverse Gaussian (NIG) distribution to model the speckle in the log domain. In [44], the authors used the Fisher-Tippett distribution (FTD) to

model the speckle after log transformation. The Gaussian pdf is the limiting case of such distributions. The FTD is more realistic for the fully-developed speckle that is when the number of scatterers are more and the speckle signal-to-noise ratio (SSNR) (defined in Section 4.8) is equal to 1.91. A particularly important concern is to model the speckle in image areas in which few scatterers are present and the SSNR is very poor (SSNR $\ll 1.91$) [125].

Recently, Gupta *et al.* [42] used the generalized Nakagami distribution (GND) as proposed by Shankar [126] to model the positive UDWT coefficients in the detail subbands of the log-transformed ultrasound images. This distribution well approximates speckle under different scattering conditions over a wide range of SSNR. They employ the *method of moments* (MM) to estimate the parameters of this model. But the GND is a variation of the generalized gamma distribution (GGAD) proposed in [125, 131]. We consider the GGAD for modelling the positive detailed coefficients in the UDWT decomposition of the log-transformed speckle data.

The method of moment (MM) [131] is not an optimal way to estimate the parameters of a distribution. In many situations, the method fails to take all the information available in the data samples. In fact, the MM solution can be taken as the first approximation for the numerical computation of other optimal estimators. We propose to use the *maximum likelihood estimation* (MLE) in place of the MM for the estimation of the GGAD parameters. The GGAD model is a versatile model and reduces to many well known distributions in limiting conditions. Some of them are the *gamma distribution*, the *Rayleigh distribution*, the *Nakagami distribution*, the *Exponential distribution* and the *Weibull distribution* [125]. The probability density function of a generalized gamma distributed random variable is defined as

$$f_{X_l}(x_l) = \frac{c x_l^{(cv-1)}}{a^{cv}\Gamma(v)} e^{-\left(\frac{x_l}{a}\right)^c}, \quad x_l \geqslant 0;\ a, v, c > 0, \tag{4.13}$$

where c and v are the shape parameters that provide flexibility in adjusting the shape of the pdf, and a is the scale parameter. c and v account for the tail behavior near and away from the origin and a determines the spread of the density function [125]. Assuming the equal probability of the negative and the positive speckle wavelet coefficients, we have used the two-sided GGAD model for approximating the speckle wavelet coefficients (N_l). The pdf of a two-sided GGAD distributed variable, N_l, can be defined as

$$f_{N_l}(n_l) = \frac{c\,|n_l|^{(cv-1)}}{2a^{cv}\Gamma(v)} e^{-\left(\frac{|n_l|}{a}\right)^c}, \quad -\infty < n_l < \infty;\ a, v, c > 0. \tag{4.14}$$

The positive part of the speckle wavelet coefficients obeys the one-sided GGAD distribution given by

$$f_{N_l}(n_l) = \frac{c n_l^{(cv-1)}}{a^{cv}\Gamma(v)} e^{-(\frac{n_l}{a})^c}, \quad n_l > 0;\ a, v, c > 0. \tag{4.15}$$

The distribution parameters c, v and a can be estimated from the subband data using the MLE technique. For distributions other than the Rayleigh, simple closed-form solutions for the parameters do not exist, and the MLE technique has been implemented through an optimization procedure similar to the one adopted in [125].

Experimental study of the GGAD model

In soft thresholding based wavelet denoising the HH_1 subband of the UDWT decomposition is used to estimate the noise [12]. We use the GGAD and other distributions to model the histograms of the positive components of the detailed UDWT coefficients. The parameters of the GGAD are estimated by the optimal MLE procedure given in subsection 4.4.4. Fig. 4.2 shows the modelling results with the Rayleigh, the Nakagami and the GGAD models for the images in Figs. 4.12i and 4.13i respectively. As observed in [42], the GGAD fits well the positive detailed coefficients of the log-transformed ultrasound images. The MLE estimate fits closely to the empirical data. Further, we study the goodness of the above three statistical models to fit the positive speckle wavelet coefficients using the Kolmogorov-Smirnov (KS) statistic as a goodness of fit measure. A smaller value of the KS statistic indicates a better fit of the particular distribution to empirical data [125]. Table 4.1 presents the results of the KS goodness-of-fit test at different orientations and scales for the speckled ultrasound image shown in Fig. 4.12i. The modelling results provide strong evidence that the GGAD provides a better fit to the tails of the empirical density of the speckle components compared to the Nakagami and Rayleigh distributions. This is further validated by the KS statistic values across different scales and orientations of wavelet decomposition for a speckled ultrasound image. In Table 4.1, we have seen that the GGAD model gives the better fit with the least value of KS statistic for a significance level of 0.05 in all the detailed subbands for three different decomposition levels as compared to the GGAD with the MM based estimation, Nakagami and Rayleigh models.

The above GGAD model for the speckle will be used for developing the UDWT based shrinkage functions for the despeckling of ultrasound images.

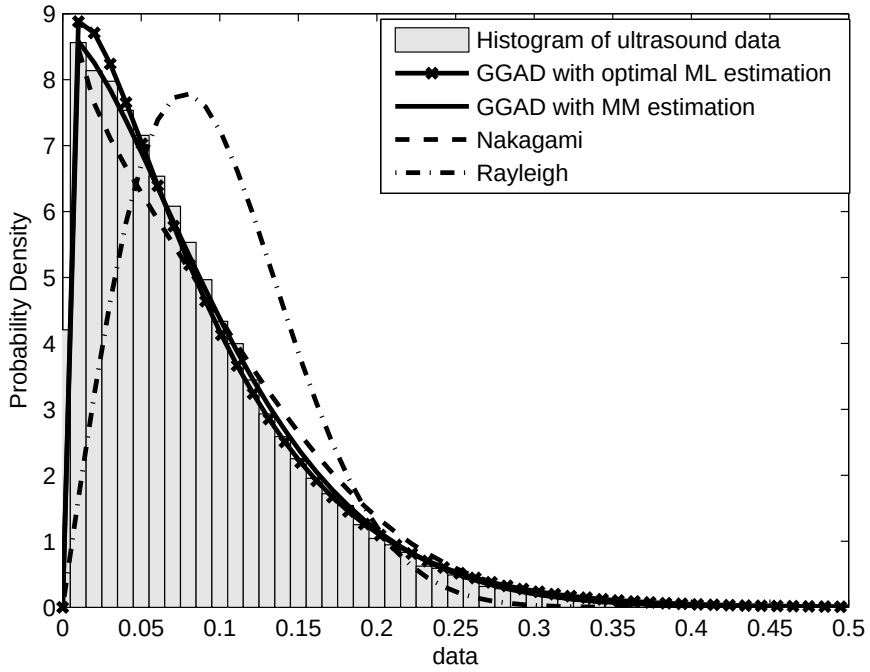

(a)

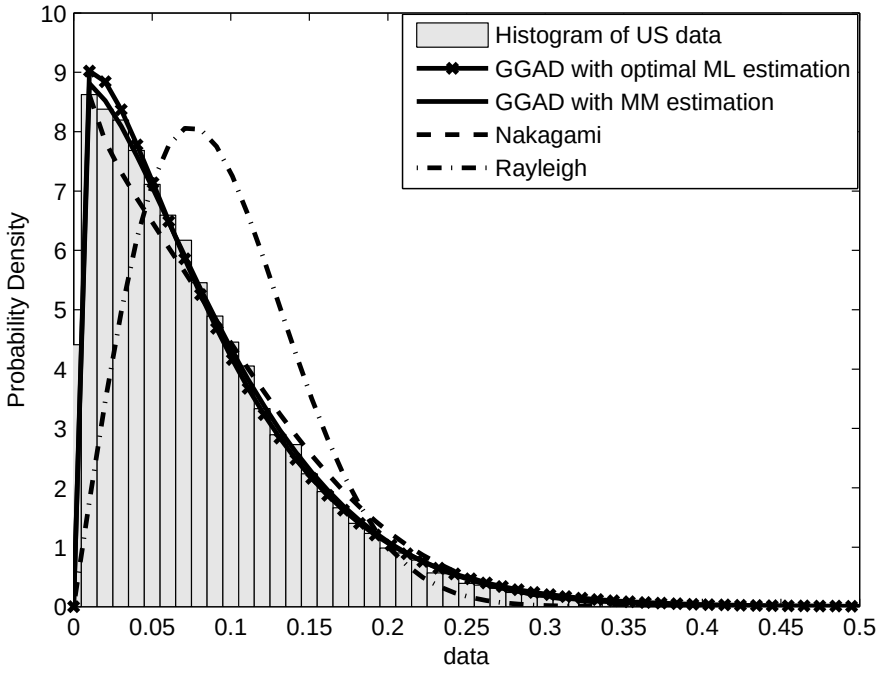

(b)

Fig. 4.2: Modelling of positive speckle wavelet coefficients using the GGAD, the Nakagami, and the Rayleigh models for the images shown in Figs. 4.12i and 4.13i respectively

Table. 4.1: The values of the Kolmogorov-Smirnov (KS) Goodness-of-fit test statistics at different orientations and scales estimated from a speckled ultrasound image shown in Fig. 4.12i

Level	Distributions	Orientations		
		HH	LH	HL
1	Rayleigh	0.1982	0.3013	0.1706
	Nakagami	0.0363	0.1209	0.0165
	GGAD with MM estimation	0.0688	0.0965	0.0131
	GGAD with optimal MLE	**0.0153**	**0.0385**	**0.0151**
2	Rayleigh	0.1863	0.2792	0.1843
	Nakagami	0.0198	0.0868	0.0190
	GGAD with MM estimation	0.0387	0.0895	0.0210
	GGAD with optimal MLE	**0.0157**	**0.0354**	**0.0197**
3	Rayleigh	0.1576	0.2555	0.2193
	Nakagami	0.0154	0.1233	0.0764
	GGAD with MM estimation	0.0299	0.0842	0.0851
	GGAD with optimal MLE	**0.0155**	**0.0651**	**0.0288**

4.3.4 Derivation of the Bayesian Shrinkage Functions

The goal here is to estimate for X_l from the noisy observation Y_l. The estimate will be denoted as $\hat{x}_l$. The MAP estimator is based on the pdf of X_l. It is given by

$$\hat{x}_l = \arg\max f_{X_l|Y_l}(x_l|y_l). \tag{4.16}$$

The pdf $f_{X_l|Y_l}(x_l|y_l)$ is the distribution of X_l given a specific value of Y_l. Using the Bayes' rule, *a posteriori* pdf of X_l based on the observed data Y_l, can be expressed as

$$f_{X_l|Y_l}(x_l|y_l) = \frac{f_{Y_l|X_l}(y_l|x_l) f_{X_l}(x_l)}{f_{Y_l}(y_l)}. \tag{4.17}$$

Because the term $f_{Y_l}(y_l)$ does not depend on X_l, the value of X_l that maximizes the right-hand side is not influenced by the denominator. Therefore, the estimate $\hat{x}_l$ of the signal X_l is given by

$$\hat{x}_l = \arg \max_{x_l} (\ f_{Y_l|X_l}(y_l|x_l)\, f_{X_l}(x_l)\ ). \tag{4.18}$$

For the assumed additive noise model given in Equation (4.2), $f_{Y_l|X_l}(y_l|x_l)$ can be written as

$$f_{Y_l|X_l}(y_l|x_l) = f_{N_l}(|y_l - x_l|). \tag{4.19}$$

Therefore, $\hat{x}_l$ is given by

$$\hat{x}_l = \arg \max_{x_l}(f_{N_l}(|y_l - x_l|))(f_{X_l}(x_l)). \tag{4.20}$$

Equivalently,

$$\frac{d}{dx_l}\left(\ln(f_{N_l}(|y_l - x_l|)) + \ln(f_{X_l}(x_l))\right)\Big|_{x_l=\hat{x}_l} = 0. \tag{4.21}$$

The solution of Equation (4.21) depends on the PDFs of the signal and the noise components of the wavelet coefficients. A closed-form form solution of the above equation cannot be obtained for the GGD model for the signal component.

In this study, Bayesian shrinkage functions for the Gaussian and the Laplacian PDFs have been derived.

(a) **When X_l is Gaussian distributed**

The substitution of Equation (4.12) and Equation (4.14) into Equation (4.21) gives

$$\frac{d}{dx_l}\left[\ln\left(\frac{c\,|y_l - x_l|^{(cv-1)}}{a^{cv}\Gamma(v)}\exp\left(-\left(\frac{|y_l - x_l|}{a}\right)^c\right)\right) + \ln\left(\frac{1}{\sigma_X\sqrt{2\pi}}\exp\left(\frac{-x_l^2}{2\sigma_X^2}\right)\right)\right]_{x_l=\hat{x}_l} = 0. \tag{4.22}$$

Simplification of the above equation leads to the estimator of x, i.e. the true signal to be

$$\hat{x}_l = sign\,(y_l)\left(\max\left(0, \frac{2|y_l|(A+a^c) - \sqrt{\left\{\begin{array}{l}\{2(A+a^c)\}^2 y_l^2 - \\ 4\{A(c-1)+2a^c\}\times \\ \{2cy^c\sigma_X^2 - 2a^c\sigma_X^2(cv-1)\}\end{array}\right\}}}{2\{A(c-1)+2a^c\}}\right)\right), \tag{4.23}$$

where $A = c^2\sigma_X^2 y_l^{c-2}$.

(b) **When X_l is Laplacian distributed**

The substitution of Equation (4.11) into Equation (4.20) gives

$$\frac{d}{dx_l}\left[\ln\left(\frac{c\,|y_l - x_l|^{(cv-1)}}{a^{cv}\Gamma(v)}\exp\left(-\left(\frac{|y_l - x_l|}{a}\right)^c\right)\right) + \ln\left(\frac{1}{\sigma_X\sqrt{2}}\exp\left(-\frac{\sqrt{2}\,|x_l|}{\sigma_X}\right)\right)\right]_{x_l=\hat{x}_l} = 0. \tag{4.24}$$

By solving Equation (4.24), one gets

$$\hat{x}_l = sign(y_l)\left(\max\left(0, \frac{cP|y_l| - \sqrt{2}a^c - \sqrt{\left(-cP|y_l| + \sqrt{2}a^c\right)^2 - 4P(c-1)\times \{Py_l^2 - (cv-1)a^c\sigma_X - \sqrt{2}|y_l|a^c\}}}{2P(c-1)}\right)\right), \tag{4.25}$$

where $P = c\sigma_X y_l^{c-2}$

4.4 Parameter Estimation

4.4.1 Estimation of σ_X^2

To adapt the above estimator to the local image statistics, the value of the parameter, σ_X^2 is to be computed for each wavelet coefficient from the local neighborhood. Since X_l and N_l are zero-mean and independent, we get

$$\sigma_{Y_l}^2 = \sigma_X^2 + \sigma_{N_l}^2. \tag{4.26}$$

The estimation of spatially varying parameter σ_X at a given spatial position can be computed as

$$\hat{\sigma}_X = \sqrt{\max(\hat{\sigma}_{Y_l}^2 - \sigma_{N_l}^2, 0)}, \tag{4.27}$$

and $\hat{\sigma}_{Y_l}^2$ can be obtained as

$$\hat{\sigma}_{Y_l}^2 = \frac{1}{t_w^2}\sum_{l,k\in W_i} Y_{l_{s,k}}^2, \qquad i \in Z^2, \tag{4.28}$$

where W_i is the window of size $t_w \times t_w$ centered at i and $Y_{l_{s,k}}$ is the wavelet coefficient in the detailed subband at location (s,k). $\sigma_{N_l}^2$ in Equation (4.27) is estimated as follows:

4.4.2 Estimation of $\sigma_{N_l}^2$

Donoho [11] proposed a formula to estimate the noise variance for additive noise model in the wavelet domain as

$$\sigma_{N_l}^2 = \left[\frac{median(|Y_l|)}{0.6745}\right]^2, \qquad Y_l \in \{HH_1\}. \tag{4.29}$$

Simard *et al.* [132] analyzed the effect of speckle correlation in the wavelet domain for SAR images and showed that the correlation properties of the speckle have an effect on the wavelet decompositions up to a scale that corresponds to its granular size. They suggested that the noise variance, should

be estimated from

$$\sigma_{N_l}^2 = \left[\gamma \frac{median(|Y_l|)}{0.6745}\right]^2, \quad Y_l \in \{HH_1, HH_2\}, \tag{4.30}$$

where γ is a tuning parameter [116] introduced to control the degree of smoothness of the denoised output. The proposed method uses Equation (4.30) to estimate $\sigma_{N_l}^2$.

4.4.3 Estimation of c, v and a

Stacy *et al.* [131] apply the method of moments to estimate the parameters of the GGAD. It is given by

$$\frac{\psi''(v)}{[\psi'(v)]^{1.5}} = -\left|\frac{E\left[\left(\ln(r) - \overline{\ln(r)}\right)^3\right]}{\left\{E\left[\left(\ln(r) - \overline{\ln(r)}\right)^2\right]\right\}^{1.5}}\right| \tag{4.31}$$

$$c = \sqrt{\frac{\psi'(v)}{E\left[\left(\ln(r) - \overline{\ln(r)}\right)^2\right]}} \tag{4.32}$$

$$a = E(r)\frac{\Gamma(v)}{\Gamma\left(v + \frac{1}{c}\right)}, \tag{4.33}$$

where $\psi'(v)$ and $\psi''(v)$ represent the first and second derivatives with respect to v, respectively and $\psi(v) = \frac{d}{dv}\ln[\Gamma(v)]$ is the digamma function. The value of v can be obtained by using the Gauss-Newton method [125]. The value of c is obtained using Equation (4.32), and subsequently the value of a is obtained using Equation (4.33). We have computed the parameters, namely, v, c and a from the positive wavelet coefficients of the diagonal details (HH_1, HH_2) assuming equal probability of the positive and negative wavelet coefficients.

The main drawbacks of the despeckling scheme based on modeling the UDWT coefficients in the log-transformed ultrasound image described above are:

1. It does not consider the correlation among the speckle noise samples.
2. The estimation of the GGAD parameters, namely, c,v and a is not optimal.
3. The estimation of σ_{N_l} using Equation (4.29) is optimal only when the noise is white and Gaussian [11].

4.4.4 Optimal Estimation of c, v and a

Consider that $n_{l_1}, n_{l_2}, \ldots, n_{l_m}$ denote the positive random sample values of the noise component N_l in the detail subbands of UDWT and $N_l \sim GGAD(n_l; c, v, a)$. The log likelihood function $\mathcal{L}$ is given

by

$$\mathcal{L} = \log\left[\left(\frac{c}{a^{cv}\Gamma(v)}\right)^{m}\left(\prod_{i=1}^{m} n_{l_i}^{cv-1}\right) e^{\left\{-\sum_{i=1}^{m}\left(\frac{n_{l_i}}{a}\right)^{c}\right\}}\right]. \tag{4.34}$$

In [125], ML estimation of the GGAD parameters is done through a numerical optimization procedure. It uses the Nelder-Mead simplex method for nonlinear optimization. The method [133] does not require the computation of derivatives but requires an initial guess of the solution. The initial guesses of the parameters were obtained using the method of moments as described in 4.4.3. With the estimation of the parameters v, c and a given by Equations (4.31)-(4.33) as the initial values, the optimal ML estimation is is carried out. We have used the *fminsearch* function available in Matlab optimization toolbox for implementation of the Nelder-Mead simplex method.

A modification of the method described in [42] is proposed in this work by estimating the GGAD parameters through the optimization method as explained above. We refer the modified method hereafter as the *GGADShrink* method. Particularly, the methods corresponding to the Gaussian and Laplacian priors for X_l will be called as *GGADShrink1* and *GGADShrink2* respectively. The overall block diagram of the despeckling algorithm based on modelling of the UDWT coefficients can be shown by the block diagram in Fig. 4.3.

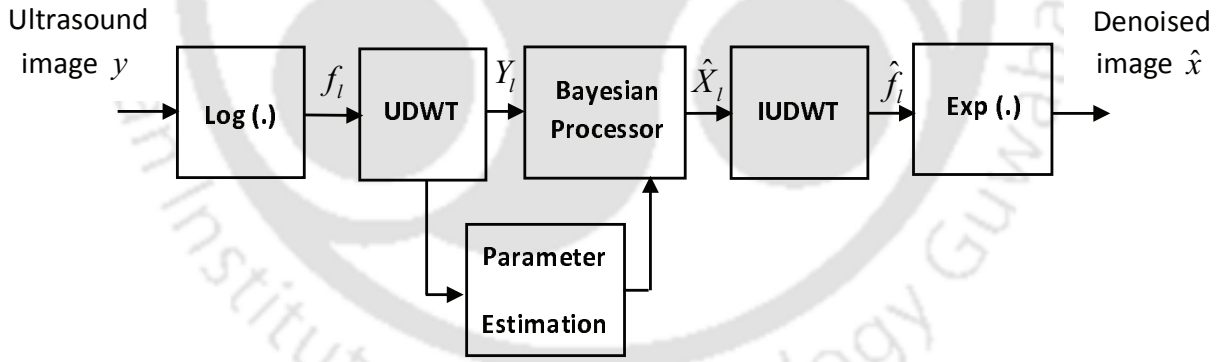

Fig. 4.3: Despeckling based on modelling of the UDWT Coeffcients

The experimental results by the proposed GGADShrink method is given at the end of the chapter.

4.5 UDWT Based Denoising of Preprocessed Ultrasound images

As pointed out above, the sparse denoising method based on the modelling of the UDWT coefficients assumes that the log-transformed speckle noise is white and the correlation among the speckle noise samples are not considered. As discussed earlier, the log-transformed speckle noise is non-Gaussian.

The UDWT based Bayesian shrinkage functions developed above to despeckle ultrasound images result in simple closed-form estimation of the signal if the log-transformed speckle is assumed to be Gaussian. Moreover, the parameter estimation in Section 4.4 is optimal when the noise is Gaussian. In [44], the authors have shown that the homomorphic despeckling methods based on the DWT can be improved by applying a preprocessing technique on the speckled ultrasound images. The preprocessing consists of two stages. In the first stage, the ultrasound image is subjected to a spectrum equalization procedure to decorrelate the image samples. In the second stage, a non-linear outlier shrinkage procedure is applied on the log-transformed ultrasound image to Gaussianize the noise. The result of this preprocessing is that the noise in the log-transformed image behaves very closely to the white Gaussian noise. The preprocessed images can be subsequently filtered using the sparse denoising methods for the removal of speckle noise. In the following, we carry out sparse denoising based on the soft-thresholding of the UDWT coefficients for despeckling of medical ultrasound images. In Chapter 5, we propose a method for the removal of speckle using sparse representations via overcomplete learned dictionaries.

4.6 Ultrasound Image Preprocessing

4.6.1 Image Formation Model

As discussed earlier, speckle in medical ultrasound images is an interference pattern produced due to the coherent accumulation of the waves scattered from the point scatterers much smaller in the scale of the ultrasound wavelength. It appears as a spatially correlated noise and degrades image quality and interpretability. In order to understand the spatial correlation in ultrasound image, we consider a standard image formation model where the backscattered signal and the tissue reflectivity function obey a simple relationship based on the linear system theory. Assuming linear wave propagation and weak scattering, the ultrasound image is considered to be the result of the convolution of the *point spread function* (PSF) of the imaging system with the *tissue reflectivity function* [44], given by

$$y(s,t) = h(s,t) * x(s,t) + u(s,t), \tag{4.35}$$

where $y(s,t)$, $h(s,t)$, and $x(s,t)$ denote the samples of the ultrasound image, the PSF, and the tissue reflectivity function, respectively at the locations (s,t) in the image plane and $*$ denotes the convolution operator. The tissue reflectivity function describes the overall reflections from a tissue via defining the relative strengths of acoustic reflectors and scatterers as a function of spatial co-

ordinates. The PSF is defined as the impulse response of the imaging system. Ideally, the PSF should be an impulse when a point target is imaged. The term $u(s,t)$ represents the samples of the measurement noise not covered by the convolution model.

The model given by Equation (4.35) considers the received image $y(s,t)$ to be a filtered version of the true reflectivity function $x(s,t)$. The spatial extent of the PSF is dependent upon the size of the aperture of the ultrasound transducer as well as the frequency of the ultrasound signal. Since the $h(s,t)$ is essentially the impulse response of a finite bandwidth low-pass filter, it introduces non-negligible spatial correlation to the ultrasound image [6]. The autocorrelation function $R_{xx}(h,k)$ for an image $\mathbf{x}$ is measured by

$$R_{xx}(h,k) = \sum_{s=0}^{m-1}\sum_{t=0}^{m-1} x(s,t)x(s+h,t+k), \tag{4.36}$$

Thus, any method developed to denoise the AWGN performs poorly in suppressing η_l in Equation (4.2). So, preprocessing of the ultrasound image is a necessary prerequisite step before using any HWDS method.

4.6.2 Decorrelation of Ultrasound Images

Suppose $P_y(\omega_1,\omega_2)$, $P_x(\omega_1,\omega_2)$, and $P_u(\omega_1,\omega_2)$ are the power spectral densities (PSD) of $y(s,t)$, $x(s,t)$, and $u(s,t)$, respectively and $H(\omega_1,\omega_2)$ denote the frequency response of the imaging system. Assuming $x(s,t)$ to be independent of $u(s,t)$, the following relationship can be derived.

$$P_y(\omega_1,\omega_2) = P_x(\omega_1,\omega_2)\,|H(\omega_1,\omega_2)|^2 + P_u(\omega_1,\omega_2). \tag{4.37}$$

In a biological system the tissue is formed by a large number of small independent structures resulting the heterogeneity of the tissue. Therefore, the samples of the tissue reflectivity function $x(s,t)$ can be reasonably assumed to be uncorrelated [44]. Thus,

$$P_x(\omega_1,\omega_2) = \sigma_x^2, \tag{4.38}$$

where σ_x^2 is the variance of $x(s,t)$. As the measurement noise $u(s,t)$ is also uncorrelated, we get

$$P_u(\omega_1,\omega_2) = \sigma_u^2. \tag{4.39}$$

Equation (4.37) now becomes

$$P_y(\omega_1,\omega_2) = \sigma_x^2\,|H(\omega_1,\omega_2)|^2 + \sigma_u^2. \tag{4.40}$$

Since the PSD of the noise is constant, the autocorrelation of the ultrasound image is completely

defined by $|H(\omega_1, \omega_2)|^2$.

Detail experiments on ultrasound images to demonstrate the correlation among the speckle noise samples have been discussed in the section on experimental results. For decorrelating the speckle noise samples, the PSD of Equation (4.40) is made equal to a constant value which is nothing but equalizing the power spectrum as reported in [117].

Inverse filtering

If the input to the decorrelating filter has the PSD given by Equation (4.40) then the output PSD must be constant indicating the process of decorrelation. Thus, the decorrelating filter can be chosen as the inverse of the square root of the input PSD. An inverse filter with its frequency response magnitude $|L(\omega_1, \omega_2)|$, is given by [117]

$$|L(\omega_1, \omega_2)| = \frac{1}{\sqrt{(|H(\omega_1, \omega_2)|^2 + \rho)}}, \tag{4.41}$$

where $\rho = \frac{\sigma_y^2}{\sigma_x^2}$ is the decorrelation parameter which can be varied in order to get the optimum decorrelation. Applying the inverse filter in Equation (4.41) to an ultrasound image results in flattening of its power spectral density (PSD), and therefore reduces the correlation among its samples.

PSF estimation

As the correlation results from the filtering action of the PSF, the ultrasound image can be decorrelated by the process of deconvolution. As the PSF here is not known *a priori*, *blind deconvolution* is needed and the PSF can be estimated from the ultrasound image using the procedure adopted in [134].

The convolution model in Equation (4.35) is valid only if weak scattering and linear wave propagation is assumed. We can assume the propagation as linear but weak scattering cannot be assumed because of the presence of specular reflectors in the tissues which give rise to acoustic reverberations. However, the number of regions occupied by such strong specular reflectors are a very few [4] and therefore the convolution model is quite able to approximate the image formation in ultrasound imaging.

Another limitation of the convolution model for the ultrasound image formation is due to the spatial variation of the PSF. It may change due to the presence of interrogated tissues between the transducer and a target. To mitigate this problem, one can assume that the PSF is locally

shift-invariant. Therefore, the whole ultrasound image can be divided into a number of overlapping segments small enough to consider the data within them to be roughly space invariant.

Segmentation of ultrasound image

The ultrasound image is divided into a number of overlapping segments for the PSF estimation. The reason for choosing overlapping segments is to avoid the visible artifacts that may occur on block boundaries. The approach that we consider in this work for segmentation of the ultrasound image is the one that was adopted in [134]. It compares the value of the speckle signal-to-noise ratio (SSNR) of the image blocks to 1.91 and subsequently keeps only those for which the SSNR is close to 1.91. This value of SSNR theoretically signifies the regions in the image containing the fully-developed speckle noise [5].

The overall block diagram for ultrasound image segmentation required for PSF estimation is shown in Fig. 4.4. The leftmost part shows a schematic of an ultrasound image with the horizontal lines denoting the boundaries of three overlapping segments in the *axial direction* (along the axis of an ultrasound beam). The middle part of the figure shows a set of three quasi-stationary image segments obtained as above. Finally, a number of image blocks are obtained within each quasi-stationary segment as shown by the rightmost part of Fig. 4.4. The segmentation procedure is

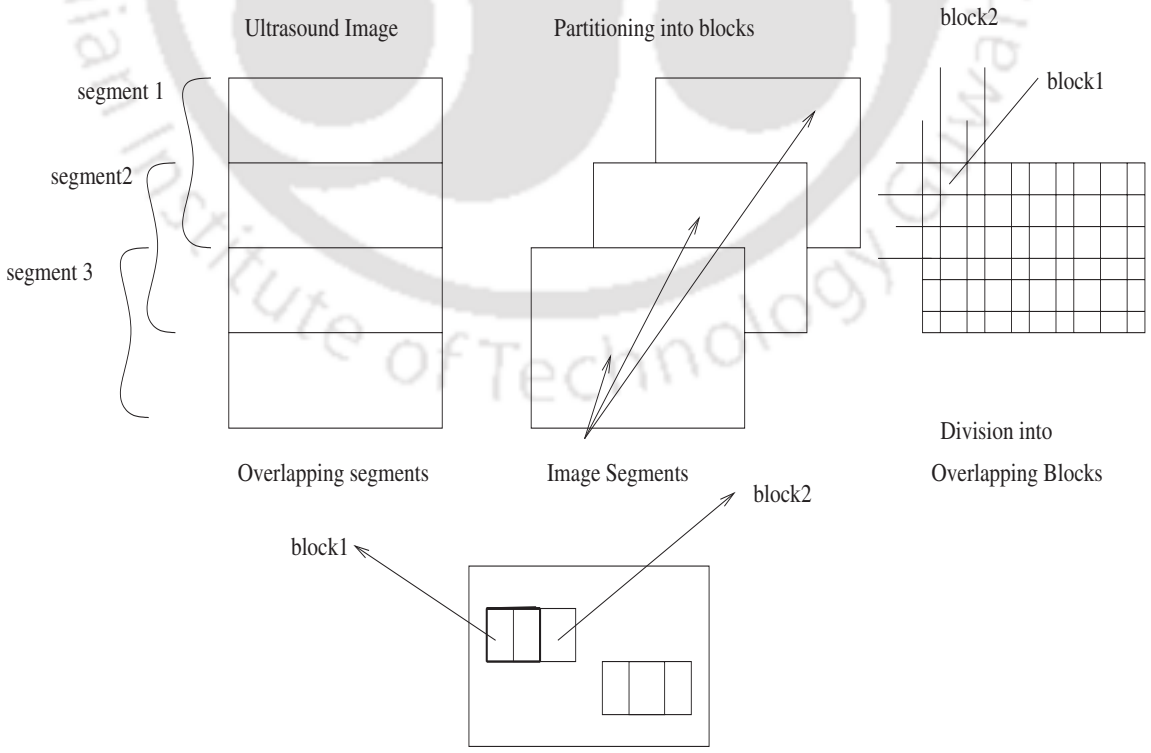

Fig. 4.4: Segmentation of image into overlapping blocks for estimating the PSF

performed along the axial direction (which is along the rows of the image matrix $\mathbf{x}$). This is due to the following reasons: (1) The lateral (along the columns of the image matrix $\mathbf{x}$) variation of the PSF at a given depth is mainly because of the dependency of the *spatial impulse response* of the transducer aperture on the lateral position of a target. This can be compensated by transducer *aperture apodization* which reduces the effect of transducer side-lobes and (2) A typical ultrasound image may extend a few thousand samples along the axial direction, while only a few hundred (or often even less) samples along the lateral direction. Thus, the lateral variations of the PSF can be assumed to be negligible, and the segmentation is performed along the axial direction only.

For a given quasi-stationary image segment, the PSF estimation is performed for all the image blocks selected on the basis of the SSNR. These PSF estimates are then averaged, to further reduce the estimation variance. The final PSF that will be used for decorrelation of the ultrasound image is the average PSF obtained as above.

Estimation of the PSF in a block

Let $Y_l(\omega_1, \omega_2)$, $X_l(\omega_1, \omega_2)$ and $H_l(\omega_1, \omega_2)$ denote the log-magnitude of the Fourier transforms (FT) of $y(s,t)$, $x(s,t)$ and $h(s,t)$, respectively of an image block obtained as above. Neglecting the noise term in Equation (4.35), the convolution model implies

$$Y_l(\omega_1, \omega_2) = H_l(\omega_1, \omega_2) + X_l(\omega_1, \omega_2). \tag{4.42}$$

Equation (4.42) shows that $H_l(\omega_1, \omega_2)$ could be estimated from $Y_l(\omega_1, \omega_2)$ by considering $X_l(\omega_1, \omega_2)$ as the noise. Thus the estimation of the PSF becomes a standard filtering problem. The samples of $X_l(\omega_1, \omega_2)$ obey the Fisher-Tippett distribution (FTD) assuming that the samples of $x(n,m)$ obey white Gaussian noise (WGN) [4]. The FTD is similar to the WGN except for a relatively small number of samples having large amplitudes which contribute to its long tail. As a result, such a noise may be viewed as a WGN contaminated by occasional outliers/transients [44]. These transients are reduced by a process called *outlier shrinkage* or *Gaussianization* [4] and defined by

$$R(\omega_1, \omega_2) = sign(\Delta Y_l(\omega_1, \omega_2))(|\Delta Y_l(\omega_1, \omega_2)| - t)_+, \tag{4.43}$$

where $R(\omega_1, \omega_2)$ is the robust residual. The term $\Delta Y_l(\omega_1, \omega_2)$ denotes the difference between Y_l and its median filtered version, t is a predefined threshold, and the operator $(x)_+$ returns x if $x > 0$ and 0 otherwise. At this stage, the term $(Y_l - R)$ is just a combination of the $H_l(\omega_1, \omega_2)$, and an approximately WGN represented by $X_l(\omega_1, \omega_2)$. Finally $(Y_l - R)$ is filtered using the Donoho's wavelet

based soft-thresholding method in Equation (4.4) to estimate H_l. After the denoising, exponential transformation is taken on the result to estimate $\hat{H}(\omega_1, \omega_2)$.

4.6.3 Gaussianization of the Log-transformed Speckle Noise

Different models are used to characterize the ultrasound image depending on the microstructure of the tissue parenchyma and properties of the incident acoustic wave. The speckle is usually a coherent part superimposed on the background diffused signals. A generalized model, the GGAD, is used to model the speckle component considering the versatility of this distribution to handle different cases.

It is shown in [44] that the log transformation of the GGAD random variable results in a double exponential type distribution with the pdf

$$f(\eta_l) = \frac{c}{\Gamma(v)} e^{\left\{cv(\eta_l - \log a) - e^{\{c(\eta_l - \log a)\}}\right\}}, \tag{4.44}$$

This pdf is very close in form to the Fisher-Tippett distribution (FTD) with the pdf

$$f(\eta_l) = 2e^{\left\{(2\eta_l - \log 2\sigma_{\eta_l}^2) - e^{\left\{2\eta_l - \log 2\sigma_{\eta_l}^2\right\}}\right\}}, \tag{4.45}$$

where $\sigma_{\eta_l}^2$ is the variance of the noise.

Considering the GGAD model for the speckle, the noise η_l in Equation (4.2) follows a double exponential distribution similar in form with the FTD. Clearly, the log-transformed noise data are to be Gaussianized prior to applying any denoising technique based on the AWGN concept. As demonstrated in [4], the FTD can be approximated theoretically by the Gaussian pdf with a fixed variance. However, the authors in [44] demonstrated that the FTD is antisymmetric and deviates from the Gaussian pdf away from its mean value. An example of the realization of the FTD noise and its pdf are shown in Fig. 4.5. It is observed from the figure that the FTD possesses a long tail on the left-hand side. This heavy tail behaviour is attributed due to the presence of a relatively small number of large amplitude samples in the noise ensemble. Thus, FTD can be assumed as the WGN with a few outliers. Therefore, as explained in subsection 4.6.2 in connection with the estimation of the PSF, the outlier-shrinkage or Gaussianization has to be carried out to smooth out these outliers. Once the outliers are removed from the log-transformed ultrasound image, the speckle can be treated as AWGN.

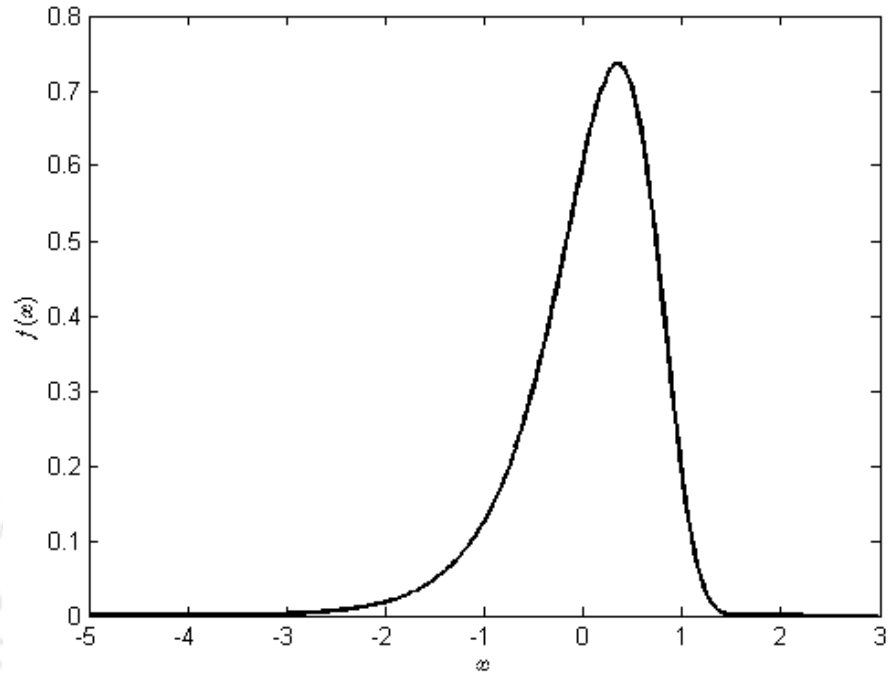

(a)

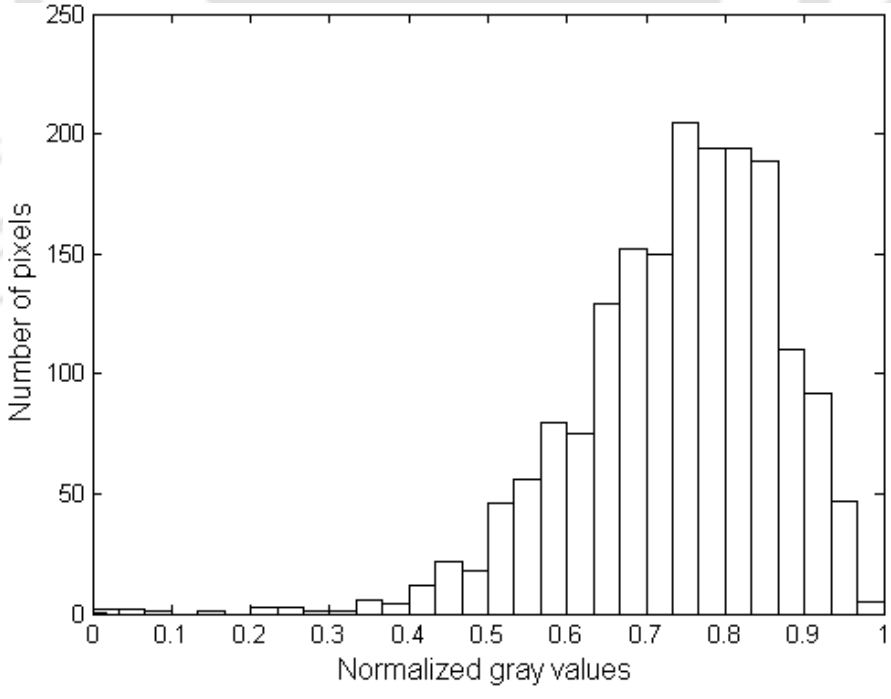

(b)

Fig. 4.5: (a) FT pdf and (b) the histogram of a log-transformed image segment of an ultrasound image in Fig. 4.8.

4.7 Proposed Despeckling Method

Based on the above discussion we conclude that the performance of the UDWT based despeckling can be improved by adopting the techniques described above. In this work we propose a despeckling algorithm based on the preprocessing and the UDWT based soft thresholding method. The UDWT based soft thresholding method is a modified version of the Donoho's method [11] by replacing the DWT with the UDWT. The proposed algorithm is referred as the *UDWT-STH* method in this work and can be summarized as follows:

Algorithm 5 UDWT-STH Method

1: Decorrelate the speckled image using the procedure discussed in Section 4.6.
2: Take the logarithmic transformation of the decorrelated image.
3: Apply the outlier shrinkage on the log-transformed image to Gaussianize the noise.
4: Perform UDWT on the above image.
5: Estimate the the noise variance $\sigma^2_{N_l}$ from the HH_1 and HH_2 subbands as described in Section 4.4.
6: **repeat**
7: For each subband except the lowpass residual

i. For each wavelet coeffcient in the detail subbands (HL, LH, and HH) find σ_X from a 3×3 neighbourhood.

ii. Estimate the signal component $\hat{x}_l$ using the shrinkage function given by Equation (4.4).

8: **until** all the wavelet decomposition levels.
9: Take the inverse UDWT to reconstruct the denoised image $\hat{f}_l$.
10: Take the exponential transformation to obtain $\hat{\mathbf{x}}$.

The overall block diagram of the proposed algorithm is shown by Fig. 4.6.

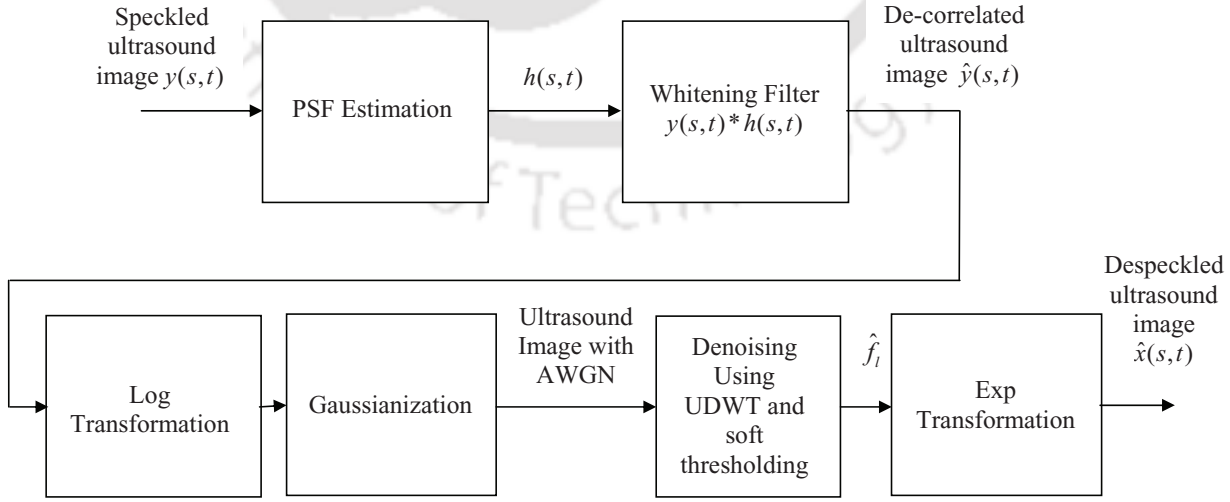

Fig. 4.6: Proposed despeckling algorithm using the UDWT-STH

4.8 Experimental Results

4.8.1 Image Database

To investigate the performance of the proposed algorithms, two image databases are considered. The first database consists of 50 ultrasound images of human liver, kidney, gallbladder, etc. collected from the Guwahati Neurological Research Centre, Guwahati. These images are cropped into the size of (256×256) for experimentation. The second database consists of five ultrasound images each of size (256×256) collected from http://telin.rug.ac.be/∽sanja. To demonstrate the working of the proposed method, a synthetic image (256×256 pixels) of geometric objects on a plain background is also considered. All these images are normalized to the range 0-1 for the computation purpose.

4.8.2 Simulation of the Speckle

To investigate the quantitative performance of the proposed method, ultrasound images are speckled using the speckle simulation model used in [40,45]. In this model, the complex Gaussian random fields representing the superimposed reflections from independent structures of the biological tissues are subjected to low-pass filtering by the point spread function of the imaging system. The amplitudes of the filtered outputs are biased to unity mean to get the speckle values. As in [40, 45], a 3×3 averaging filter is employed to model the PSF of the imaging system. By changing the variance of the complex Gaussian random field in Equation (4.1), the images with different levels of speckle noise ($\sigma_n = 0.2, 0.3, 0.4, 0.5, 0.6, 0.7, 0.8$) were generated.

4.8.3 Performance Evaluation Metrics

Consider an original image $\mathbf{x} = [x_1\ x_2\ \ldots\ x_m]^T$, the noisy image $\mathbf{y} = [y_1\ y_2\ \ldots\ y_m]^T$ and the denoised image $\hat{\mathbf{x}} = [\hat{x}_1\ \hat{x}_2\ \ldots\ \hat{x}_m]^T$. The following metrics are used to measure the performance of the proposed denoising scheme:

1. *Signal-to-MSE* (S/MSE) ratio in dB

   This measure is defined by

   $$\text{S/MSE} = 10 \log_{10} \left(\frac{\|\mathbf{x}\|_2^2}{\|\mathbf{x} - \hat{\mathbf{x}}\|_2^2} \right).$$

   A larger S/MSE value corresponds to a better quality of the denoised image.

2. *Speckle-signal-to-noise ratio* (SSNR)

It is defined as the ratio of the mean of the ultrasound image to its standard deviation. Thus, the SSNR of the noisy image $\mathbf{y}$ is given by

$$\text{SSNR}_{\mathbf{y}} = \frac{\overline{y}}{\sqrt{\frac{1}{m}\sum_{i=1}^{m}(y_i - \overline{y})^2}},$$

where $\overline{y} = \frac{1}{m}\sum_{i=1}^{m} y_i$ represents the DC of the noisy image $\mathbf{y}$. The SSNR of the reconstructed image $\hat{\mathbf{x}}$ is compared with that of the original image and given by

$$\text{SSNR}_{\hat{\mathbf{x}}} = \frac{\overline{\hat{x}}}{\sqrt{\frac{1}{m}\sum_{i=1}^{m}(\hat{x}_i - \overline{\hat{x}})^2}},$$

where $\overline{\hat{x}} = \frac{1}{m}\sum_{i=1}^{m} \hat{x}_i$. For denoising $\text{SSNR}_{\hat{\mathbf{x}}} > \text{SSNR}_{\mathbf{y}}$.

3. *Coefficient of correlation* (κ) The coefficient of correlation of $\mathbf{x}$ and $\hat{\mathbf{x}}$

$$\kappa = \frac{\Gamma\left(\mathbf{x} - \overline{\mathbf{x}},\, \hat{\mathbf{x}} - \overline{\hat{\mathbf{x}}}\right)}{\sqrt{\Gamma\left(\mathbf{x} - \overline{\mathbf{x}},\, \mathbf{x} - \overline{\mathbf{x}}\right)\Gamma\left(\hat{\mathbf{x}} - \overline{\hat{\mathbf{x}}},\, \hat{\mathbf{x}} - \overline{\hat{\mathbf{x}}}\right)}},$$

where

$$\Gamma(\mathbf{x} - \overline{\mathbf{x}}, \hat{\mathbf{x}} - \overline{\hat{\mathbf{x}}}) = \sum_{i=1}^{m}(x_i - \overline{x})(\hat{x}_i - \overline{\hat{x}}),$$

It is the measure of similarity between the original image and the despeckled image. Ideally, κ should be close to unity.

4. *Edge-preservation index* (β)

This is defined as

$$\beta = \frac{\Gamma\left(\Delta\mathbf{x} - \overline{\Delta\mathbf{x}},\ \ \Delta\hat{\mathbf{x}} - \overline{\Delta\hat{\mathbf{x}}}\right)}{\sqrt{\Gamma\left(\Delta\mathbf{x} - \overline{\Delta\mathbf{x}},\ \ \Delta\mathbf{x} - \overline{\Delta\mathbf{x}}\right)\ \Gamma\left(\Delta\hat{\mathbf{x}} - \overline{\Delta\hat{\mathbf{x}}},\ \ \Delta\hat{\mathbf{x}} - \overline{\Delta\hat{\mathbf{x}}}\right)}},$$

where $\Delta\mathbf{x}$ and $\Delta\hat{\mathbf{x}}$ are the high-pass filtered versions of $\mathbf{x}$ and $\hat{\mathbf{x}}$ respectively, obtained with a 3×3 standard approximation of the Laplacian operator. β measures the correlation between the outputs of a high-pass filter on the original and the denoised images. For good reconstruction, β should be close to unity.

5. *Ultrasound resolution index* (δ) [44]

This parameter measures the resolution in ultrasound imaging. Suppose $R^*_{\mathbf{x}}$ is the maximum value of the autocorrelation function of the image, and m_1 represents the number of pixels which exceeds $0.75R^*_{\mathbf{x}}$. Then the ultrasound resolution index δ_x of the original image x is

defined by

$$\delta_{\mathbf{x}} = \frac{m_1}{m}.$$

where m represents the total number of pixels in the image. Similarly, $\delta_{\hat{\mathbf{x}}}$ is defined. For denoising $\delta_{\hat{\mathbf{x}}} > \delta_{\mathbf{x}}$. Like the SSNR, this performance metric is particularly used in ultrasound despeckling because it can be measured without the knowledge of the original image.

Experiments were performed to study the proposed GGADShrink and UDWT-STH despeckling schemes. The results of the following experiments are reported.

A. Performance of the GGADShrink method

This experiment studies the performance of the GGADShrink method. For denoising of ultrasound images, all the images are first filtered with the homomorphic Wiener filter. The outputs of the homomorphic Wiener filter are then treated as the clean images. The filtered outputs are then artificially degraded with speckles using the simulation procedure described in subsection 4.8.2. For estimating σ_N^2 using Equation (4.30), we have chosen $\gamma = 3$ for all the ultrasound images as adopted in [42]. We used the Daubechies "db1" wavelet and four levels of decompositions for all the experiments.

Fig. 4.7 shows the results for despeckling of an ultrasound image speckled at $\sigma_n = 0.7$ using the GGADShrink1 method. From the figure it is observed that the GGADShrink method removes the speckle from the noisy image effectively. For quantitative evaluation of the GGADShrink method, we consider the two performance metrics, namely, the S/MSE and the SSNR. The results are presented in Table 4.2. The results show improvements in both the performance indices indicating that the GGADShrink method is successful in removing the speckle from an ultrasound image. The comparative results of the GGADShrink and other despeckling methods are presented later.

Table. 4.2: Results for despeckling an ultrasound image using the GGADShrink methods. The input values of S/MSE and SSNR are 11.4052 and 1.3740 respectively.

Method	Output S/MSE (in dB)	SSNR
GGADShrink1	17.7714	1.5176
GGADShrink2	18.1774	1.4193

B. Decorrelation and Gaussianization of the speckle.

In this experiment, segments of the ultrasound image without any visible organ structure are considered for studying the statistical properties of the speckle. Such homogeneous regions are characterized

(a) (b) (c)

Fig. 4.7: (a) Original image. (b) Speckled image at $\sigma_n = 0.7$ and (c) Denoised image using the GGADShrink1 method.

by a constant mean and may be considered to be composed of speckle only. Fig. 4.8b and Fig. 4.9b show two such regions in the ultrasound images in Fig. 4.8a and Fig. 4.9a respectively. In this case, the autocorrelation of the image segment represents the autocorrelation of the speckle noise field.

Fig. 4.8c and Fig. 4.9c show the plots of autocorrelations of the log-transformed segments in Fig. 4.8b and Fig. 4.9b respectively. The wide spread of the computed autocorrelation functions clearly shows that the speckle is not uncorrelated in the log-transformed image.

To decorrelate the speckle by the method discussed in subsection 4.6.2, the PSF of the imaging system is first computed. Fig. 4.8d and Fig. 4.9d show the plots of autocorrelation of the log-transformed segments after the decorrelation step. The sharp peaks of the autocorrelation functions illustrate the decorrelation action of the method. We have chosen the decorrelation parameter ρ in Equation (4.41) empirically in the range 0.2-0.5 for these images so as to achieve maximum decorrelation and control the amplification of the high frequency components in the image. This parameter in general should be less than unity.

To study the performance of the Gaussianization procedure, the log-transformed image segments are subjected to the Gaussianization procedure. Fig. 4.8e and Fig. 4.9e show the histograms of the selected image segments in the log-transform domain. The histograms show the long tail characteristics of the log-transformed data. The histograms after Gaussianization of the log-transformed data are plotted in Fig. 4.8f and Fig. 4.9f. The plots show that the histograms after Gaussianization look more Gaussian. For the test of Gaussianity, the kurtosis of the random variable representing the log-transformed ultrasound image before and after Gaussianization are determined. The kurtosis

value of a random variable X is measured by [97]

$$\text{Kurtosis} = \frac{E(X - \mu_X)^4}{\sigma_X^4} \tag{4.46}$$

where μ_X and σ_X^2 are the mean and variance of X respectively. In case of Gaussian distribution, the kurtosis value is 3. The kurtosis values of the two log-transformed image segments (shown in Fig. 4.8a and Fig. 4.9a) before Gaussianization are 5.4843 and 3.2938 respectively. After applying the Gaussianization method the corresponding values become 2.9888 and 2.8945 respectively. The decrease in the kurtosis values confirm that the log-transformed preprocessed data are more Gaussian.

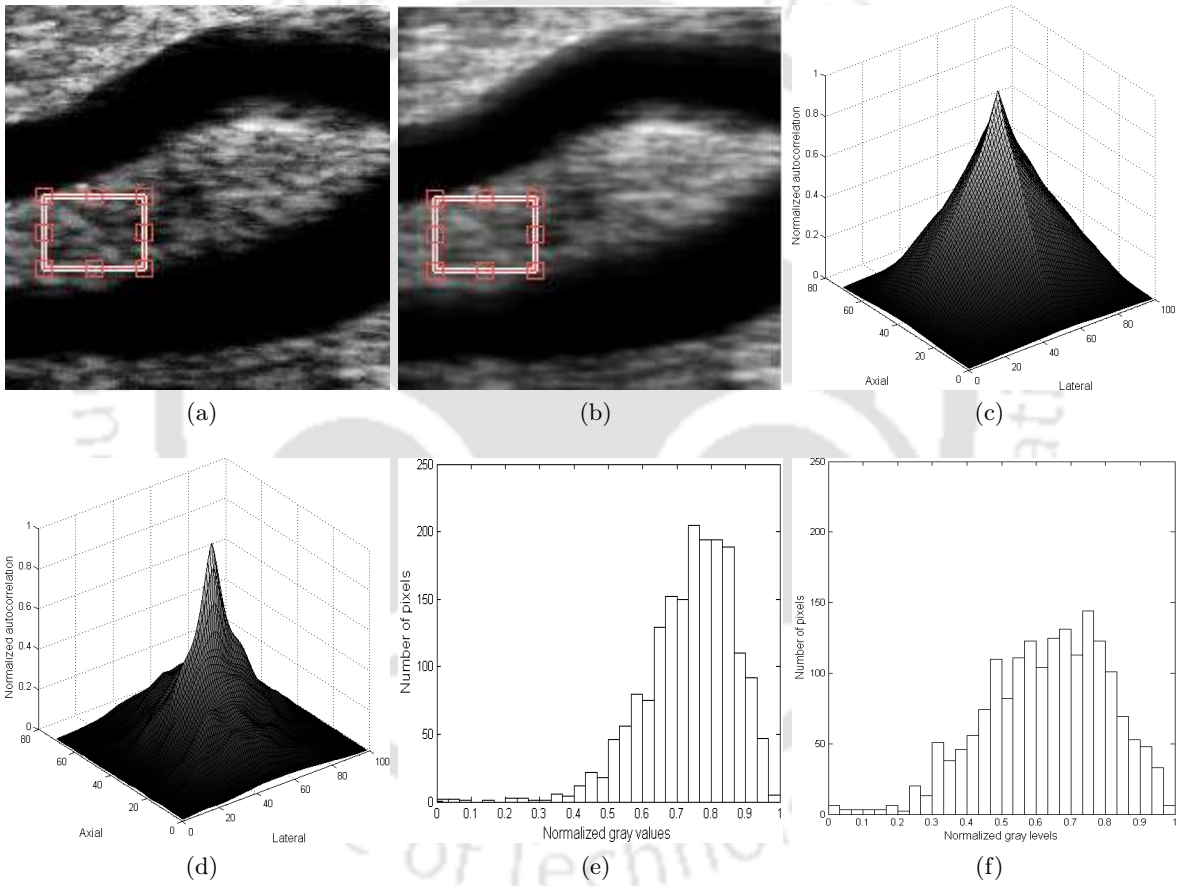

Fig. 4.8: (a) Original ultrasound image . (b) Decorrelated image. (c) Speckle autocorrelation for a log-transformed image segment shown inside the "box" before inverse filtering. (d) Speckle autocorrelation for the log-transformed image segment after inverse filtering. (e) Histogram of the log-transformed image segment without decorrelation and Gaussianization (f) Histogram of the log-transformed image segment after decorrelation and Gaussianization.

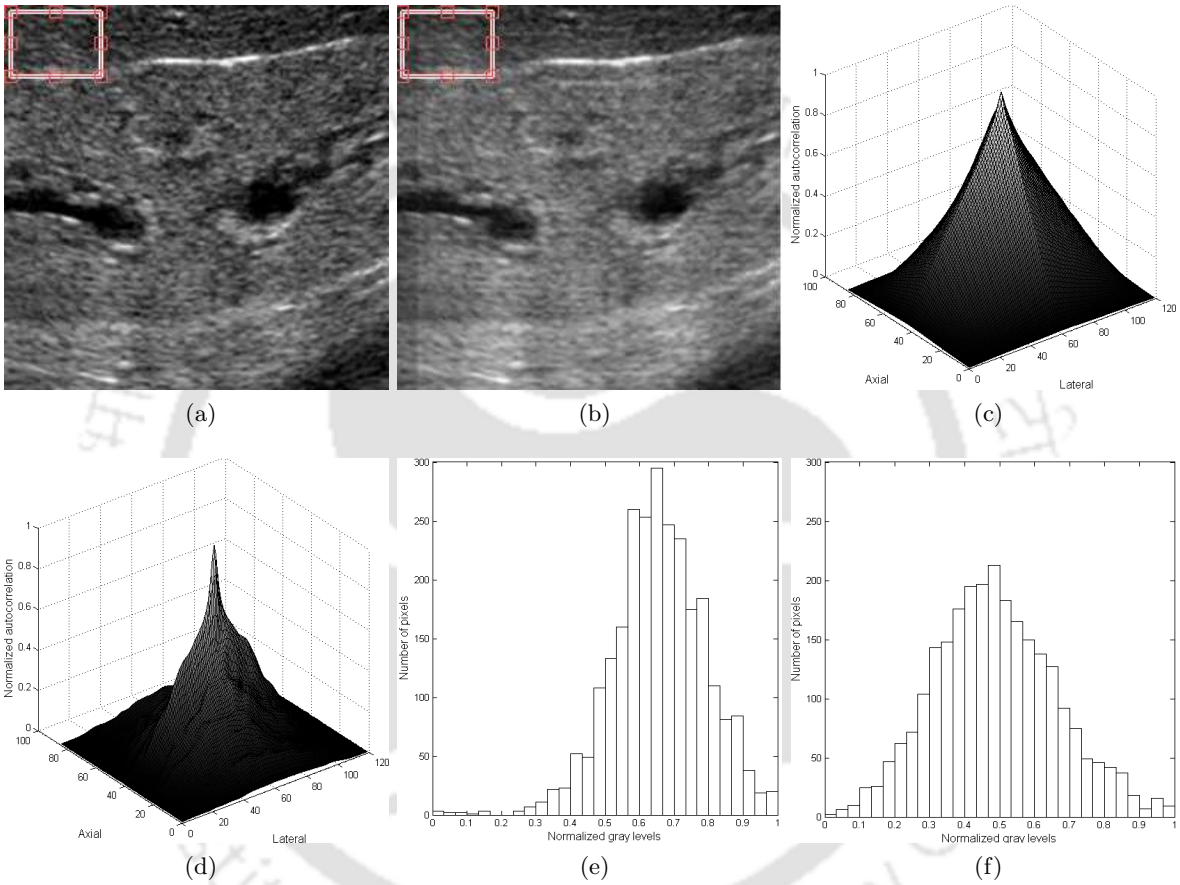

Fig. 4.9: (a) Original ultrasound image (b) Decorrelated image. (c) Speckle autocorrelation for a log-transformed image segment shown inside the "box" before inverse filtering. (d) Speckle autocorrelation for the log-transformed image segment after inverse filtering. (e) Histogram of the log-transformed image segment without decorrelation and Gaussianization (f) Histogram of the log-transformed image segment after decorrelation and Gaussianization.

C. Denoising performance of the UDWT-STH method on ultrasound and synthetic images at different noise levels.

In this experiment we investigate the denoising performance of the proposed algorithm on ultrasound and synthetic images for σ_n in the range 0.2 to 0.8 at an interval of 0.1. For the DWT based soft-thresholding (DWT-STH) and the UDWT-STH methods, the threshold is estimated as in [13]. For estimating σ_N^2, we have chosen $\gamma = 5$ for the synthetic image, and $\gamma = 3$ for the ultrasound images. The performance is measured in terms of S/MSEs in dB at different noise levels. The results are presented in Table 4.3 for the ultrasound image and the synthetic gray scale image shown in Fig. 4.14i and Fig. 4.15i, respectively. From these results it is evident that the proposed technique is capable of removing speckle at different noise levels. To assess the effectiveness of the proposed method visually, we also apply the proposed method to an ultrasound and a synthetic image corrupted by speckle noise at $\sigma_n = 0.6$. Fig. 4.10 and Fig. 4.11 show the denoised outputs using the proposed method. It is observed that the proposed method successfully removes the speckle in both the images.

Table. 4.3: Output S/MSE values for the UDWT-STH despeckling of (a) the ultrasound image (Fig. 4.14i) (b) the synthetic image (Fig. 4.15i) at different σ_n.

(a)

σ_n	Output S/MSE (in dB)
0.2	13.6508
0.3	13.6387
0.4	13.5448
0.5	13.4457
0.6	13.3310
0.7	13.2253
0.8	13.2060

(b)

σ_n	Output S/MSE (in dB)
0.2	17.8616
0.3	16.2506
0.4	14.5243
0.5	13.7012
0.6	13.3868
0.7	11.8171
0.8	11.1521

D. Denoising performance of the UDWT-STH method on different ultrasound images at the same noise level.

In this experiment different ultrasound images are considered for experimentation. These images are speckled for the same noise level $\sigma_n = 0.7$. We apply the proposed method on these images. Table 4.4 shows the output S/MSEs for all the ultrasound images. The results indicate that the proposed methods successfully removes the speckle from different ultrasound images corrupted with the same noise level.

Table. 4.4: Despeckling performance of the UDWT-STH method on different ultrasound images corrupted by the same noise level of $\sigma_n = 0.7$ in terms of output S/MSEs.

Input image	S/MSE (in dB)	
	input	output
Image1 (Fig. 4.8a)	13.5455	14.6990
Image2 (Fig. 4.9a)	12.8278	14.4255
Image3 (Fig. 4.12i)	11.4052	18.3774
Image4 (Fig. 4.13i)	10.2383	18.1774
Image5 (Fig. 4.14i)	11.3740	18.9239

(a) (b) (c)

Fig. 4.10: (a) Original image. (b) Speckled image at $\sigma_n = 0.6$ and (c) Denoised image using the UDWT-STH method.

E. Comparison of different despeckling methods.

In this experiment, despeckling of medical ultrasound and synthetic images are carried out using the state-of-the-art despeckling methods. The performance of the proposed UDWT based methods, namely, the *GGADShrink*, and the *UDWT-STH* are compared with the following methods: (a) Lee filter (LF) [33] (b) Homomorphic Wiener filter (HWF) [7] (c) Adaptive weighted median filter (AWMF) [35] (d) DWT based soft-thresholding (DWT-STH) [11] and (e) Bayesian shrinkage

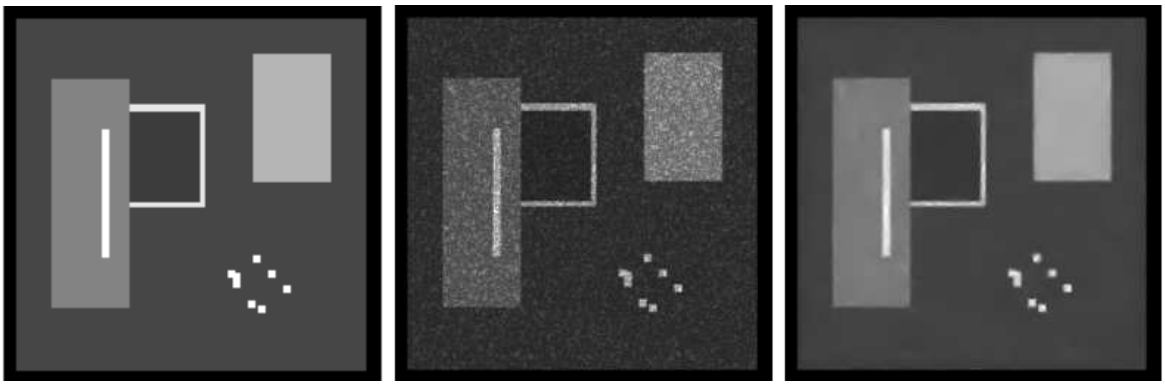

(a) (b) (c)

Fig. 4.11: (a) Original synthetic image. (b) Speckled image at $\sigma_n = 0.6$ and (c) Denoised image using the UDWT-STH method.

methods, namely, GNDShrink and GNDThresh [42]

For the quantitative performance, we considered the following performance metrics in this experiment: (1) SSNR (2) S/MSE (3) β and (4) κ. The quantitative results for various filtering methods are presented in Tables 4.5-4.7. Table 4.7 summarizes these metrics for the various filtering methods including the proposed UDWT based methods at two different noise levels for the synthetic image. For the ultrasound images (shown in Figs. 4.12i, 4.13i, and 4.14i respectively) the values of the quality metrics are given in Tables 4.5 and 4.6. All the numerical results are averaged over five runs to obtain stable values. The best results in each set are shown in bold face. The higher values of the performance evaluation metrics in almost all the cases indicate that the proposed UDWT-STH method can eliminate speckle efficiently. It is also observed that the proposed UDWT-STH method outperforms the GGADShrink and the DWT-STH methods for both the synthetic and medical ultrasound images at different noise levels. This is a consequence of the fact that the sparsity based denoising methods give optimal performance when the noise is Gaussian. The numerical results are further supported by qualitative comparison of the despeckled images with their respective original images shown in Figs. 4.12-4.15.

F. *In vivo* experiments

Due to the absence of noise free reference ultrasound images, the processed images using the various filtering schemes are presented to assess the image quality improvement for visualization. Fig. 4.16a shows the part of a ultrasound image (128×128) without degradation with artificial speckle. The corresponding outputs of the HWF, the LF, the AWMF, the DWT-STH, the GNDShrink, the GGADShrink and the UDWT-STH methods are shown in Fig. 4.16. Visual inspection of the processed

imaged reveals that proposed method yields good performance in terms speckle smoothing and edge preservation.

We also apply the UDWT-STH method to some of the representative images of the first dataset which contain visible speckles in them and are having low contrast to verify the efficacy of the proposed method. For quantitative measures *in vivo*, we consider only the metrics SSNR and δ as they do not need the knowledge of original image. Table 4.8 shows the results for the proposed method for different ultrasound images. It is clear from the results that the proposed method is able to remove speckle successfully.

4.9 Conclusion

In this chapter, we proposed an application of the sparsity based denoising for medical ultrasound images corrupted by speckle noise. It analyzed an existing UDWT based Bayesian MAP estimator using the GGAD distribution to model the positive high-pass coefficients of the log-transformed ultrasound images. The MLE principle is used for the estimation of the distribution parameters. Two UDWT based Bayesian shrinkage methods, namely, the GGADShrink1 and GGADShrink2 using the optimal parameter estimation perform better compared to that based on the parameter estimated using the method of moments. For applying the existing sparsity based denoising techniques, the noise model should be AWGN. Particularly, the soft-thresholding based wavelet denoising is optimal for the AWGN model. This chapter investigated the existing preprocessing methods for decorrelation and Gaussianization of the speckle noise in the log-transform domain. The preprocessed images are then subjected to soft-thresholding based UDWT denoising. The experimental results show superior performance of the UDWT-STH compared to the UDWT based Bayesian shrinkage methods and the DWT-STH method both qualitatively and quantitatively. The next chapter investigates sparse representation via overcomplete dictionary for despeckling of medical ultrasound images.

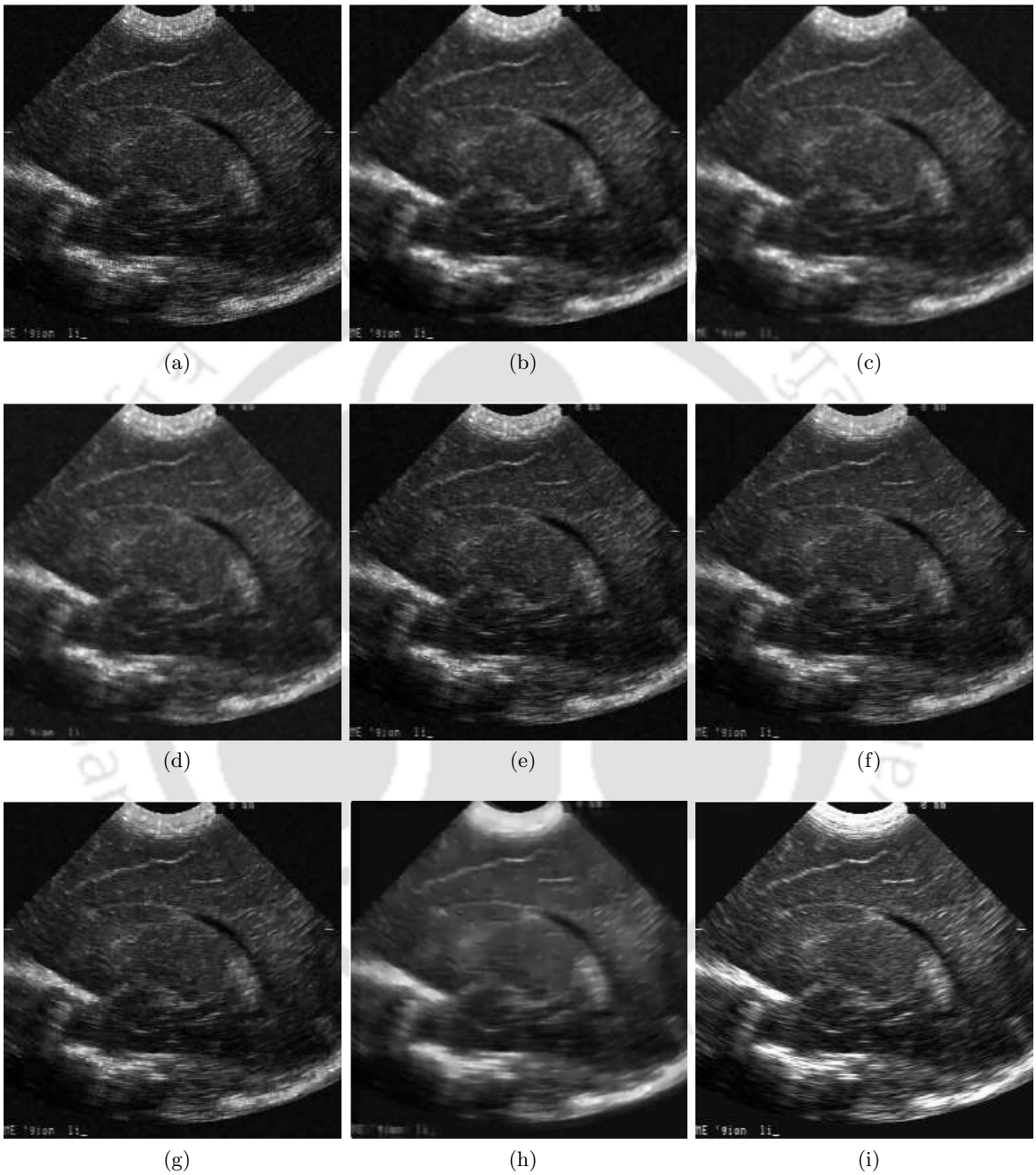

(a) (b) (c)

(d) (e) (f)

(g) (h) (i)

Fig. 4.12: Denoised results on the speckle simulated ultrasonic image. Outputs of (a) Speckled image at $\sigma_n = 0.7$. (b) HWF. (c) LF. (d) AWMF. (e) DWT-STH. (f) GNDShrink. (g) GGADShrink1. (h) UDWT-STH and (i) Original image.

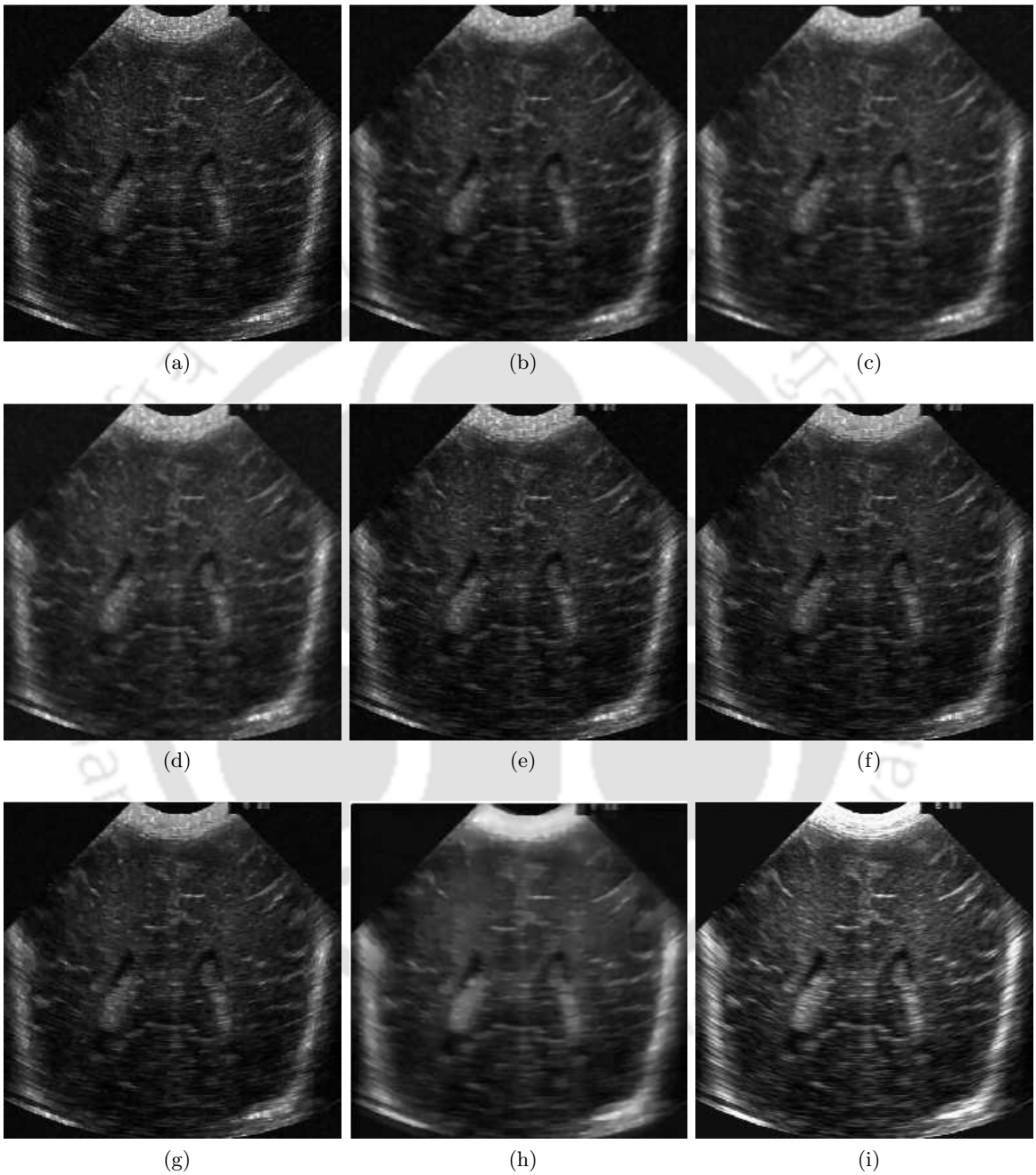

Fig. 4.13: Denoised results on the speckle simulated ultrasonic image. Outputs of (a) Speckled image at $\sigma_n = 0.6$. (b) HWF. (c) LF. (d) AWMF. (e) DWT-STH. (f) GNDShrink. (g) GGADShrink1. (h) UDWT-STH and (i) Original image.

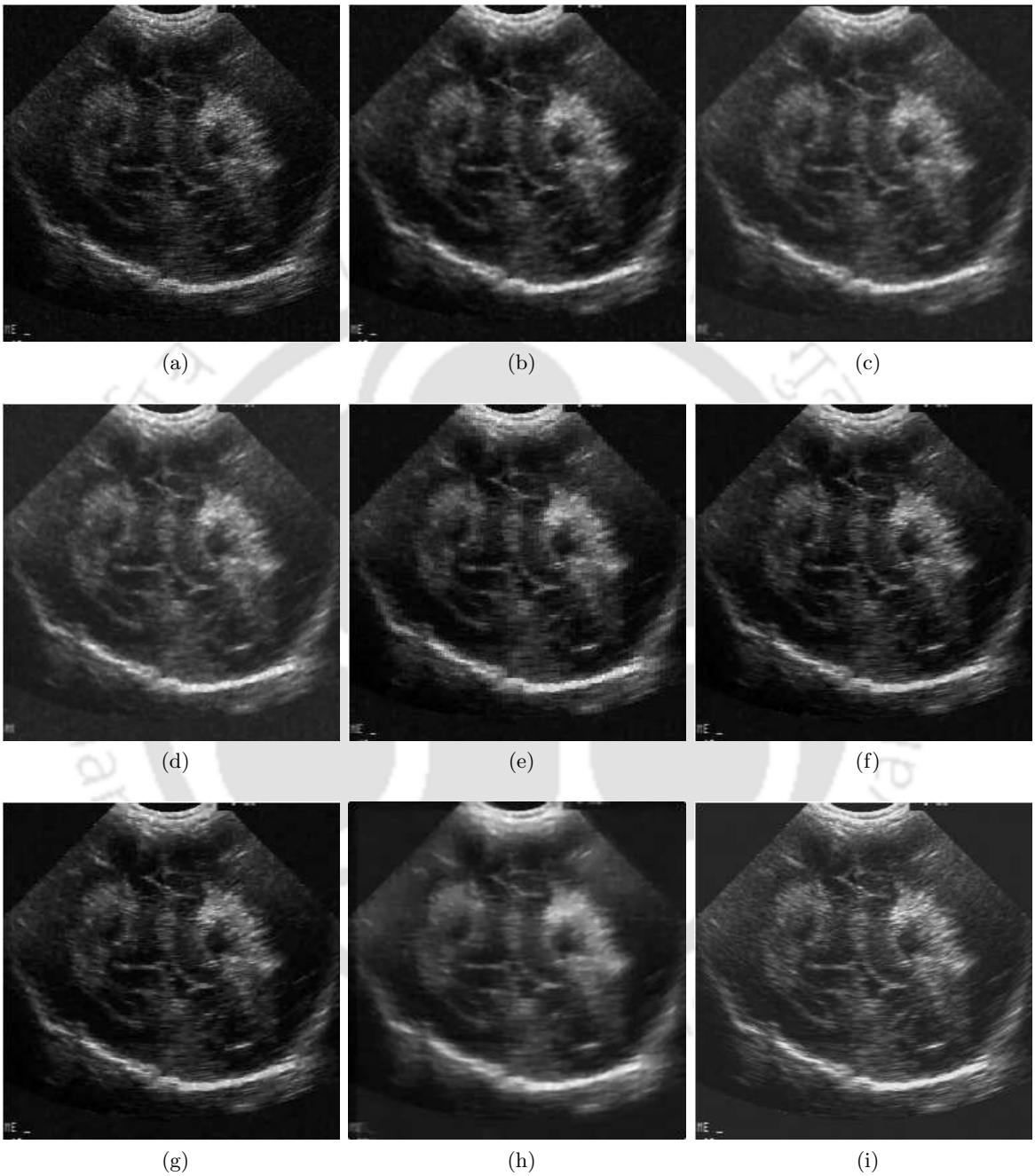

Fig. 4.14: Denoised results on the speckle simulated ultrasonic image. Outputs of (a) Speckled image at $\sigma_n = 0.5$. (b) HWF. (c) LF. (d) AWMF. (e) DWT-STH. (f) GNDShrink. (g) GGADShrink1. (h) UDWT-STH and (i) Original image.

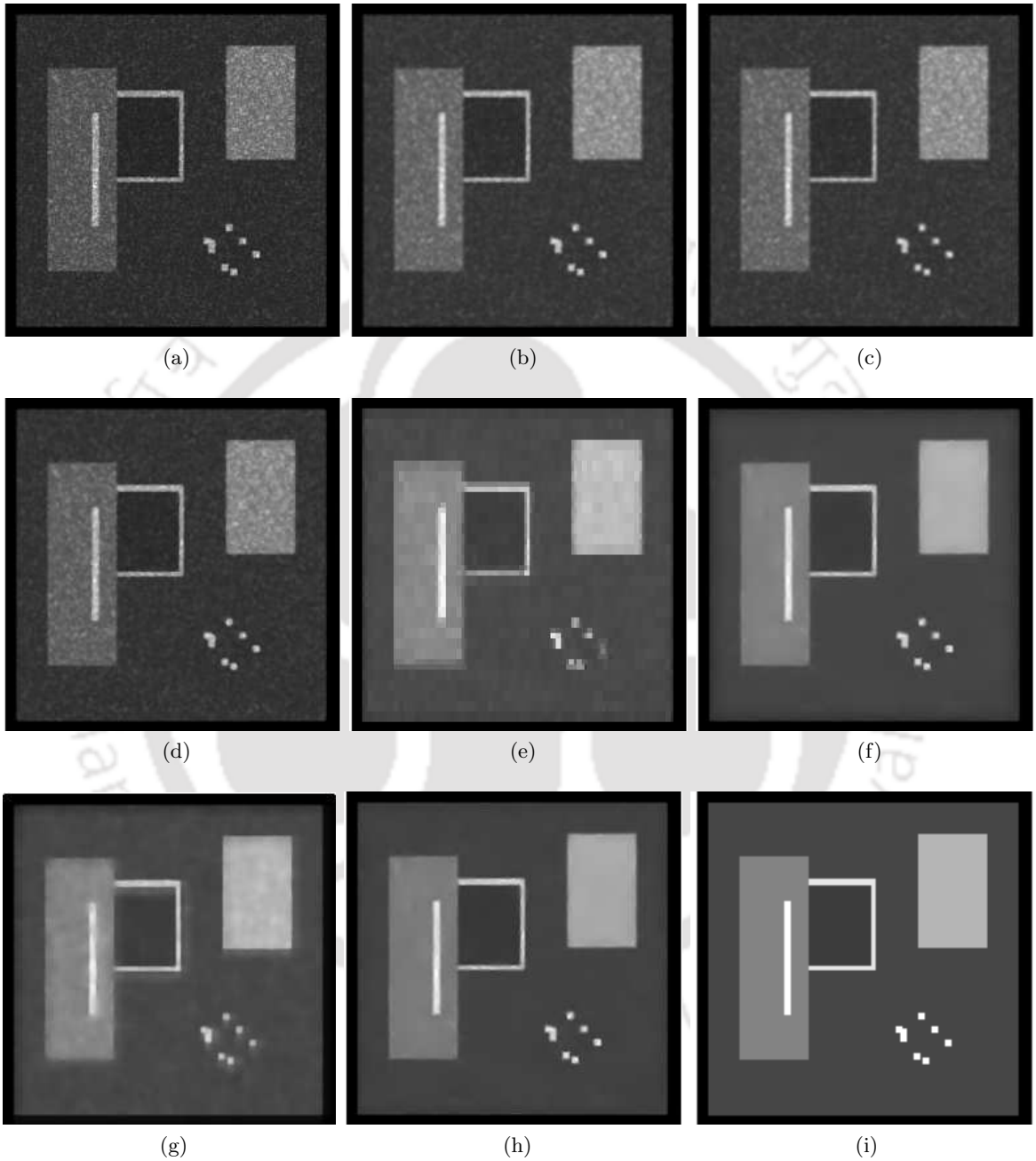

Fig. 4.15: Denoised results on the speckle simulated synthetic ultrasonic image. Outputs of (a) Speckled image at $\sigma_n = 0.6$. (b) HWF. (c) LF. (d) AWMF. (e) DWT-STH. (f) GNDShrink. (g) GGADShrink1. (h) UDWT-STH and (i) Original image.

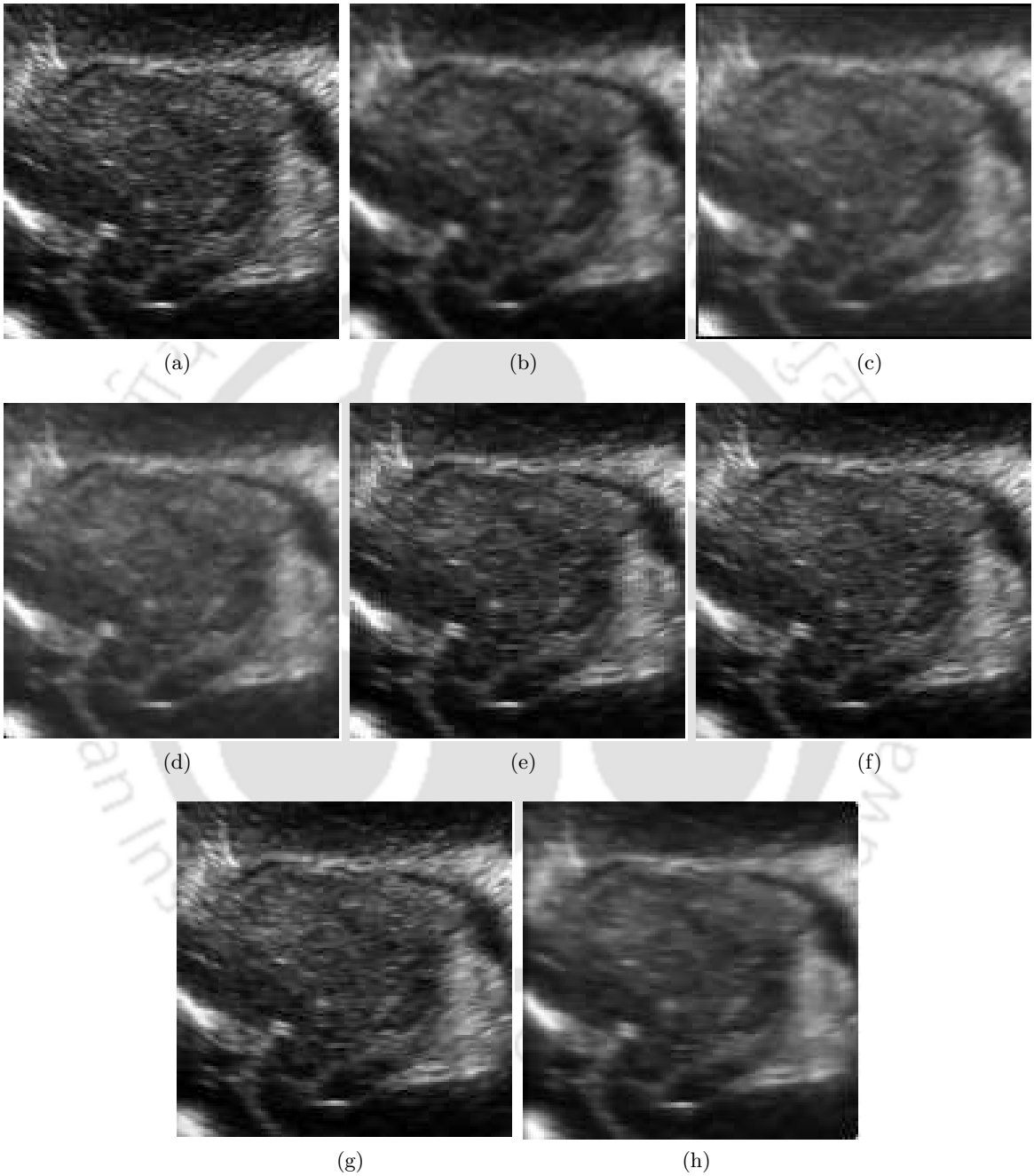

Fig. 4.16: Denoised results on a section of ultrasond image. (a) Original image. Outputs of (b) HWF. (c) LF. (d) AWMF. (e) DWT-STH. (f) GNDShrink. (g) GGADShrink1 and (h) UDWT-STH.

Table. 4.5: Image quality measures obtained for various denoising methods tested on speckled synthetic image 256×256 (Fig. 4.15i) at two input noise levels (i.e., $\sigma_n = 0.5$ and $\sigma_n = 0.6$ respectively) and with $\gamma = 5$. The S/MSE is given in dB and the other parameters (SSNR, β , κ) are the unit-less quantities. (a) Input SSNR 1.6079 , S/MSE=13.4278 dB. (b)Input SSNR 1.5947 , S/MSE=11.9983 dB.

(a)

Noise level	Method	Output			
		SSNR	S/MSE	β	κ
$\sigma_n = 0.5$	HWF	1.6578	22.7244	0.6531	0.9903
	LF	1.6459	21.7453	0.5217	0.9879
	AWMF	1.6421	22.7578	0.6662	0.9903
	DWT-STH	1.6973	18.8043	0.2952	0.9761
	GNDShrink	1.6592	22.1610	0.8916	0.9909
	GNDThresh	1.6590	22.1553	0.8889	0.9909
	GGADShrink1	1.6588	22.7445	0.8928	0.9921
	GGADShrink2	1.6442	24.9390	0.8882	0.9977
	UDWT-STH	**1.7479**	**28.8937**	**0.8978**	**0.9982**

(b)

Noise level	Method	Output			
		SSNR	S/MSE	β	κ
$\sigma_n = 0.6$	HWF	1.6544	21.6548	0.6046	0.9876
	LF	1.6427	20.8979	0.4863	0.9853
	AWMF	1.6388	21.3360	0.5991	0.9865
	DWT-STH	1.7075	18.2222	0.2965	0.9729
	GNDShrink	1.6621	21.6511	0.8661	0.9899
	GNDThresh	1.6619	21.6405	0.8616	0.9899
	GGADShrink1	1.6620	21.9864	**0.8668**	0.9907
	GGADShrink2	1.6478	27.4399	0.8576	0.9969
	UDWT-STH	**1.6678**	**27.9394**	0.8658	**0.9978**

Table. 4.6: Image quality measures obtained for various denoising methods tested on two 256×256 ultrasound images (Figs. 4.12i and 4.13i , respectively) at a input noise level of $\sigma_n = 0.7$ with $\gamma = 1$. The S/MSE is given in dB and the other parameters (SSNR, β , κ) are the unit-less quantities. (a) Input SSNR=1.3740,S/MSE=11.4052 dB. (b)Input SSNR=1.4176, S/MSE=10.2383 dB.

(a)

Noise level	Method	Output			
		SSNR	S/MSE	β	κ
$\sigma_n = 0.7$	HWF	1.4686	16.4554	0.5092	0.9657
	LF	1.4731	14.6225	0.0722	0.9471
	AWMF	1.4549	15.4550	0.3241	0.9563
	DWT-STH	1.4192	17.8469	0.7943	0.9751
	GNDShrink	1.5409	17.4774	0.8225	0.9767
	GNDThresh	1.5517	17.5409	0.8298	0.9781
	GGADShrink1	1.5176	17.7714	0.8228	0.9771
	GGADShrink2	1.4193	18.1774	0.8243	0.9769
	UDWT-STH	**1.6613**	**18.3774**	**0.8323**	**0.9898**

(b)

Noise level	Method	Output			
		SSNR	S/MSE	β	κ
$\sigma_n = 0.7$	HWF	1.5213	16.7595	0.5052	0.9663
	LF	1.5295	15.2000	0.1150	0.9516
	AWMF	1.5113	16.1963	0.4105	0.9613
	DWT-STH	1.4994	16.9905	0.6321	0.9678
	GNDShrink	1.5842	17.6448	0.7879	0.9752
	GNDThresh	1.6043	17.5877	0.7950	0.9761
	GGADShrink1	1.5734	17.7481	0.7877	0.9753
	GGADShrink2	1.4659	17.8620	0.7857	0.9740
	UDWT-STH	**1.6227**	**18.3774**	**0.8123**	**0.9869**

Table. 4.7: Image quality measures obtained for various denoising methods tested on 256 × 256 ultrasound images (Fig. 4.14i) at two input noise levels (i.e., $\sigma_n = 0.4$ and $\sigma_n = 0.5$ respectively) and with $\gamma = 1.5$. The S/MSE is given in dB and the other parameters (SSNR, β , κ) are the unit-less quantities. (a) Input SSNR 1.6731, S/MSE=15.3370 dB. (b)Input SSNR 1.6595 , S/MSE=13.3715 dB.

(a)

Noise level	Method	Output			
		SSNR	S/MSE	β	κ
$\sigma_n = 0.4$	HWF	1.7832	18.7272	0.5306	0.9745
	LF	1.7830	16.4229	0.1152	0.9555
	AWMF	1.7571	18.2605	0.4774	0.9710
	DWT-STH	1.7709	19.1358	0.6405	0.9776
	GNDShrink	1.8635	20.5112	0.8999	0.9876
	GNDThresh	1.8625	20.2427	0.8963	0.9869
	GGADShrink1	1.8253	21.3081	0.9005	0.9886
	GGADShrink2	1.7004	22.4457	0.8943	0.9889
	UDWT-STH	**1.8872**	**24.1554**	**0.9123**	**0.9969**

(b)

Noise level	Method	Output			
		SSNR	S/MSE	β	κ
$\sigma_n = 0.5$	HWF	1.7782	18.3552	0.5194	0.9720
	LF	1.7785	16.2115	0.1124	0.9532
	AWMF	1.7559	17.8115	0.4499	0.9678
	DWT-STH	1.7796	18.0753	0.5620	0.9700
	GNDShrink	1.8581	19.6651	0.8621	0.9834
	GNDThresh	1.8650	19.5783	0.8599	0.9834
	GGADShrink1	1.8422	19.9155	0.8623	0.9838
	GGADShrink2	1.6916	20.8938	0.8561	**0.9842**
	UDWT-STH	**1.8772**	**21.1452**	**0.8743**	0.9829

Table. 4.8: Results for the UDWT-STH method on various medical ultrasound images

Input image	SSNR		δ	
	input	output	input	output
Breast	1.5630	1.7629	0.0368	0.0683
Aorta	0.9155	1.0635	0.0059	0.0160
Abdomen	1.0693	1.1529	0.0102	0.0185
Carotid	1.0788	1.1094	0.0360	0.0462
Heart	0.7374	0.7760	0.0079	0.0121
Kidney	2.4083	2.9737	0.0595	0.0972
Liver	1.8230	2.1198	0.0232	0.0401
Renal	1.6490	1.8911	0.0675	0.1120
Spleen	1.2529	1.4358	0.0149	0.0372
Gallbladder	1.0864	1.1698	0.0163	0.0258

Chapter 5

Sparse Despeckling of Medical Ultrasound Images Using Overcomplete Dictionaries

5.1 Introduction

As discussed in Chapter 4, sparse denoising methods based on thresholding the discrete wavelet transform (DWT) and the undecimated wavelet transform (UDWT) coefficients have been used for despeckling of medical ultrasound images. In addition, many new multiscale redundant transforms such as the curvelets, the contourlets, the ridgelets, etc. have been proposed and found applications for the removal of speckle from coherent imagery [120–123].

An overcomplete dictionary of reasonable size can be adaptively trained from the given image data [69] to develop an efficient sparse representation of the image. The discovery of the matching pursuit [57] and the basis pursuit [55] algorithms and their ability to extract the signal from noisy data have led to the direct application of learned overcomplete dictionaries for image denoising. Aharon *et al.* [68] proposed the K-SVD algorithm as a generalization of the K-means algorithm for training a dictionary from a set of overlapping image patches using the singular value decomposition (SVD) method combined with a sparse coding of the image using the orthogonal matching pursuit (OMP) [58] algorithm. In [56], the authors adopted an example-based image restoration [135] technique via learned overcomplete dictionary obtained by the K-SVD algorithm. It was shown that the algorithm outperformed the state-of-the-art denoising methods for the removal of additive white Gaussian noise (AWGN) from images.

This chapter investigates the despeckling of medical ultrasound images using a K-SVD based

sparse representation method. Note that the speckle is locally correlated and cannot be assumed white and Gaussian after the log transformation. The sparsity based denoising methods are not suitable for the removal of this noise. Therefore, the speckle in these images are first decorrelated and then Gaussianized by applying the decorrelation and the Gaussianization procedures detailed in the previous chapter. The speckle in the preprocessed images can be approximately assumed to be additive white Gaussian noise in the log-transform domain. We propose to apply the K-SVD based image denoising method in the log-transform domain for the removal of multiplicative speckle noise from these preprocessed ultrasound images.

5.2 Prior Art

Chapter 2 discussed the sparse denoising method for AWGN corrupted images using an overcomplete dictionary learned through the K-SVD algorithm. The image $\mathbf{x} \in \mathbb{R}^m$ is assumed to have sparse representation in each patch of dimension $\sqrt{m_p} \times \sqrt{m_p}$. Addressing image denoising as a sparse decomposition problem on each patch leads to the following energy minimization problem:

$$\begin{aligned}\{\hat{\boldsymbol{\alpha}}_i, \hat{\mathbf{x}}\ , \hat{\boldsymbol{\Phi}}\}_{i=1,2,\ldots,M} = \arg\min_{\mathbf{x},\boldsymbol{\alpha}_i,\boldsymbol{\Phi}} \gamma \left\|\mathbf{x}-\mathbf{y}\right\|_2^2 \\ + \sum_i \left\|\mathbf{L}_i\mathbf{x} - \boldsymbol{\Phi}\boldsymbol{\alpha}_i\right\|_2^2 + \sum_i \lambda_i \left\|\boldsymbol{\alpha}_i\right\|_0 \end{aligned} \tag{5.1}$$

where the index i marks the location of the patch in the image, λ_i is the sparsity inducing regularization parameter and γ is used in connection with a global constraint related to σ_n. The sparse representation for the i^{th} patch using $\hat{\boldsymbol{\Phi}}$ is given by $\hat{\boldsymbol{\alpha}}_i$. The operator $\mathbf{L}_i$ is an $m_p \times m$ binary matrix which extracts the i^{th} patch from $\mathbf{x}$.

The above minimization problem is solved by using iteratively the OMP based sparse coding and the K-SVD based dictionary learning stages. Finally, the denoised image is obtained by a weighted averaging operation given by

$$\hat{\mathbf{x}} = \left[\gamma\mathbf{I} + \sum_i \mathbf{L}_i^T\mathbf{L}_i\right]^{-1}\left[\gamma\mathbf{y} + \sum_i \mathbf{L}_i^T\hat{\boldsymbol{\Phi}}\hat{\boldsymbol{\alpha}}_i\right] \tag{5.2}$$

where $\mathbf{I}$ is the identity matrix.

The K-SVD based sparse representation has proved successful in many image processing applications including sparse denoising, compression, and inpainting [68].

5.3 Sparse Despeckling of Ultrasound Images Using a K-SVD based Dictionary

The overall block diagram of the proposed sparse despeckling algorithm is shown in Fig. 5.1. The core idea is to convert the multiplicative speckle noise into approximately white and Gaussian noise through the preprocessing steps.

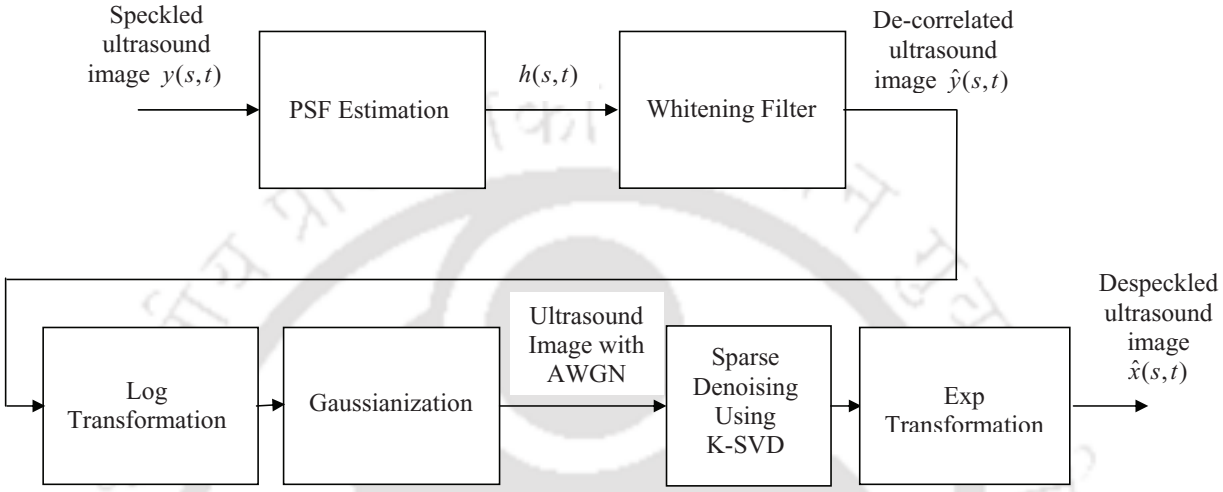

Fig. 5.1: Block diagram of the proposed de-speckling algorithm

5.3.1 Preprocessing of Ultrasound Images

The log transformation converts the multiplicative speckle into an additive noise. As pointed out in the previous chapter, ultrasound speckle is locally correlated and the log-transformed speckle follows the Fisher-Tippett distribution. In order to reduce the correlation of speckle, the ultrasound image is first decorrelated using the procedure detailed in subsection 4.6.2. After the decorrelation operation, the log-transformed image is Gaussianized through an outlier shrinkage operation to make speckle to be approximately white and Gaussian in the log-transform domain.

A greedy pursuit algorithm is applied on the resulting image with a dictionary learned through the K-SVD method.

5.3.2 Sparse Denoising Using K-SVD

Denoising via sparse representation consists of a sparse coding stage and a dictionary learning stage. The K-SVD based method of image denoising applies the OMP and the singular value decompositions

iteratively on the overlapping patches of the image. Finally the denoised image may be obtained by the weighted averaging operation in Equation (5.2).

However, the weighted averaging in Equation (5.2) will introduce a bias due to the logarithmic transformation carried out on the image $\mathbf{y}$ [123,136]. In order to adapt the same weighted averaging for the log-transformed ultrasound image, the parameter γ in Equation (5.2) is made zero [123]. In addition, the K-SVD based dictionary learning is performed only on the mean centered patch in order to approximate the high-frequency information of the patch and the mean of the patch is added subsequently to reconstruct the patch [68].

Therefore, the modified weighted averaging for denoising of the log-transformed ultrasound image can be written as

$$\hat{\mathbf{x}} = \left[\sum_i \mathbf{L}_i^T \mathbf{L}_i\right]^{-1} \left[\sum_i \mathbf{L}_i^T \left(\hat{\mathbf{\Phi}}\hat{\boldsymbol{\alpha}}_i + \langle \mathbf{y}_l \rangle_i\right)\right], \tag{5.3}$$

where $\langle . \rangle$ represents the local mean. The proposed despeckling algorithm can be summarized as follows:

Algorithm 6 Despeckling algorithm using the sparse representation

1: Decorrelate the speckled image using the procedure discussed in subsection 4.6.2.
2: Take the logarithmic transformation of the decorrelated image.
3: Apply the Gaussianization procedure on the log-transformed image as discussed in subsection 4.6.3.
4: Estimate the noise as discussed in subsection 4.4.2 and find the stopping parameter C using the method discussed in subsection 2.2.3.
5: Apply the iterative K-SVD based sparse denoising algorithm for the removal of additive white Gaussian noise.
6: Compute the weighted averaging operation using Equation (5.3) to obtain the reconstructed image.
7: Finally, take the exponential transformation of the denoised output.

5.4 Experimental Results

A number of experiments are carried out on the ultrasound images from the databases discussed in the previous chapter. We also consider two synthetic images for experimentation. The medical ultrasound images are first despeckled by using the standard homomorphic Wiener filter for considering the despeckled outputs as the original images. These original ultrasound images and the synthetic images are speckled artificially for different values of σ_n. An overcomplete dictionary is learned using the K-SVD method from the noisy image patches. It consists of 256 atoms arranged into column vectors of dimension 64×1 each and initialized by 256 randomly chosen patches from

the noisy image itself. The denoising is achieved iteratively by running the OMP and the K-SVD based dictionary learning. The value of the stopping parameter C in Equation (2.33) is found to be 1.14 for $m_p = 64$. The algorithm is run for 5-10 iterations for convergence. All the numerical results are averaged over 3 runs to obtain stable values. The following performance evaluation metrics are used for quantitative assessment of the denoised outputs:

1. SSNR
2. S/MSE
3. β and
4. δ.

These metrics are described in subsection 4.8.3.

A. Performance of the K-SVD based method applied directly on log-transformed ultrasound images

In the first experiment, the K-SVD based sparse denoising is applied directly on the log-transformed ultrasound images without the preprocessing steps. These ultrasound images are selected from the database in such a way that they contain some visible natural speckle. No artificial speckle was added. Fig. 5.2 and Fig. 5.3 show the ultrasound images and the corresponding denoised outputs obtained by the K-SVD denoising method for 10 iterations. It is observed that the denoised images are difficult to be distinguished from their corresponding noisy images. This means that the speckle is not removed effectively by the the K-SVD method if applied directly on the log-transformed image without preprocessing. This is further verified quantitatively by the SSNR values shown in Table 5.1. The input and output SSNR values for both the images differ only slightly indicating that the K-SVD method fails to remove speckle effectively. In the second experiment, we consider an ultrasound

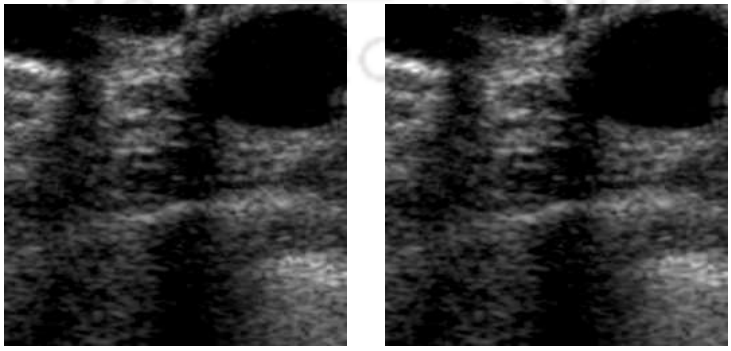

(a) (b)

Fig. 5.2: (a) Noisy ultrasound image and (b) denoised image using the K-SVD based sparse denoising directly on the log-transformed image.

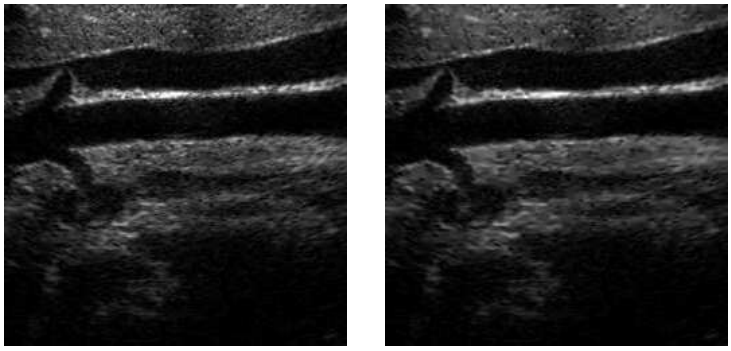

(a) (b)

Fig. 5.3: (a) Noisy ultrasound image and (b) denoised image using the K-SVD based sparse denoising directly on the log-transformed image.

Table. 5.1: Comparison of SSNR values of the denoised outputs using the K-SVD method

Input image	SSNR	
	input	output
Image1 (5.2a)	1.0693	1.0700
Image2 (5.3a)	0.9285	0.9302
Image3 (5.4b)	1.7829	1.7879

image corrupted by simulated speckle at $\sigma_n = 0.5$. Then, the K-SVD based sparse denoising is applied on the log-transformed speckled image. Figs. 5.4a-5.4c show the original image, the noisy image and the speckled image, respectively. The corresponding SSNR values are reported in Table 5.1. It is observed that the K-SVD method directly applied on the log-transform domain fails to remove the noise from the speckled image.

(a) (b) (c)

Fig. 5.4: (a) Original ultrasound image (b) Speckled image with $\sigma_n = 0.5$ and (c) denoised image using the K-SVD based sparse denoising directly on the log-transformed image.

B. Denoising performance of the proposed method

In this experiment, we consider both the synthetic and ultrasound images. The ultrasound images are first denoised with the homomorphic Wiener filter and the filtered outputs are then considered as the original images. Both the synthetic and ultrasound images are corrupted by the simulated speckle at $\sigma_n = 0.3$. The speckled images are then subjected to decorrelation. The decorrelated images are then subjected to log-transformation followed by the Gaussianization as shown in Fig. 5.1. We have considered the soft thresholding based DWT and the UDWT methods, DWT-STH and UDWT-STH for comparison of the denoising performances. We use four levels of wavelet decompositions using the Daubechies wavelet with six vanishing moments for implementation of these methods.

(a) Performance on synthetic images

We first consider the denoising performance of the proposed method on two synthetic images corrupted by speckle at $\sigma_n = 0.3$. Fig. 5.5 shows the outputs of the proposed method and the two soft thresholding based methods. Fig. 5.6 shows the outputs of various denoising methods for another synthetic image. Fig. 5.5e and Fig. 5.6e show that the proposed method is able to remove the speckle from both the images effectively and provides better smoothing in homogeneous regions compared to the soft thresholding based methods.

(b) Performance on ultrasound images

We consider a number of preprocessed ultrasound images and corrupt them with the simulated speckle at different σ_n. Fig. 5.7a shows an ultrasound image corrupted by speckle at $\sigma_n = 0.3$. Fig 5.7e shows the output of the proposed method. The outputs of the UDWT-STH and the DWT-STH are shown in Figs. 5.7c and 5.7d, respectively. It is observed that the proposed method is not only able to remove the speckle but also preserve the detail features in the image better than the UDWT-STH and the DWT-STH methods. The soft thresholding based methods cause oversmoothing in their corresponding outputs. Table 5.2 shows the performance of the proposed method and the soft thresholding methods at different values of σ_n in terms of S/MSE and β for the ultrasound image in Fig. 5.7a. The table shows the superior performance by the proposed method consistently at all noise levels. The performance at higher noise levels is significantly better than the other methods.

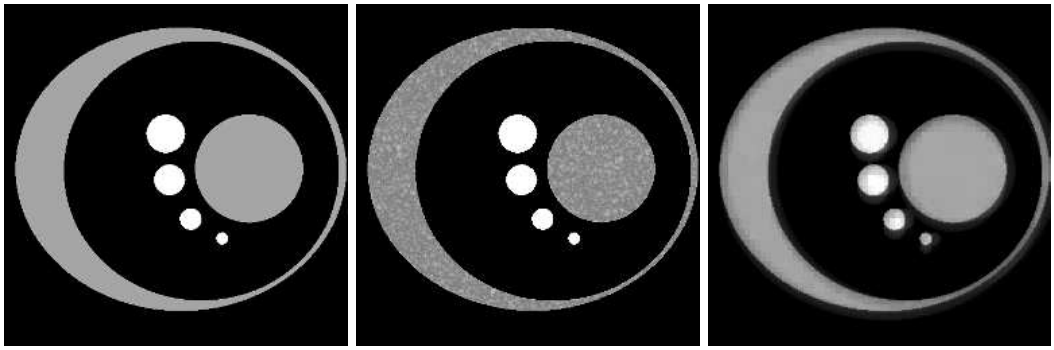

(a) (b) (c)

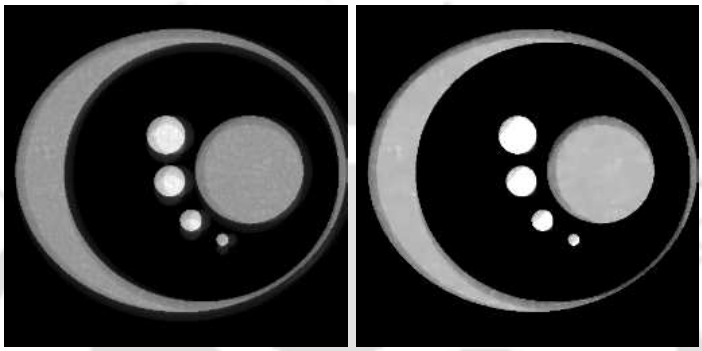

(d) (e)

Fig. 5.5: (a) Original image (b) speckled image at $\sigma_n = 0.3$ and denoised outputs of (c) the DWT-STH (d) the UDWT-STH and (e) the proposed method.

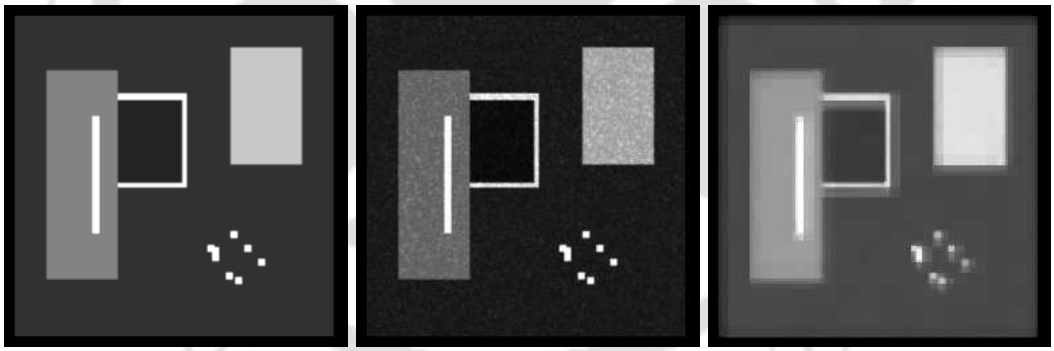

(a) (b) (c)

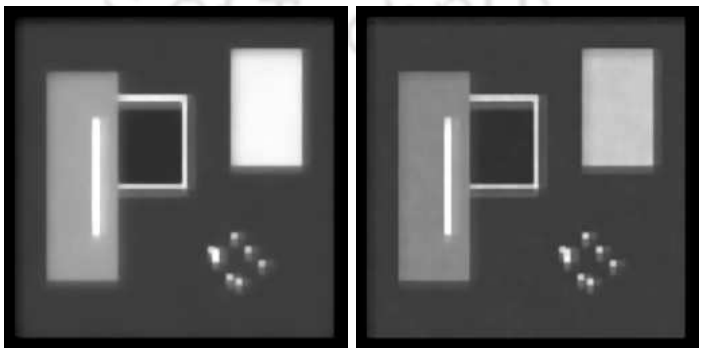

(d) (e)

Fig. 5.6: (a) Original image (b) speckled image at $\sigma_n = 0.3$ and denoised outputs of (c) the DWT-STH (d) the UDWT-STH and (e) the proposed method.

(a) (b) (c)

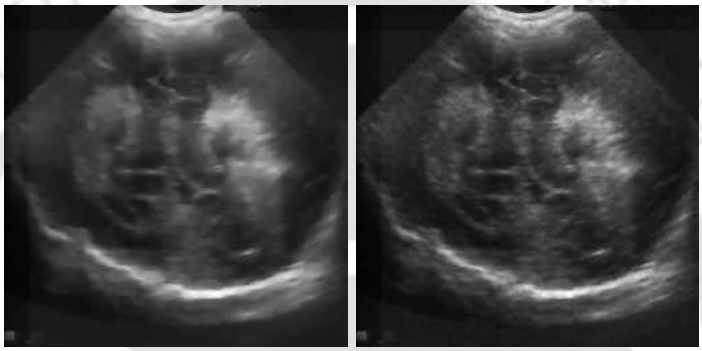

(d) (e)

Fig. 5.7: (a) Original image (b) speckled image at $\sigma_n = 0.3$ and denoised outputs of (c) the DWT-STH (d) the UDWT-STH and (e) the proposed method.

Table. 5.2: Performance of the proposed method and the soft thresholding based methods for different σ_n for the image in Fig. 5.4a

σ_n	DWT-STH		UDWT-STH		Proposed Method	
	S/MSE	β	S/MSE	β	S/MSE	β
0.2	14.3619	0.6377	14.4366	0.6662	14.7500	0.6941
0.3	13.8056	0.5979	13.9376	0.6541	14.0531	0.6564
0.4	13.4470	0.4629	13.5448	0.6182	13.6387	0.6148
0.5	13.3301	0.4345	13.4457	0.6004	13.5967	0.5980
0.6	12.8618	0.4364	12.8861	0.5360	13.3005	0.5530
0.7	12.4306	0.4071	12.4079	0.5220	13.2642	0.5356
0.8	12.7193	0.3928	12.7208	0.5016	13.2109	0.5100

C. *In vivo* Experiments

Since there is no speckle-free reference ultrasound images, it is difficult to measure the quantitative performance of the despeckling algorithms on real ultrasound images. The proposed method is applied on different real medical ultrasound images which already possess different levels of speckle. The value of ρ defined in Equation (4.41) is chosen in the range 0.2-0.5 by trial and error. Fig. 5.8a shows the original ultrasound image. The despeckled images using the DWT and UDWT based soft thresholding methods and the proposed method are shown in Figs. 5.8b-5.8d. Results of despeckling are also shown for another ultrasound image in Fig. 5.9. The visual inspection of the denoised outputs shows the superiority of the proposed despeckling method for the removal of speckle noise and preserving the detail features in the image.

We consider the SSNR and the ultrasound resolution index δ for measuring the performances of the proposed method compared to the soft thresholding based methods. The results for various real ultrasound images are presented in Table 5.3. Higher values of the SSNR and δ indicate that the proposed method outperforms the DWT-STH and the UDWT-STH methods quantitatively .

Table. 5.3: *In vivo* performance comparisons of the proposed method with other preprocessing based methods for different ultrasound images

Input image	Method	SSNR		δ	
		input	output	input	output
Kidney	DWT-STH	2.3644	2.7146	0.0763	0.1083
	UDWT-STH	2.3644	2.7153	0.0763	0.1083
	Proposed Method	2.3644	2.7192	0.0763	0.1087
Spleen	DWT-STH	1.2453	1.3789	0.0173	0.0268
	UDWT-STH	1.2453	1.3895	0.0173	0.0285
	Proposed Method	1.2453	1.3945	0.0173	0.0294
Breast	DWT-STH	2.1289	2.5985	0.0330	0.0581
	UDWT-STH	2.1289	2.6122	0.0330	0.0589
	Proposed Method	2.1289	2.6553	0.0330	0.0603
Liver	DWT-STH	2.3077	2.5545	0.0300	0.0390
	UDWT-STH	2.3077	2.5629	0.0300	0.0393
	Proposed Method	2.3077	2.5858	0.0300	0.0399
Gallbladder	DWT-STH	1.5640	1.7308	0.0149	0.0266
	UDWT-STH	1.5640	1.7569	0.0149	0.0286
	Proposed Method	1.5640	1.7695	0.0149	0.0295

5.5 Conclusion

In this chapter, we proposed sparse representations via overcomplete learned dictionary for the despeckling of medical ultrasound images. The method works in two stages. In the first stage, preprocessing of the ultrasound images is carried out using the whitening and Gaussianization procedures to convert the log-transformed speckle noise into white and Gaussian. In the second stage, a denoising method based on sparse representation on overcomplete dictionary is applied on the log-transformed speckle corrupted medical ultrasound images. It is experimentally demonstrated that the preprocessing of the ultrasound image is a necessary prerequisite for the despeckling methods using sparse and overcomplete representations. The simulation results on despeckling show that the proposed method outperforms the soft thresholding based sparse denoising methods, namely, the DWT-STH and the UDWT-STH both visually and quantitatively.

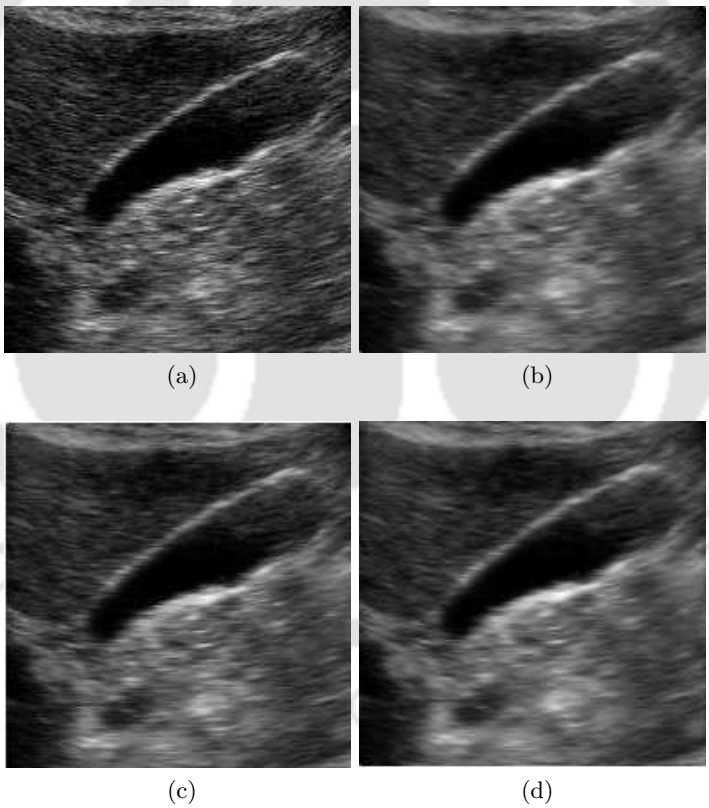

(a) (b)

(c) (d)

Fig. 5.8: (a) Ultrasound image. Denoising results obtained by (b) the DWT-STH method, (c) the UDWT-STH, and (d) the proposed Method.

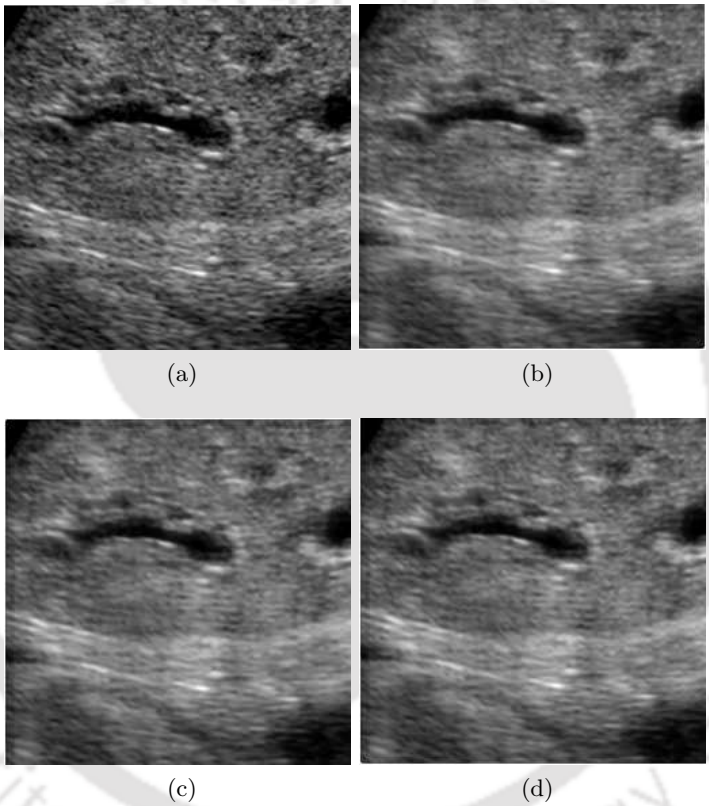

Fig. 5.9: (a) Ultrasound image. Denoising results obtained by (b) the DWT-STH. (c) the UDWT-STH and (d) the proposed Method.

Chapter 6

Conclusions and Future Work

6.1 Summary

The thesis investigated the use of sparse representation techniques for the removal of non-Gaussian, non-white and non-additive noise, namely, the impulse noise and the speckle noise. The major objective of the thesis has been to apply the sparse representation techniques for removing these noises. It particularly addresses the following issues:

1. Examine the methods for solving the sparse representation problem and suggest possible improvements for denoising applications.
2. Apply the sparse representation technique for the removal of the impulse noise.
3. Adapt the sparse representation methods for the removal of the speckle noise.

The research work carried out in this thesis resulted in the following contributions:

i) A modified Bayesian Pursuit Algorithm (BPA) is developed and applied for filtering the additive white Gaussian noise in images.

ii) A unified detection-based sparse reconstruction filter is proposed for the removal of the impulse noise from gray scale images.

iii) Two redundant wavelet transform based methods are proposed for the removal of speckle noise from medical ultrasound images.

iv) A denoising method using the sparse representation over redundant dictionary is proposed for the removal of the speckle noise from medical ultrasound images.

Chapter 2 investigated a modification of the standard Bayesian Pursuit Algorithm (SBPA). The SBPA determines the active atoms in the dictionary by a hypothesis testing procedure. It is an

iterative procedure which is initialized with an ℓ^2-norm solution and initially assumes sufficient number of active atoms by trial and error. The ℓ^2-norm solution is not a sparse solution and the performance of the SBPA can be improved by a sparse initialization and estimating the initial value of p from the initial sparse solution. Simulation study shows the advantage of the proposed modification in terms of representation and reconstruction errors compared to the standard BPA and other greedy pursuit algorithms especially at low noise. This chapter also investigates the effectiveness of the modified BPA for denoising of gray scale images corrupted by AWGN at different noise levels by integrating the modified BPA and the sparse representation based K-SVD algorithm for image denoising. The denoising results on standard test images demonstrate that the proposed framework outperforms the K-SVD based denoising algorithm using the OMP for low noise levels.

Chapter 3 proposed a two-stage detection based sparse reconstruction filter for the removal of impulse noise from gray scale images. The reconstruction principle of the proposed algorithm is based on the theory of compressed sensing. It has been demonstrated experimentally that the performance of the proposed filtering scheme depends mainly on the number of noise-free data available for reconstruction. The reconstruction fails if the noise-free data are less than the minimum samples required by compressed sensing. The proposed methods with the SD-ROM detection and the one with the ACWM detection are found to be the best for the removal of the fixed-valued and the random-valued impulse noises respectively. We have also compared the performance of the proposed method with the state-of-the-art detection based filtering schemes like the PSM, the SD-ROM, the MACWM, and the CEF. The experimental results show that with an efficient impulse detection method, the proposed reconstruction outperforms the detection-based filtering methods both quantitatively and qualitatively.

Chapter 4 investigated an application of the sparsity based denoising for medical ultrasound images corrupted by the speckle noise. We first analyzed an existing UDWT based Bayesian MAP estimator using the GGAD distribution to model the positive high-pass coefficients of the log-transformed ultrasound images and incorporated an optimal method for estimation of the distribution parameters. It is observed that the UDWT based despeckling method using the optimal parameter estimation performs better compared to the UDWT based method using the method of moments. This chapter also investigated the existing preprocessing methods for the decorrelation and the Gaussianization of the speckle noise in the log-transform domain. The preprocessed images are then subjected to soft-thresholding based UDWT denoising. The experimental results demonstrate superior performance compared to the UDWT based Bayesian shrinkage methods and the DWT-STH method both

qualitatively and quantitatively.

Chapter 5 proposed a method using sparse representation via overcomplete learned dictionary for the despeckling of medical ultrasound images. The method works in two stages. In the first stage, preprocessing of the ultrasound images is carried out using the procedure discussed in Chapter 4 to make the log-transformed speckle noise approximately white and Gaussian. In the second stage, a denoising method based on sparse representation on a K-SVD based overcomplete dictionary is applied on the log-transformed images. It is experimentally demonstrated that the preprocessing of the ultrasound image is a necessary prerequisite for the despeckling methods using sparse and overcomplete representations. The simulation results on despeckling show that the proposed method outperforms the soft-thresholding based sparse denoising methods, namely, the DWT-STH and the UDWT-STH both visually and quantitatively.

6.2 Directions for Future Work

The research work carried out in this thesis can be extended in a number of ways. A few tracks for future research are outlined below:

- The BPA is based on the Bayesian decision theory and promises to be a better alternative to the OMP and its variations. The performance of the BPA is inferior at higher noise levels. This point needs further investigation.
- The detection-based impulse denoising methods can be studied under the compressive sensing framework. In order to improve the incoherence between the random sensing matrix and the overcomplete dictionary, possibility for learning the sensing matrix for a given overcomplete dictionary can be investigated. This may further improve the quality of sparse reconstruction. The present work on impulse noise removal may also be extended to handle colour images. A straightforward extension will be to apply the sparse denoising on each colour channel separately.
- The sparse representations via overcomplete dictionaries for the removal of speckle in medical ultrasound images can be extended to filter intensity images obtained by synthetic aperture radar imaging.
- The thesis has explored learning of a single-scale dictionary for an image patch-by-patch. Techniques for learning multiscale dictionaries may be investigated as a future research direction.

Appendix A

Supplementary Materials

A.1 Methods for the Removal of Impulse Noise

A.1.1 SD-ROM filter

The input signal is filtered depending on the decision of the impulse detector. If a sample is detected as noisy then it is replaced with an estimation of the true value, otherwise it is left unaltered. It consists of the following two stages [27]:

1. *Impulse noise detection:*

   - Consider a 3×3 window $\mathbf{W}$ centered at $y(i,j)$. Define an observation vector containing the pixels in the neighbourhood of $y(i,j)$ and obtained by a left-right, top-to-bottom scan of the window:

     $\mathbf{w} = [w_1, w_2, \ldots, w_8]$

   - Arrange the observation vector $\mathbf{w}$ by their ranks $\mathbf{\Delta}$ given by $\mathbf{\Delta} = [\Delta_1, \Delta_2, \ldots, \Delta_8]$ such that $\Delta_1 \leq \Delta_2 \leq \ldots \Delta_8$.

   - Define the rank-ordered mean (ROM) by

     $\mathcal{M} = (\Delta_4 + \Delta_5)/2.$

   - Obtain the rank-ordered differences $\boldsymbol{\tau}^d$,

     where

     $$\tau_i^d = \begin{cases} \Delta_i - y(i,j), & \text{if } y(i,j) \leqslant \mathcal{M} \\ y(i,j) - \Delta_{9-i}, & \text{otherwise,} \end{cases} \tag{A.1}$$

     for $i = 1, \ldots, 4$.

   - Consider $y(i,j)$ to be noisy if

     $\tau_i^d > T_i,$

where T_1, T_2, T_3, and T_4 are threshold values such that $T_i < T_{i+1}$, for $i = 1, \ldots, 4$.

2. *Estimation of the true value:*

$$y(i,j) = \begin{cases} \mathcal{M}, & \text{if } y(i,j) \text{ is noisy} \\ X(i,j), & \text{otherwise.} \end{cases} \tag{A.2}$$

A.1.2 ACWM Filter

ACWM filter was originally used for the removal of random-valued impulse noise [28]. The filter is summarized as follows:

Let x_{ij} be the gray level value of a true image $\mathbf{x}$ at a location (i,j) and y_{ij} be the corresponding value in the noisy image $\mathbf{y}$. Consider a window defined in terms of the image coordinates symmetrically surrounding the current pixel x_{ij}, be

$$\mathbf{W} = \{(s,t)| \ -h \leqslant s \leqslant h, -h \leqslant t \leqslant h\}.$$

Let

$$\mathbf{Z}_{ij}^{w} = \text{median}\left(\mathbf{y}_{ij}^{w}\right), \tag{A.3}$$

where

$$\mathbf{y}_{ij}^{w} = \{y_{i-s,j-t}, w \diamondsuit y_{ij} | (s,t) \in \mathbf{W}, \ (s,t) \neq (0,0)\}. \tag{A.4}$$

In Equation (A.4), $w = 2k+1$, where k is a non-negative integer denotes the center weight, and the operator $\diamondsuit$ represents the repetition operation. The window size is assumed to be $2L+1 (L > 0)$. In [25], it is shown that Z_{ij}^{1} (i.e., $k = 0$) is the output of the standard median filter, whereas Z_{ij}^{2k+1} is the output of the identity filter (no filtering) when $k \geq L$. For the current pixel y_{ij}, consider the difference

$$d_k = \left| Z_{ij}^{w} - y_{ij} \right| = \left| Z_{ij}^{2k+1} - y_{ij} \right|, \tag{A.5}$$

where $k = 0, 1, \ldots, L-1$. It is shown that $d_k \leq d_{k-1}$ for $k \geq 1$ [28].

To determine whether the current pixel (i,j) is corrupted by the noise, a set of thresholds T_k are introduced, where $T_k > T_{k-1}$ for $k = 0, 1, 2, \ldots, L-1$. If any one of the inequalities $d_k > T_k (k = 0, 1, 2, \ldots, L-1)$ is true, then Y_{ij} is regarded as an impulse and replaced by the median i.e. Z_{ij}^{1}. Otherwise, the current pixel is considered as noise-free and kept unchanged.

The main difficulty in this method arises due to the selection of the thresholds. In [28], the authors proposed a threshold selection strategy as follows:

If a 3×3 window is considered (*i.e.*, $h = 1$ and $2L + 1 = 9$), four thresholds $T_k (k = 0, 1, 2, 3)$ are computed. The median of the absolute deviations from the median (MAD) are computed as:

$$\text{MAD} = \left\{ |y_{i-s,j-t} - Z_{ij}^1| \, (s,t) \in \mathbf{W} \right\}. \tag{A.6}$$

It is a robust estimate of the dispersion and its scaled version is used as the thresholds. The thresholds are then described as [28]

$$T_k = \nu.\text{MAD} + \delta_k, \;\; 0 \leqslant k \leqslant 3, \tag{A.7}$$

with

$$[\delta_0, \delta_1, \delta_2, \delta_3] = [40, 25, 10, 5], \tag{A.8}$$

and $0 \leq \nu \leq 1$. The parameter ν can be tuned to vary the thresholds at different noise-ratios.

A.1.3 Contrast Enhancement Filter

This filter is based on the contrast enhancement within the filtering window for the removal of random-valued impulse noise. The removal of the random-valued impulse noise is more difficult than the fixed-valued impulse noise because of their small differences in gray values with the neighbouring pixels. To overcome this problem, the authors in [107] proposed a nonlinear function to enhance the difference between the noisy pixels and the noise-free pixels in a progressive manner. The algorithm can be summarized as follows:

1. **Repeat**

2. Consider a window W of size $(2L + 1) \times (2L + 1)$. Find the normalized absolute differences

$$d(s,t) = \frac{1}{255} \left| y(s,t) - y(i,j) \right|, \tag{A.9}$$

   where $y(s,t) \in W$ and $s = i - L, \ldots, i + L$ and $t = j - L, \ldots, j + L$.

3. Transform the normalized absolute differences $\{d(s,t)\}$ to obtain $d^{(t)}(s,t)$

$$d^{(t)}(s,t) = \exp\left\{\varsigma.d(s,t)\right\} - 1, \tag{A.10}$$

   where ς is a constant that varies with the iterations.

4. Sort the $d^{(t)}(s,t)$ in ascending order to obtain $\{d^{(t)}(1), d^{(t)}(2), \ldots, d^{(t)}(9)\}$.

5. Consider the center pixel $y(i,j)$ noisy for a window of size 3×3 if

$$\sum_{i=1}^{5} d^{(t)}(i) \geqslant 25. \tag{A.11}$$

6. Replace the noisy pixel $y(i,j)$:

   - Let B be the set of pixels in the direction of minimum standard deviation. Then compute

$$m(i,j) = median\{w \diamondsuit x(s,t)\}, \tag{A.12}$$

   where

$$w = \begin{cases} 2, & \text{if } x(s,t) \in B \\ 1, & \text{otherwise} \end{cases}, \tag{A.13}$$

   and $\diamondsuit$ denotes repetition operation.

   - Compute

$$y(i,j) = \xi_{ij} x(i,j) + (1 - \xi_{ij}) m(i,j), \tag{A.14}$$

   where

$$\xi_{ij} = \begin{cases} 0, & \text{if } y(i,j) \text{ is noisy} \\ 1, & \text{otherwise} \end{cases} \tag{A.15}$$

7. **Until convergence** for different values of ς.

Bibliography

[1] A. Bovik, Ed., *Handbook of Image and Video Processing.* Academic Press, 2000.

[2] J. Astola and P. Kousmanen, *Fundamentals of Nonlinear Digital Filtering.* CRC Press, 1997.

[3] J. W. Goodman, "Some fundamental properties of speckle," *J. Opt. Soc. Am.*, vol. 66, no. 11, pp. 1145–1150, 1976.

[4] O. Michailovich and D. Adam, "Robust estimation of ultrasound pulses using outlier-resistant de-noising," *IEEE Transactions on Medical Imaging*, vol. 22, no. 3, pp. 368–381, March 2003.

[5] R. Wagner, S. Smith, J. Sandrik, and H. Lopez, "Statistics of speckle in ultrasound B-scans," *IEEE Transactions on Sonics and Ultrasonics*, vol. 30, no. 3, pp. 156–163, May 1983.

[6] Y. Erez, Y. Schechner, and D. Adam, "Ultrasound image denoising by spatially varying frequency compounding," in *Proceedings of DAGM Symposium*, pp. 1–10, 2006.

[7] A. Jain, *Fundamentals of Digital Image Processing.* Prentice Hall, 1989.

[8] A. Grossmann and J. Morlet, "Decomposition of Hardy functions into square integrable wavelets of constant shape," *SIAM Journal of Mathematical Analysis*, vol. 15, pp. 723–736, 1984.

[9] S. Mallat, "A theory for multiresolution signal decomposition: the wavelet representation," *IEEE Transactions on Pattern Analysis and Machine Intelligence*, vol. 11, no. 7, pp. 674 –693, July 1989.

[10] D. Donoho and I. M. Johnstone, "Adapting to unknown smoothness via wavelet shrinkage," *Journal of the American Statistical Association*, vol. 90, pp. 1200–1224, 1995.

[11] D. Donoho, "De-noising by soft-thresholding," *IEEE Transactions on Information Theory*, vol. 41, no. 3, pp. 613–627, May 1995.

[12] D. L. Donoho and I. M. Johnstone, "Ideal spatial adaptation by wavelet shrinkage," *Biometrika*, vol. 81, pp. 425–455, 1994.

[13] S. Chang, B. Yu, and M. Vetterli, "Adaptive wavelet thresholding for image denoising and compression," *IEEE Transactions on Image Processing*, vol. 9, no. 9, pp. 1532–1546, September 2000.

[14] M. Lang, H. Guo, J. E. Odegard, and C. S. Burrus, "Nonlinear processing of a shift invariant dwt for noise reduction," in *Proceedings of SPIE, Mathematical Imaging: Wavelet Applications for Dual Use, April 1995.*

[15] A. Gyaourova, C. Kamath, and I. K. Fodor, "Undecimated wavelet transforms for image de-noising," Center for Applied Scientific Computing, Lawrence Livermore National Laboratory, Tech. Rep., 2002.

[16] E. J. Candès and D. L. Donoho, "Curvelets - a surprisingly effective nonadaptive representation for objects with edges," in *Curves and Surfaces,* L. L. Schumaker et al. (Eds). Nashville, TN: Vanderbilt University Press, 1999.

[17] E. J. Candès, "Ridgelets and their derivatives: Representation of images with edges," in *Curves and Surfaces,* L. L. Schumaker et al. (eds). Nashville, TN: Vanderbilt University Press.

[18] M. N. Do and M. Vetterli, "Framing pyramids," *IEEE Transactions on Signal Processing*, vol. 51, pp. 2329–2342, 2003.

[19] J.-L. Starck, E. J. Candès, and D. L. Donoho, "The curvelet transform for image denoising," *IEEE Transactions on Image Processing*, vol. 11, pp. 670–684, 2002.

[20] R. Eslami and H. Radha, "Translation-invariant contourlet transform and its application to image denoising," *IEEE Transactions on Image Processing*, vol. 15, pp. 3362–3374, 2006.

[21] X. Zhanga and X. Jing, "Image denoising in contourlet domain based on a normal inverse gaussian prior," *Digital Signal Processing*, vol. 20, pp. 1439–1446, 2010.

[22] J. W. Tukey, "Nonlinear (nonsuperimposable) methods for smoothing data," in *Conference Records of Electronics and Aerospace Systems Convention (EASCON),* p. 673, 1974.

[23] I. Pitas and A. Venetsanopoulos, "Nonlinear mean filters in image processing," *IEEE Transactions on Acoustics, Speech and Signal Processing,*, vol. 34, pp. 573–584, 1986.

[24] D. R. K. Brownrigg, "The weighted median filter," *Commun. ACM*, vol. 27, pp. 807–818, August 1984.

[25] S.-J. Ko and Y. Lee, "Center weighted median filters and their applications to image enhancement," *IEEE Transactions on Circuits and Systems*, vol. 38, no. 9, pp. 984–993, September 1991.

[26] R. C. Hardie and K. E. Barner, "Rank-conditioned rank selection filters for signal restoration," *IEEE Transactions on Image Processing*, vol. 2, pp. 192–206, 1994.

[27] E. Abreu and S. Mitra, "A signal-dependent rank ordered mean (SD-ROM) filter-a new approach for removal of impulses from highly corrupted images," in *ICASSP*, vol. 4, pp. 2371 –2374, 1995.

[28] T. Chen and H. R. Wu, "Adaptive impulse detection using center-weighted median filters," *IEEE Signal Processing Letters*, vol. 8, no. 1, pp. 1–3, January 2001.

[29] J. Bamber and C. Daft, "Adaptive filtering for reduction of speckle in ultrasonic pulse-echo images." *Ultrasonics*, vol. 24, pp. 41–44, 1986.

[30] V. Dutt and J. Greenleaf, "Adaptive speckle reduction filter for log-compressed B-scan images," *IEEE Transactions on Medical Imaging*, vol. 15, no. 6, pp. 802–813, December 1996.

[31] J. I. Koo and S. B. Park, "Speckle reduction with edge preservation in medical ultrasonic images using a homogeneous region growing mean filter," *Ultrasonic Imaging*, vol. 13, no. 3, pp. 211–237, 1991.

[32] M. Karaman, M. Kutay, and G. Bozdagi, "An adaptive speckle suppression filter for medical ultrasonic imaging," *IEEE Transactions on Medical Imaging*, vol. 14, no. 2, pp. 283 –292, June 1995.

[33] J.-S. Lee, "Speckle analysis and smoothing of synthetic aperture radar images," *Computer Graphics and Image Processing*, vol. 17, no. 1, pp. 24–32, 1981.

[34] D. T. Kuan, A. A. Sawchuk, T. C. Strand, and P. Chavel, "Adaptive restoration of images with speckle," *IEEE Transactions on Acoustics, Speech and Signal Processing*, vol. 35, pp. 373–383, 1987.

[35] T. Loupas, W. McDicken, and P. Allan, "An adaptive weighted median filter for speckle suppression in medical ultrasonic images," *IEEE Transactions on Circuits and Systems*, vol. 36, no. 1, pp. 129 –135, January 1989.

[36] Y. Yu and S. Acton, "Speckle reducing anisotropic diffusion," *IEEE Transactions on Image Processing*, vol. 11, no. 11, pp. 1260–1270, November 2002.

[37] X. Zong, A. Laine, and E. Geiser, "Speckle reduction and contrast enhancement of echocardiograms via multiscale nonlinear processing," *IEEE Transactions on Medical Imaging*, vol. 17, no. 4, pp. 532 –540, August 1998.

[38] X. Hao, S. Gao, and X. Gao, "A novel multiscale nonlinear thresholding method for ultrasonic speckle suppressing," *IEEE Trans. on Med. Imaging*, vol. 18, no. 9, pp. 787–794, September 1999.

[39] E. Simoncelli and E. Adelson, "Noise removal via bayesian wavelet coring," in *Proceedings of ICIP*, pp. 379–382, 1996.

[40] A. Achim, A. Bezerianos, and P. Tsakalides, "Novel bayesian multiscale method for speckle removal in medical ultrasound images," *IEEE Transactions on Medical Imaging*, vol. 20, no. 8, pp. 772–783, August 2001.

[41] C. L. Nikias and M. Shao, *Signal processing with alpha-stable distributions and applications*. New York, NY, USA: Wiley-Interscience, 1995.

[42] S. Gupta, L. Kaur, R. C. Chauhan, and S. C. Saxena, "A versatile technique for visual enhancement of medical ultrasound images," *Digit. Signal Process.*, vol. 17, no. 3, pp. 542–560, 2007.

[43] R. F. Wagner, M. F. Insana, and S. W. Smith, "Fundamental correlation lengths of coherent speckle in medical ultrasonic images," *IEEE Transactions on Ultrasonics, Ferroelectrics, and Frequency Control*, vol. 35, pp. 34–44, 1988.

[44] O. Michailovich and A. Tannenbaum, "Despeckling of medical ultrasound images," *IEEE Transactions on Ultrasonics, Ferroelectrics and Frequency Control*, vol. 53, no. 1, pp. 64–78, January 2006.

[45] A. Pizurica, W. Philips, I. Lemahieu, and M. Acheroy, "A versatile wavelet domain noise filtration technique for medical imaging," *IEEE Transactions on Medical Imaging*, vol. 22, no. 3, pp. 323–331, March 2003.

[46] S. Foucher, G. Benie, and J.-M. Boucher, "Multiscale map filtering of SAR images," *IEEE Transactions on Image Processing*, vol. 10, no. 1, pp. 49–60, January 2001.

[47] H. Xie, L. E. Pierce, and F. T. Ulaby, "Despeckling sar images using a low-complexity wavelet denoising process," in *Proceedings of the IEEE International Geoscience and Remote Sensing Symposium*, 2002.

[48] A. Buades, B. Coll, and J. M. Morel, "On image denoising methods," Technical Note, CMLA (Centre de Mathematiques et de Leurs Applications), Tech. Rep., 2004.

[49] A. Buades, B. Coll, and J. Morel, "A review of image denoising algorithms, with a new one," *Multiscale Modelling and Simulation*, vol. 4, no. 2, pp. 490–530, 2005.

[50] M. Mahmoudi and G. Sapiro, "Fast image and video denoising via nonlocal means of similar neighborhoods," *IEEE Signal Processing Letters*, vol. 12, no. 12, pp. 839–842, 2005.

[51] P. Coupé, P. Hellier, C. Kervrann, and C. Barillot, "Nonlocal means-based speckle filtering for ultrasound images," *IEEE Transactions on Image Processing*, vol. 18, pp. 2221–2229, 2009.

[52] J. Manjón, J. Carbonell, J. Lull, G. García-Martí, L. Martí-Bonmatí, and M. Robles, "MRI denoising using Non-Local Means," *Medical Image Analysis*, vol. 12, pp. 514–523, 2008.

[53] D. J. Field, *Scale-invariance and self-similar "wavelet" transforms: an analysis of natural scenes and mammalian visual systems*, J. M., Hunt and C. Vascillicos, Eds. Oxford: Oxford University Press., 1993.

[54] B. Olshausen and D. Field, "Natural image statistics and efficient coding," in *Network: Computation in Neural Systems*, pp. 333–339, 1996.

[55] S. S. Chen, D. L. Donoho, and M. A. Saunders, "Atomic decomposition by basis pursuit," *SIAM Journal on Scientific Computing*, vol. 20, no. 1, pp. 33–61, 1998.

[56] M. Elad and M. Aharon, "Image denoising via sparse and redundant representations over learned dictionaries," *IEEE Transactions on Image Processing*, vol. 15, no. 12, pp. 3736–3745, December 2006.

[57] S. Mallat and Z. Zhang, "Matching pursuits with time-frequency dictionaries," *IEEE Transactions on Signal Processing*, vol. 41, no. 12, pp. 3397–3415, December 1993.

[58] Y. Pati, R. Rezaiifar, and P. Krishnaprasad, "Orthogonal matching pursuit: recursive function approximation with applications to wavelet decomposition," in *Proceedings of the 27th Annual Asilomer conference on Signals, Systems, and Computers,*, pp. 40–44, 1993.

[59] D. L. Donoho, "For most large underdetermined systems of equations, the minimal ℓ^1-norm solution is also the sparsest solution," *Communications on Pure and Applied Mathematics*, vol. 59, no. 7, pp. 797–829, 2004.

[60] R. R. Coifman and D. L. Donoho, "Translation-invariant de-noising," Department of Statistics, Stanford University, Tech. Rep., 1995.

[61] M. Lang, H. Guo, J. E. Odegard, C. S. Burrus, and R. O. W. Jr., "Noise reduction using an undecimated discrete wavelet transform," *IEEE Signal Processing Letters*, vol. 3, pp. 10–12, 1996.

[62] E. P. Simoncelli, W. T. Freeman, E. H. Adelson, and D. J. Heeger, "Shiftable multiscale transforms," *IEEE Transactions on Information Theory*, vol. 382, pp. 587–607, 1992.

[63] J.-L. Starck, E. Candes, and D. Donoho, "The curvelet transform for image denoising," *IEEE Transactions on Image Processing*, vol. 11, no. 6, pp. 670–684, June 2002.

[64] M. J. Fadili, J. L. Starck, and L. Boubchir, "Morphological diversity and sparse image denoising," in *Proceedings of ICASSP*, pp. 589–592, 2007.

[65] J. Starck, M. Elad, and D. Donoho, "Image decomposition via the combination of sparse representations and a variational approach," *IEEE Trans. on Image Processing*, vol. 14, pp. 1570–1582, 2005.

[66] D. L. Donoho and X. Huo, "Combined image representation using edgelets and wavelets," *Wavelet applications in signal and image processing VII, in SPIE*, vol. 3813, pp. 468–476, 1999.

[67] R. Rubinstein, A. M. Bruckstein, and M. Elad, "Dictionaries for sparse representation modeling," *Proceedings of the IEEE*, vol. 98, pp. 1045–1057, 2010.

[68] M. Aharon, M. Elad, and A. Bruckstein, " K-SVD: An algorithm for designing overcomplete dictionaries for sparse representation," *IEEE Transactions on Signal Processing*, vol. 54, no. 11, pp. 4311–4322, November 2006.

[69] B. A. Olshausen and D. J. Field, "Sparse coding with an overcomplete basis set: A strategy employed by V1?" *Vision Research*, vol. 37, no. 23, pp. 3311–3325, 1997.

[70] K. Engan, S. O. Aase, , and J. H. Hakon-Husoy, "Method of optimal directions for frame design," in *Proceedings of the IEEE Int. Conf. Acoustics, Speech, and Signal Processing*, pp. 2443–2446,1999.

[71] K. Kreutz-Delgado, J. F. Murray, B. D. Rao, K. Engan, T. Lee, and T. J. Sejnowski, "Dictionary learning algorithms for sparse representation," *Neur. Comput.*, vol. 15, pp. 349–396, 2003.

[72] M. S. Lewicki and T. J. Sejnowski, "Learning overcomplete representations," *Neur. Comput.*, vol. 12, pp. 337–365, 2000.

[73] J. Starck, M. Nguyen, and F. Murtagh, "Wavelets and curvelets for image deconvolution: A combined approach," *Signal Processing*, vol. 83, pp. 2279–2283, 2003.

[74] E. J. Candès, J. Romberg, and T. Tao, "Robust uncertainty principles: exact signal reconstruction from highly incomplete frequency information," *IEEE Transactions on Information Theory*, vol. 52, pp. 489–509, February 2006.

[75] L. Sendur and I. Selesnick, "Bivariate shrinkage with local variance estimation," *IEEE Signal Processing Letters*, vol. 9, pp. 438–441, 2002.

[76] J. Portilla, V. Strela, J. Wainwright, and E. P. Simoncelli, "Image denoising using scale mixtures of gaussians in the wavelet domain," *IEEE Transactions on Image Processing*, vol. 12, pp. 1338–1351, 2003.

[77] D. Donoho, M. Elad, and V. Temlyakov, "Stable recovery of sparse overcomplete representations in the presence of noise," *IEEE Transactions on Information Theory*, vol. 52, no. 1, pp. 6–18, Jan 2006.

[78] J. L. Starck, M. Elad, and D. L. Donoho, "Image decomposition: Separation of texture from piece-wise smooth content," in *SPIE Conf. Signal Image Process.: Wavelet Applicat. Signal Image Process., SPIE 48th Annu. Meeting*, San Diego, CA, August , 2003.

[79] J. Mairal, M. Elad, and G. Sapiro, "Sparse representation for color image restoration," *IEEE Transactions on Image Processing*, vol. 17, no. 1, pp. 53–69, January 2008.

[80] S. Roth and M. Black, "Fields of experts: A framework for learning image priors," in *Proceedings of the IEEE Conference on Computer Vision and Pattern Recognition*, pp. 860–867, June 2005.

[81] E. J. Candès and T. Tao, "Near-optimal signal recovery from random projections: universal encoding strategies," *IEEE Transactions on Information Theory*, vol. 52, pp. 5406–5425, December 2006.

[82] H. Huang and J. Zhu, "Removal of salt-and-pepper noise based on compressed sensing," *Electronics Letters*, vol. 46, pp. 1198–1199, August 2010.

[83] W. Dong, L. Zhang, G. Shi, and X. Wu, "Image deblurring and supper-resolution by adaptive sparse domain selection and adaptive regularization," *accepted for IEEE Transactions on Image Processing.*

[84] R. Gribonval and S. Lesage, "A survey of sparse component analysis for blind source separation: principles, perspectives, and new challenges," in *Proceedings of ESANN'06*, pp. 323–330, April 2006.

[85] D. L. Donoho, "Compressed sensing," *IEEE Transactions on Information Theory*, vol. 52, pp. 1289–1306, 2006.

[86] J. K. Pillai, V. M. Patel, R. Chellappa, and N. K. Ratha, "Secure and robust iris recognition using random projections and sparse representations," *IEEE Transactions on Pattern Analysis and Machine Intelligence (accepted for publication).*

[87] G. Davis, S. Mallat, and M. Avellaneda, "Adaptive greedy approximations," *Journal of Constructive Approximation*, vol. 13, pp. 57–98, 1997.

[88] I. Gorodnitsky and B. Rao, "Sparse signal reconstruction from limited data using FOCUSS: a re-weighted minimum norm algorithm," *IEEE Transactions on Signal Processing*, vol. 45, no. 3, pp. 600–616, March 1997.

[89] A. M. Bruckstein, D. L. Donoho, and M. Elad, "From sparse solutions of systems of equations to sparse modeling of signals," *SIAM Review*, vol. 51, no. 1, pp. 34–81, 2009.

[90] D. Wipf and B. Rao, "Sparse Bayesian learning for basis selection," *IEEE Transactions on Signal Processing*, vol. 52, no. 8, pp. 2153–2164, August 2004.

[91] S. Ji, Y. Xue, and L. Carin, "Bayesian compressive sensing," *IEEE Transactions on Signal Processing*, vol. 56, no. 6, pp. 2346–2356, June 2008.

[92] D. L. Donoho, Y. Tsaig, I. Drori, and J. luc Starck, "Sparse solution of underdetermined linear equations by stagewise orthogonal matching pursuit," Tech. Rep., 2006. [Online]. Available: http://www-stat.standford.edu/~idrori/STOMP.pdf

[93] T. Blumensath and M. Davies, "Gradient pursuits," *IEEE Transactions on Signal Processing*, vol. 56, no. 6, pp. 2370 –2382, June 2008.

[94] ——, "Stagewise weak gradient pursuits," *IEEE Transactions on Signal Processing*, vol. 57, no. 11, pp. 4333–4346, November 2009.

[95] H. Zayyani, M. Babaie-Zadeh, and C. Jutten, "Bayesian pursuit algorithm for sparse representation," in *Proceedings of the ICASSP 2009*, pp. 1549–1552, April 2009.

[96] M. Aharon, "Overcomplete dictionaries for sparse representation of signals," Ph.D. dissertation, The Technion - Israel Institute of Technology, November 2006.

[97] A. Papoulis, *Probability, Random Variables, and Stochastic Processes*. Mc-Graw Hill, 1984.

[98] H. Zayyani, M. Babaie-Zadeh, and C. Jutten, "Decoding real-field codes by an iterative expectation-maximization (EM) algorithm," in *Proceedings of ICASSP*, pp. 3169 –3172, 2008.

[99] J. Mairal, F. Bach, J. Ponce, G. Sapiro, and A. Zisserman, "Non-local sparse models for image restoration," in *Proceedings of the IEEE 12th International Conference on Computer Vision*, pp. 2272–2279, September 2009.

[100] G. H. Golub and C. F. Van Loan, *Matrix computations (3rd ed.)*. Baltimore, MD, USA: Johns Hopkins University Press, 1996.

[101] Z. Wang, A. C. Bovik, H. R. Sheikh, and E. P. Simoncelli, "Image quality assessment: From error visibility to structural similarity," *IEEE Transactions on Image Processing*, vol. 13, pp. 600–612, 2004.

[102] R. C. Gonzalez and R. E. Woods, *Digital Image Processing (3rd Edition)*. Upper Saddle River, NJ, USA: Prentice-Hall, Inc., 2006.

[103] W. Pratt, *Digital Image Processing.* John Wiley & Sons Inc, 1978.

[104] O. Yli-Harja, J. Astola, and Y. Neuvo, "Analysis of the properties of median and weighted median filters using threshold logic and stack filter representation," *IEEE Trans. on Signal Processing*, vol. 39, pp. 395–410, 1991.

[105] Z. Wang and D. Zhang, "Progressive switching median filter for the removal of impulse noise from highly corrupted images," *IEEE Transactions on Circuits and Systems II: Analog and Digital Signal Processing*, vol. 46, no. 1, pp. 78–80, January 1999.

[106] Y. Dong and S. Xu, "A new directional weighted median filter for removal of random-valued impulse noise," *IEEE Signal Processing Letters*, vol. 14, no. 3, pp. 193–196, March 2007.

[107] U. Ghanekar, A. Singh, and R. Pandey, "A contrast enhancement-based filter for removal of random valued impulse noise," *IEEE Signal Processing Letters*, vol. 17, no. 1, pp. 47–50, January 2010.

[108] R. Chan, C. Hu, and M. Nikolova, "An iterative procedure for removing random-valued impulse noise," *IEEE Signal Processing Letters*, vol. 11, no. 12, pp. 921–924, December 2004.

[109] S. Beygi-Harchegani, M. Kafashan, and F. Marvasti, "Impulsive noise removal from images using sparse representation and optimization methods," in *Proceedings of 10th International Conference on Information Science, Signal Processing and their Applications (ISSPA 2010)*, 2010.

[110] P. E. Ng and K. K. Ma, "A switching median filter with boundary discriminative noise detection for extremely corrupted images," *IEEE Transactions on Image Processing*, vol. 15, no. 6, pp. 1506–1516, 2006.

[111] H. Rauhut, K. Schnass, and P. Vandergheynst, "Compressed sensing and redundant dictionaries," *IEEE Transactions on Information Theory*, vol. 54, pp. 2210–2219, 2008.

[112] M. Elad, "Optimized projections for compressed sensing," *IEEE Transactions on Signal Processing*, vol. 55, pp. 5695–5702, Dec. 2007.

[113] C. Burckhardt, "Speckle in ultrasound B-mode scans," *IEEE Transactions on Sonics and Ultrasonics*, vol. 25, no. 1, pp. 1–6, January 1978.

[114] V. S. Frost, J. A. Stiles, K. S. Shanmugan, and J. C. Holtzman, "A model for radar images and its application to adaptive digital filtering of multiplicative noise," *IEEE Transactions on Pattern Analysis and Machine Intelligence*, vol. 4, pp. 157–165, 1982.

[115] S. Solb and T. Eltoft, "Homomorphic wavelet-bsed despeckling of sar images," *IEEE Transactions on Geoscience and Remote Sensing*, vol. 42, pp. 711–721, 2004.

[116] S. Gupta, R. Chauhan, and S. Saxena, "Locally adaptive wavelet domain bayesian processor for denoising medical ultrasound images using speckle modelling based on rayleigh distribution," *IEE Proceedings on Vision, Image and Signal Processing*, vol. 152, no. 1, pp. 129–135, 28 2005.

[117] L. L. D. Iraca and L. Verrazzani, "Power spectrum equalization for ultrasonic image restoration," *IEEE Transactions on Ultrasonics, Ferroelectronics, and Frequency Control*, vol. 36, pp. 216–222, 1989.

[118] F. Argenti and L. Alparone, "Speckle removal from SAR images in the undecimated wavelet domain," *IEEE Transactions on Geoscience and Remote Sensing*, vol. 40, pp. 2363–2374, 2002.

[119] M. O. Ulfarsson, J. R. Sveinsson, and J. A. Benediktsson, "Speckle reduction of sar images in the curvelet domain," in *Proceedings of the IEEE International Geoscience and Remote Sensing Symposium*, 2002.

[120] M.-Y. Huang, Y.-M. Huang, and M.-S. Wang, "Speckle reduction of ultrasound image based on contourlet transform," in *International Computer Symposium*, Taipei, Taiwan, Dec. 2004.

[121] L. Parthiban and R. Subramanian, "Speckle noise removal using contourlets," in *Proceedings of the International Conference on Information and Automation*, 2006.

[122] J. R. Sveinsson and J. A. Benediktsson, "Combined wavelet and curvelet denoising of sar images using tv segmentation," in *Proceedings of the IEEE International Geoscience and Remote Sensing Symposium*, 2007.

[123] S. Foucher, "SAR image filtering via learned dictionaries and sparse representations," in *Proc. of IGARSS 2008*, July, pp. 229–232, 2008.

[124] F. Argenti and G. Torricelli, "Speckle suppression in ultrasonic images based on undecimated wavelets," *EURASIP J. Appl. Signal Process.*, vol. 2003, pp. 470–478, 2003.

[125] B. Raju and M. Srinivasan, "Statistics of envelope of high-frequency ultrasonic backscatter from human skin in vivo," *IEEE Transactions onUltrasonics Ferroelectrics and Frequency Control*, vol. 49, no. 7, pp. 871–882, July 2002.

[126] P. Mohana Shankar, "A general statistical model for ultrasonic backscattering from tissues," *IEEE Transactions on Ultrasonics, Ferroelectrics and Frequency Control*, vol. 47, no. 3, pp. 727 –736, May 2000.

[127] S. Mallat, *A Wavelet Tour of Signal Processing, Second Edition (Wavelet Analysis & Its Applications)*, 2nd ed. Academic Press, September 1999.

[128] J. E. Fowler, "The redundant discrete wavelet transform and additive noise," *IEEE Signal Processing Letters*, vol. 12, pp. 629–632, 2005.

[129] M. Vetterli and J. Kovacevic, *Wavelets and Subband Coding*. Englewood Cliffs, NJ: Prentice Hall, 1995.

[130] S. Solbø and T. Eltoft, "Homomorphic wavelet-based statistical despeckling of sar images," *Geoscience and Remote Sensing, IEEE Transactions on*, vol. 42, no. 4, pp. 711 – 721, April 2004.

[131] E. W. Stacy and G. A. Mihram, "Parameter estimation for a generalized gamma distribution," *Technometrics*, vol. 7, no. 3, pp. 349–358, 1965.

[132] M. Simard, G. DeGrandi, K. Thomson, and G. Benie, "Analysis of speckle noise contribution on wavelet decomposition of sar images," *IEEE Transactions on Geoscience and Remote Sensing*, vol. 36, no. 6, pp. 1953 –1962, November 1998.

[133] J. A. Nelder and R. Mead, "A simplex method for function minimization," *The Computer Journal*, vol. 7, pp. 308–313, 1965.

[134] O. V. Michailovich and D. Adam, "A novel approach to the 2-D blind deconvolution problem in medical ultrasound," *IEEE Transactions on Medical Imaging*, vol. 24, pp. 86–104, January 2005.

[135] S.Roth and M.J.Black, "Fields of experts: A framework for learning image priors," in *Proceedings of the IEEE Conference on Computer Vision and Pattern Recognition*, 2005, pp. 860–867, June 2005.

[136] D. Sen, M. N. S. Swamy, and M. O. Ahmad, "Unbiased homomorphic system and its application in reducing multiplicative noise," *IEE Proceedings on Vision, Image and Signal Processing*, vol. 153, pp. 521–537, 2006.

List of Publications

Manuscript Revised

1. B. Deka and P. K. Bora, "Wavelet Based Despeckling of Medical Ultrasound Images," Communicated to IETE Journal of Research, Manuscript No.: IETEJR-36-10 (Mar. 2011)

2. B. Deka and P. K. Bora," Impulse Noise Removal Using Sparse Representation," Communicated to IET Image Processing, Manuscript No.: IPR-2010-0343 (Nov. 2011).

Manuscript Under Review

1. B. Deka and P. K. Bora,"Removal of Correlated Speckle Using Sparse Representation," Communicated to Digital Signal Processing, Manuscript No.: DSP-10-251 (Aug. 2010).

Conference Publications

1. B. Deka and P. K. Bora, "Removal of Random Valued Impulse Noise Using Sparse Representation," in Proceedings of NCC 2011, January, 2011.

2. B. Deka and P. K. Bora, "Enhancing the Performance of the Bayesian Pursuit Algorithm," in Proceedings of NCC 2011, January, 2011.

3. B. Deka and P. K. Bora, "Impulse Noise Removal Using Overcomplete dictionary" in Proceedings of INDICON 2010, December, 2010.

4. B. Deka and P. K. Bora, " Despeckling of Medical Ultrasound Images Using Sparse Representation," in Proceedings of IEEE International Conference of Signal Processing and Communications (SPCOM 2010), Bangalore, July, 2010.

5. B. Deka and P. K. Bora, "A Versatile Statistical Model for Despeckling of Medical Ultrasound Images," in Proceedings of IEEE INDICON 2009, Gandhinagar, December 2009.

6. B. Deka, A. K. Talukdar, and P. K. Bora, "Wavelet Based Adaptive Bayesian Despeckling for Medical Ultrasound Images," in Proceedings of IEEE TENCON 2009, Singapore, 2009.